

Miniaturized RF technology for femtosecond electron microscopy

Citation for published version (APA):

Lassise, A. (2012). *Miniaturized RF technology for femtosecond electron microscopy*. [Phd Thesis 1 (Research TU/e / Graduation TU/e), Applied Physics and Science Education]. Technische Universiteit Eindhoven. <https://doi.org/10.6100/IR739203>

DOI:

[10.6100/IR739203](https://doi.org/10.6100/IR739203)

Document status and date:

Published: 01/01/2012

Document Version:

Publisher's PDF, also known as Version of Record (includes final page, issue and volume numbers)

Please check the document version of this publication:

- A submitted manuscript is the version of the article upon submission and before peer-review. There can be important differences between the submitted version and the official published version of record. People interested in the research are advised to contact the author for the final version of the publication, or visit the DOI to the publisher's website.
- The final author version and the galley proof are versions of the publication after peer review.
- The final published version features the final layout of the paper including the volume, issue and page numbers.

[Link to publication](#)

General rights

Copyright and moral rights for the publications made accessible in the public portal are retained by the authors and/or other copyright owners and it is a condition of accessing publications that users recognise and abide by the legal requirements associated with these rights.

- Users may download and print one copy of any publication from the public portal for the purpose of private study or research.
- You may not further distribute the material or use it for any profit-making activity or commercial gain
- You may freely distribute the URL identifying the publication in the public portal.

If the publication is distributed under the terms of Article 25fa of the Dutch Copyright Act, indicated by the "Taverne" license above, please follow below link for the End User Agreement:

www.tue.nl/taverne

Take down policy

If you believe that this document breaches copyright please contact us at:

openaccess@tue.nl

providing details and we will investigate your claim.

Miniaturized RF Technology for Femtosecond Electron Microscopy

PROEFSCHRIFT

ter verkrijging van de graad van doctor aan de Technische Universiteit Eindhoven, op gezag van de rector magnificus, prof.dr.ir. C.J. van Duijn, voor een commissie aangewezen door het College voor Promoties in het openbaar te verdedigen op woensdag 7 november 2012 om 16.00 uur.

door

Adam Christopher Lassise

geboren te Denver, Verenigde Staten van Amerika

Dit proefschrift is goedgekeurd door de promotor:

prof.dr.ir. O.J. Luiten

Copromotor:

dr.ir. P.H.A. Mutsaers

Printed by Universiteitsdrukkerij Technische Universiteit Eindhoven

Cover photo by Nicola Debernardi (www.dobermanprod.biz) of sunset over the mountains surrounding Tucson, AZ.

A catalogue record is available from the Eindhoven University of Technology Library.

ISBN:978-90-386-3272-8

NUR 926

The work described in this thesis has been carried out at the group Coherence and Quantum Technology (CQT) at the Eindhoven University of Technology (TUE), Department of Applied Physics.



This work is part of the research program of the “Stichting voor Fundamenteel Onderzoek der Materie” (FOM), which is part of the “Nederlandse Organisatie voor Wetenschappelijk Onderzoek” (NWO).

Contents

1	Introduction	- 5 -
1.1	Radio Frequency Cavities in Electron Microscopy.....	- 5 -
1.2	Time Resolved Electron Microscopy.....	- 7 -
1.3	Scope of this Thesis	- 10 -
	References.....	- 11 -
2	Resonant Cavity Theory	- 13 -
2.1	Vacuum Pillbox	- 13 -
2.1.1	TM ₀₁₀ and TM ₁₁₀ Fields	- 14 -
2.1.2	Power, Energy, and Quality factor	- 17 -
2.2	Dielectric filled TM ₁₁₀ Pillbox	- 19 -
2.3	Comparison of Vacuum and Dielectric filled Pillbox.....	- 21 -
2.4	Principle of RF Compression (TM ₀₁₀ cavity)	- 22 -
2.5	Principle of RF Chopping (TM ₁₁₀ cavity).....	- 24 -
2.6	Conclusion	- 26 -
	References.....	- 26 -
3	TM₁₁₀ Cavity Design and Characterization	- 27 -
3.1	Construction	- 27 -
3.1.1	Electron pathway	- 27 -
3.1.2	Side ports	- 28 -
3.1.3	Elliptical shape.....	- 30 -
3.2	CST Microwave Studio Simulations	- 31 -
3.3	RF Cavity Characterization.....	- 32 -
3.3.1	Power Absorption	- 33 -
3.3.2	Field Profiles.....	- 34 -
3.3.3	Tuning Screw	- 36 -
3.3.4	Temperature Dependence of Frequency	- 37 -
3.4	Conclusion	- 39 -
	References.....	- 40 -
4	Experimental Setup and Beam line	- 41 -
4.1	Implementation.....	- 42 -
4.1.1	30 keV SEM.....	- 43 -
4.1.2	TM ₁₁₀ Dielectric Cavity.....	- 43 -
4.1.3	Extensions	- 45 -
4.2	Testing	- 46 -
4.3	Conclusion	- 49 -
	References.....	- 49 -
5	Beam Dynamics	- 50 -
5.1	Analytical Model.....	- 51 -
5.1.1	Momentum and Position	- 51 -
5.1.2	Emittance	- 53 -
5.1.3	Energy Spread	- 55 -
5.2	GPT.....	- 57 -
5.2.1	Fields, Momentum, and Position	- 57 -
5.2.2	Collimated Case.....	- 62 -
5.2.3	Focused Case.....	- 65 -
		- 3 -

5.2.4	Phase Space	- 68 -
5.3	Emittance Measurements	- 70 -
5.4	Conclusions	- 76 -
	References	- 77 -
6	Applications and Valorization	- 78 -
6.1	Implementation into an Existing Electron Microscope	- 79 -
6.1.1	Simulated Tecnai Implementation Results	- 81 -
6.1.2	Solutions to Reduce Energy Spread	- 83 -
6.2	Synchronization with a Laser: New Ideas.....	- 84 -
6.2.1	Dual Frequency TM_{110} Cavity	- 85 -
6.3	Phase Control Between Two Cavities Running Simultaneously	- 88 -
6.4	Poor Man's FEELS.....	- 90 -
6.4.1	Three Cavity Poor Man's FEELS Implementation Scheme for TU/e.....	- 93 -
6.5	Spherical Aberration Correction	- 95 -
6.6	Conclusion.....	- 97 -
	References	- 98 -
7	Fundamental Photon-Electron Interaction	- 99 -
7.1	Free Electron in a Standing Light Wave	- 99 -
7.2	Fundamental Motivation	- 102 -
7.2.1	Classical Polarization Dependence.....	- 103 -
7.2.2	Electron Diffraction from a Standing Light Wave	- 105 -
7.3	Applications of the Pomo and KD effects.....	- 105 -
7.3.1	Coherent Beam Splitter	- 105 -
7.3.2	Bunch Length Measurements	- 107 -
7.4	Feasibility of Ponderomotive Bunch Length Measurements in the Beam Line ...	- 109 -
7.5	Conclusion.....	- 112 -
	References	- 113 -
	Summary	- 115 -
	Outlook	- 118 -
A	Appendices	- 120 -
A.1	Emittance: Collimated Case	- 120 -
A.2	Emittance: Focused Case	- 122 -
A.3	Energy Spread	- 124 -
A.4	Electromagnetic Fields of a fs Laser Pulse.....	- 125 -
A.5	Technical Drawings for the TM_{110} Dielectric Cavity.....	- 126 -
	Acknowledgements.....	- 129 -
	Curriculum Vitae	- 132 -

1 Introduction

This thesis describes the use of radio frequency (RF) cavities as time dependent charged particle phase space manipulators, with the primary motivation being sub-picosecond (ps) time resolved electron microscopy and as a secondary motivation to investigate dynamic aberration correction. Since RF techniques have been developed with a high degree of sophistication in high energy particle accelerators, it is the agenda of the Coherence and Quantum Technology (CQT) group at the Eindhoven University of Technology (TUE) to use this RF knowledge and move from accelerators into ultrafast electron microscopy and diffraction. The development of the fourth dimension, time, into electron microscopes has been demonstrated with resolution ranging from nanoseconds (ns) [1] down into the femtosecond (fs) time regime [2,3] and even reaching down to attoseconds [4], but only with the required use of cumbersome fs laser systems. Within the scope of this thesis, the design, development, and characterization of a working table-top setup without the mandatory use of lasers is described. This chapter describes the background of RF cavities in the scope of electron microscopy as well as the most recent time-resolved electron experiments.

1.1 Radio Frequency Cavities in Electron Microscopy

With the development of the electron microscope in 1931 by Ernst Ruska and Max Knoll, the resolution of microscopes was no longer limited to the wavelength of light, but instead the wavelength of electrons, in theory. It took a further two years of development to finally break the resolution obtained with an optical microscope [5]. But the limit to resolution of these new electron microscopes was far from the expected deBroglie wavelength of the electrons.

The largest hurdle to electron microscopy, both in the early years and now, is aberrations caused by the electron lenses, both spherical and chromatic. As Hawkes stated, “Electron lenses are extremely poor: if glass lenses were as bad, we should see as well with the naked eye as with a microscope!” In 1936, Otto Scherzer presented his namesake theorem: that a rotationally symmetric electro/magnetostatic lens will always have a positive-definite aberration coefficient [5].

In 1939, Nesslinger studied the use of an einzel lens excited not by a DC voltage, but by a high-frequency signal instead. He first chopped an incident beam into pulses with a deflection system, and then had them traverse the lens. He noted that the focal length of the lens varied with the phase of the bunches with respect to the AC excitation signal. This was the first time that the “phase condition” and “transit time” became important in understanding the use of time-dependent lenses. In this way, Nesslinger was the first to

attempt to navigate around Scherzer's theorem, by no longer using electro-magnetostatic lenses [6,7].

In 1941, Rudolph Kompfner proposed again the use of a chopped beam and a high-frequency excitation of a lens [8]. However, this was found to be outweighed by, "...technical difficulties arising from the complication of the scheme. [9]"

By 1947, after more than a decade of trying to find ways around his theorem, Scherzer presented a design for a high-frequency cavity to correct both spherical and chromatic aberration [10]. He commented that the period of the AC field should be on the same order of magnitude as the time spent by the electrons in the field, implying hundreds of megahertz (MHz) or even gigahertz (GHz), both being beyond the technology of the time [5]. According to Hawkes and Kasper, "...there is no reason to believe that his lens would not behave as predicted (subject to some improvement in the shape of the cavity for operation in the gigahertz range)," [7]. After considering many options to navigate around his theorem, Scherzer was confident that it would be either non-rotationally symmetric systems or high-frequency systems that would be the first to reach angstrom resolution.

In the 1970's, interest in the use of resonant cavities with pulsed beams as spherical aberration correctors began to rise, particularly at Cambridge. Vaidya suggested, in collaboration with Hawkes, Garg, and Pandey, a "synklysmotron" to correct the aberration of a magnetic lens. This scheme uses two cavities, the first as a buncher, and the second as a corrector [11]. Under the guidance of Hawkes, Oldfield carried out a thorough study of the fields inside re-entrant cavities and their paraxial properties, finding the "phase dependence" to be of the utmost importance [12].

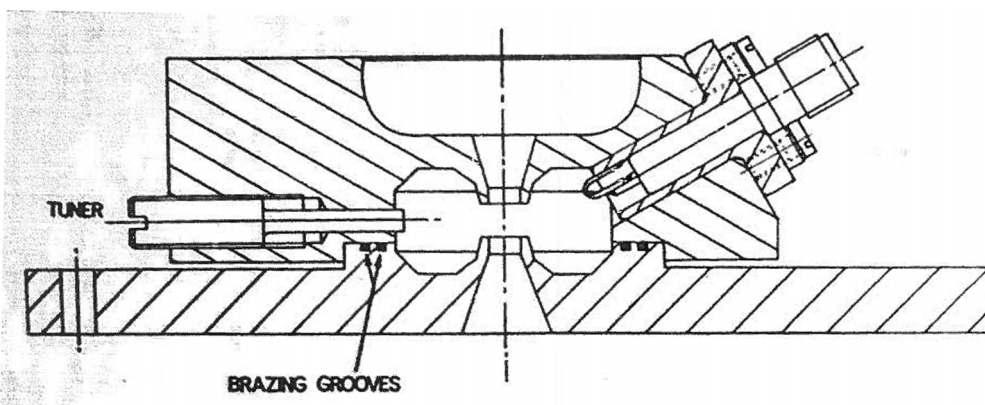


Figure 1.1: Drawing of Oldfield's cylindrically symmetric cavity, taken from Ref. [12].

Oldfield designed and commissioned a dual cavity system. He built a rotationally symmetric electron beam chopper (see Fig. 1.1) for picosecond pulses coupled with "...an 'energy correcting' cavity operating in synchronism with the chopper," [13]. Oldfield eventually concluded, "Preliminary results obtained with one-, two-, and three-cavity systems show that it is possible to obtain at gigahertz frequencies electron pulses which, in terms of energy spread and phase width, are adequate for electron optical and most other applications." However, he mentioned that, "Owing to astigmatic focusing of the second cavity as a result of field distortion introduced by the frequency tuner, the full potential of the design has yet to be realized," [12,13]

In 1974, Matsuda and Ura derived the formulae for most of the aberration coefficients of various cavities, and also presented a dual-cavity system to be implemented in a scanning electron microscope (SEM) [14,15]. His first cavity was a deflector with a chopping aperture, followed by a bunching cavity, similar to Oldfield. Ura reported compressing bunches down to 0.2 ps, the first time a regular train of fs electron pulses had been reported [16].

Recent exploration of time-dependent tricks to circumvent Scherzer's theorem has again been done, with the 2006 work of Schoenhense [3]. In his paper, he discusses the theoretical method of switching of electrical acceleration fields or lens fields to create a time dependent aberration coefficient which, at particular times, is negative. In the method, he exploits the highly precise time structure of pulsed photon sources or pulsed lasers in combination with pulsed photocathodes.

With present day RF techniques and ultrafast beam technology matured, coupled with the high speed computer processing capabilities (compared to the 60's and 70's) necessary for simulations and calculations, the time seems right to employ the earlier ideas of Scherzer, Ura, and Oldfield and improve upon them to advance the electron microscopy community.

1.2 Time Resolved Electron Microscopy

A time-resolved technique for electron microscopes has been desired since the first glimpse into the atomic world, with early interest beginning with electron stroboscopic microscopy in the late 1960's. While the majority of the work was in the context of aberration correction, as previously discussed, ns and ps resolution was desired for the imaging of the (then) newly developed semiconductor devices [16].

In 1968, Plows and Nixon demonstrated that a stroboscopic scanning electron microscope could study surface voltages, which are changing at very high frequencies. They pulsed the electron beam to 10 ns, at a 7 MHz repetition rate. The pulsing was achieved with deflector plates that pass over a chopping aperture. If the deflector plates are synchronized

to a cyclical voltage cycle on the sample, the image gives a temporal resolution of a particular phase of the voltage cycle. By varying the phase, different phases of the cycle are imaged [17].

In 1973, Gopinath and Hill sent an SEM beam between the outer and helical inner of a coaxial line. The coaxial line is used to streak the beam back and forth across an aperture, giving short pulses at a high repetition rate. They reported approximately 10 ps pulses at a 9.1 GHz repetition rate. With this, they imaged Gunn devices, also operating at 9.1 GHz, imaging various phases of the Gunn device's cycle [18]. The chopping was again performed by an "electrostatic" deflector. In a similar setup, Feuerbaum and Otto reported chopping bunches down to 350 ps [19]. By 1985, Sadorf and Kratz had also designed a new beam chopping system, capable of operating with electron energies of 0.75-3 keV, creating pulses of 15 ps, with repetition rates up to the microwave range [20].

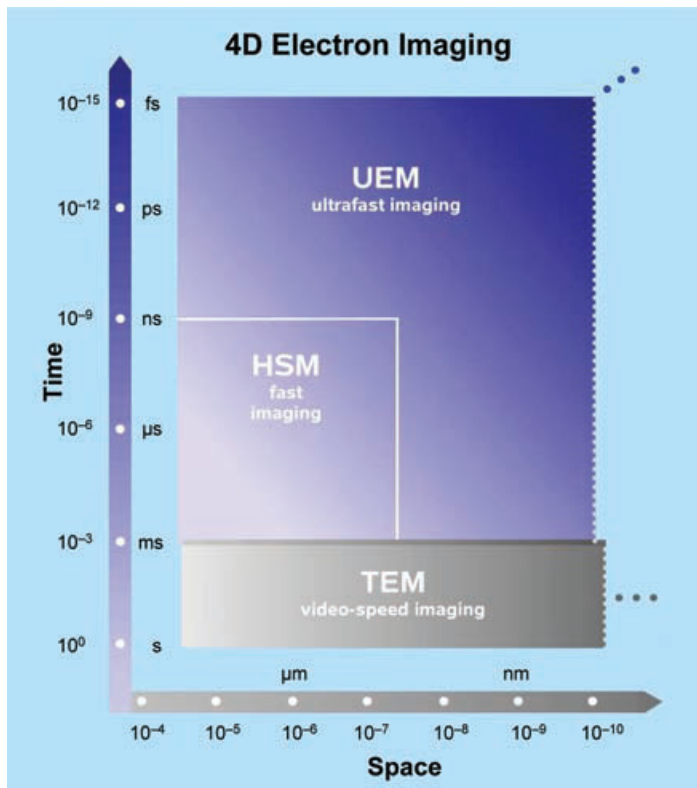


Figure 1.2: Pictorial representation of the temporal and spatial resolution of normal TEM imaging, High Speed Microscopy, and Ultrafast Microscopy. Image taken from Ref. [2].

Jumping forward 30 years, Gai and Boyes demonstrated in an environmental TEM atomic resolution of nanoparticles participating in catalytic reactions [21]. They were able to

illustrate both temperature dependence of the reaction, as well as temporal resolution of ms and longer, labeled TEM and seen in grey in Fig. 1.2. However, they were temporally limited in their resolution by the response of the detector and electronics.

The group of Ganiere in Lausanne has a photoemission-based electron gun based inside of an SEM capable of delivering 12 picosecond pulses at a repetition rate of 80.7 MHz focused onto a probe diameter of 50 nm at the sample with a probe current of only 10 pA. The setup, using cathodoluminescence, successfully characterized different nanostructures grown in InGaAs/AlGaAs and allowed for the description of carrier transport in the quantum structures [22].

Lagrange, in the group of Browning at the Lawrence Livermore National Laboratory in California, has built what the group calls a dynamic transmission electron microscope (DTEM). With this machine, a 10 ns laser pulse is focused upon a photocathode to create ~ 15 ns pulses. There are $\sim 10^7$ electrons present in each of the pulses. This allows for single shot studies, ideal for pump-probe measurements. With a spatial resolution of <10 nm and a temporal resolution of 15 ns, the DTEM was able to study reactions in multilayer films, transformations in nanocrystals, and the catalytic growth of nanowires [23].

Bostanjoglo built a photoelectron ns microscope in Berlin, capable of ever smaller time resolution, but at the cost of resolution, only able to resolve down to the micron and sub-micron levels [1], roughly the spatial resolution of a light microscope. However, Bostanjoglo was able to do it all with a single pulse. The spatial and temporal resolution of his machine is limited by the space-charge explosion of the bunch.

One way to navigate the space charge explosion is to reduce the charge. Zewail developed a photo-driven microscope, dubbed an ultrafast electron microscope (UEM), which gives ~ 1 electron, per bunch [2]. In this way, an image is built up of a reversible process, with the electrons synchronized to image the same "phase" of the process, similar to Plows and Nixon, and Gopinath and Hill [17,18]. This particular machine has demonstrated fantastic results, with spatial resolution down to a few angstroms and temporal resolution of a few hundred fs [2]. Carbone performed pump-probe femtosecond electron energy loss spectroscopy (FEELS) of graphite with this machine in 2008 [24]. Yurtsever used it again in 2012 to image and do FEELS spectroscopy of a silver nanoparticle on graphene and upon a copper-vacuum interface. The sample was pumped with a laser, and the resulting plasmon response was taken with spatial, temporal, and energy resolution of nm, fs, and meV, respectively [25].

Another way to navigate around this space charge explosion of a high electron density bunch created on a photocathode was demonstrated by van Oudheusden. By appropriately shaping the laser on the cathode, the bunch that comes out has linear space charge fields, causing the bunch to expand in all three directions. A solenoid is sufficient to collimate the beam transversely, and an RF cavity is used to compress the bunch back down to 100 fs. He demonstrated compression of 0.1 pC down to a temporal resolution of 100 fs, sufficient for single-shot time resolved diffraction images [26].

Kubo imaged the nonlinear two-photon photoemission from a sample, creating a movie with a rate of 330-attoseconds/frame, making photoemission electron microscopy (PEEM) the fastest form of time-resolved electron microscopy [4]. It was in the scope of time-resolved PEEM that Schoenhense has suggested aberration correction with pulsed sources, bringing us full circle back to Scherzer's theorem [3].

1.3 Scope of this Thesis

The designs, simulations, and experiments described in this thesis involve the use of a radio frequency (RF) cavity to create fs electron bunches for time-resolved electron microscopy. The goal is to create fs electron bunches at a high repetition rate without the use of lasers; this is achieved by chopping a DC electron beam rather than using photocathodes. To generate the electron bunches at a high repetition rate, the DC electron beam is sent through an RF cavity with a transverse magnetic field that sweeps the DC beam back and forth across a slit twice per RF period. Assuming a large enough sweep and small enough slit, the DC beam is chopped into fs electron bunches at a high repetition rate. To achieve ~ 1 electron per bunch and a bunch length of 100 fs, an initial DC current of $\sim 1 \mu\text{A}$ must be supplied.

Chapter 2 describes the theory of two types of RF cavities: TM_{010} and TM_{110} . The TM_{010} cavity was designed in a parallel project [26] to manipulate the longitudinal properties (compression/expansion) of electron bunches using an electric field. The TM_{110} cavity is a dielectric loaded sweep cavity, previously mentioned to chop the DC beam. It is filled with a dielectric to reduce both the size and power consumption. Chapter 3 discusses the technical design, construction, and testing of the TM_{110} dielectric cavity. Chapter 4 gives an overview of the experimental setup built in this project, discussing the capabilities and limitations of the 30 keV altered scanning electron microscope (SEM) beam line. In Ch. 5, an analytical model to predict the longitudinal and transverse beam quality after traversing the sweep cavity is presented. Following, it is compared to numerical simulations, and finally compared to experiments.

Chapter 6 describes future work which could be carried out in the scope of this project, beginning with a simulated study of implementation of the TM_{110} cavity into a commercial microscope done in coordination with FEI Company [27]. Later, a new hybrid cavity is suggested for synchronization with lasers, followed by experimental verification of phase control between a TM_{110} cavity and a TM_{010} cavity. Unifying the previous sections of the chapter is a simulated suggestion for a table top pump-probe setup for femtosecond electron energy loss spectroscopy (FEELS) with < 1 eV energy resolution, dubbed the "Poor man's FEELS." Finally, to conclude Ch. 6, a setup to test the ability of the TM_{010} cavity to act as a spherical aberration correction device is described and simulated. And last but not least, with ultrashort electron bunches generated and synchronization with a laser accurately achieved, the manipulation of electrons with the electromagnetic fields of a laser pulse is investigated. Chapter 7 discusses the ponderomotive effect of a charged particle in a standing light wave. The fundamental motivation for shooting electrons with lasers is presented, with possible applications discussed, and finishing with a feasibility study for implementation into the beam line for temporal bunch length measurements.

Throughout the project, simulations were relied upon heavily for the design, testing, and analysis of the experimental setup, as will be presented in Ch. 3, 5, 6, and 7. All numerical simulations, unless otherwise stated, were carried out with the well-established General Particle Tracer (GPT) code [28]. The code is a C-based simulation platform for the study of charged particle dynamics in electromagnetic fields in 3D including coulomb effects, space charge, and fringe fields; providing a solid basis for all 3D and non-linear effects. It utilizes an embedded fifth-order Runge-Kutta driver with adaptive step sizes to ensure an accuracy of up to 10^{-10} with respect to the smallest given time step [28]. This ensures complete confidence in the overall accuracy of the results given by GPT, allowing comparison with theoretical models as well as experimental measurements.

References

- [1] O. Bostanjoglo, R. Elschner, Z. Mao, T. Nink, M. Weingaertner. "Nanosecond electron microscopes." *Ultramicroscopy* 81 (2000): 141-147.
- [2] Zewail, Ahmed H. "Four-Dimensional Electron Microscopy." *Science* 328 (2010): 187-193.
- [3] G. Schoenhense and H.J. Elmers. "PEEM with high time resolution- imaging of transient processes and novel concepts of chromatic and spherical aberration correction." *Surf. and Interface Anal.* 38 (2006): 1578-1587.
- [4] A. Kubo, K. Onda, H. Petek, Z. Sun, Y.S. Jung, and H.K. Kim. "Femtosecond Imaging of Surface Plasmon Dynamics in a Nanostructured Silver Film." *Nano Letters* 5 (2005): 1123-1127.
- [5] Hawkes, P.W. "Aberration correction past and present." *Phil. Trans. R. Soc. A* 367 (2009): 3637-3664.
- [6] Nesslinger, A. "Ueber Achromasie von Elektronenlinsen." *Jahrb. AEG-Forschung* 6 (1939): 83-85.
- [7] P.W. Hawkes, and E. Kasper. *Principles of Electron Optics*. New York: Academic Press, 1989.

- [8] Kompfner, R. "On a method of correcting the spherical error of electron lenses, especially those employed with electron microscopes." *Phil. Mag.* 32 (1941): 410-416.
- [9] Gabor, D. *The electron microscope, its development, present performance and future possibilities*. London: Hulton Press, 1945.
- [10] Scherzer, O. "Sphaerische und chromatische Korrektur von Elektronen-Linsen." *Optik* 2 (1947): 114-132.
- [11] Vaidya, N.C. "Synklysmotron lenses- a new electron-optical correcting system." *Proc. IEEE* 60 (1972): 245-247.
- [12] Oldfield, L. *Microwave cavities as electron lenses*. Cambridge: University of Cambridge, 1973. Thesis.
- [13] Oldfield, L. "A rotationally symmetric electron beam chopper for picosecond pulses." *J. Phys. E: Sci. Instrum.* 9 (1976): 455-463.
- [14] J.-i. Matsuda, K. Ura. "The aberration theory of the electron trajectory in the RF fields. Part 1. The second-order aberration." *Optik* 40 (1974): 179-192.
- [15] K. Ura, H. Fujioka, T. Hosokawa. "Picosecond Pulse Stroboscopic Scanning Electron Microscope." *J. Electron Microsc.* 27 (1978): 247-252.
- [16] T. Hosokawa, H. Fujioka, and K. Ura. "Generation and measurement of subpicosecond electron beam pulses." *Rev. Sci. Instrum.* 49 (1978): 624-628.
- [17] G.S. Plows, W.C. Nixon. "Stroboscopic scanning electron microscopy." *J. Phys. E: Sci. Instrum.* 1 (1968): 595-600.
- [18] A. Gopinath, M.S. Hill. "Deflection beam-chopping in the SEM." *J. Phys. E: Sci. Instrum.* 10 (1977): 229.
- [19] H.P. Feuerbaum, J. Otto. "Beam chopper for subnanosecond pulses in scanning electron microscopy." *J. Phys. E: Sci. Instrum.* 11 (1978): 529.
- [20] H. Sadorf, H.A. Kratz. "Plug-in fast electron beam chopping system." *Rev. Sci. Instrum.* 56 (1985): 567-571.
- [21] P.L. Gai, E.D. Boyes. "Advances in Atomic Resolution In Situ Environmental Transmission Electron Microscopy and 1 Å Aberration Corrected In Situ Electron Microscopy." *Microscopy Research and Techniques* 72 (2009): 153-164.
- [22] M. Merano, S. Sonderegger, A. Crottini, S. Collin, E. Pelucchi, P. Renucci, A. Malko, M.H. Baier, E. Kapon, J.D. Ganiere, B. Deveaud. "Time-Resolved cathodoluminescence of InGaAs/AlGaAs tetrahedral pyramidal quantum structures." *Applied Physics B* 84 (2006): 343-350.
- [23] T. LaGrange, G.H. Campbell, B.W. Reed, M. Taheri, J.B. Pesavento, J.S. Kim, N.D. Browning. "Nanosecond time-resolved investigations using the in situ of dynamic transmission electron microscope (DTEM)." *Ultramicroscopy* 108 (2008): 1441-1449.
- [24] F. Carbone, B. Barwick, O.H. Kwon, H.S. Park, J.S. Baskin, A.H. Zewail. "EELS femtosecond resolved in 4D ultrafast electron microscopy." *Chemical Physics Letters* 468 (2009): 107-111.
- [25] A. Yurtsever, R.M. van der Veen, A.H. Zewail. "Subparticle Ultrafast Spectrum Imaging in 4D Electron Microscopy." *Science* 335 (2012): 59-64.
- [26] van Oudheusden, Thijs. *Electron Source For Sub-Relativistic Single-Shot Femtosecond Diffraction*. Eindhoven: TU Eindhoven, 2010. Thesis
- [27] FEI Company. "FEI Internal Document." n.d. *FEI Company*. www.fei.com.
- [28] Pulsar Physics. "General Particle Tracer (GPT) User Manual." n.d. *General Particle Tracer (GPT)*. www.pulsar.nl.

2 Resonant Cavity Theory

As discussed in Sec. 1.1, utilizing RF cavities in electron microscopes is not a new idea, despite having a different purpose. Our group, CQT, here at TU/e utilizes two types of RF cavities as time-dependent lenses, the TM_{010} and TM_{110} cavities. In order to describe and understand the way these two cavities operate, first the electromagnetic field equations and patterns for a cylindrically symmetric pillbox geometry will be described. From the field equations, analytical solutions for the power lost to the cavity and the energy in the fields will be given. As a way to reduce the size and power consumption of one of the two cavities, the cavity is filled with a dielectric material. The changes in power consumption and size of the dielectric filled cavity will be discussed, presenting the specific high permittivity, low loss tangent dielectric material that was chosen for this project.

Once the field patterns are described, the general purpose of operation of each of the cavities can be discussed. The TM_{010} cavity is used as a longitudinal phase space manipulator. Its primary purpose is to compress or expand (longitudinally focus or defocus, respectively) a temporally short bunch of electrons. The TM_{110} cavity, on the other hand, is used as a streak cavity. The streak cavity is designed to streak a DC electron beam back and forth across an aperture, creating ultrashort electron bunches at a high repetition rate. In this way, it will be clear that the two RF cavities act as time-dependent correlated phase space manipulators.

2.1 Vacuum Pillbox

We start from a standard rectangular cylindrical volume of vacuum surrounded by perfectly conducting metallic walls with radius a in the xy -plane, and length d in the z direction, as seen in Fig. 2.1. By solving Maxwell's equations, cylindrical cavities always have either the E_z or B_z component of the field equal to zero. If the electric field is zero, it is known as a transverse electric (TE) mode; when the magnetic field has no z -component, it is known as the transverse magnetic (TM) mode; when both are zero, it is known as a transverse electro-magnetic (TEM) mode. The modes are characterized by three integers; l , m , n . These integers are used to describe the eigenvalues of the wave vector k needed to satisfy the boundary conditions, and are dependent upon the mode, frequency, and cavity dimensions. The modes are then written as $TM_{l,m,n}$, and analogously for TE; however for TEM modes, $n=0$ and is left out [1]. The scope of this thesis is narrowed to the treatment of cavities operating in the monopole and dipole transverse magnetic modes, TM_{010} and TM_{110} , respectively.

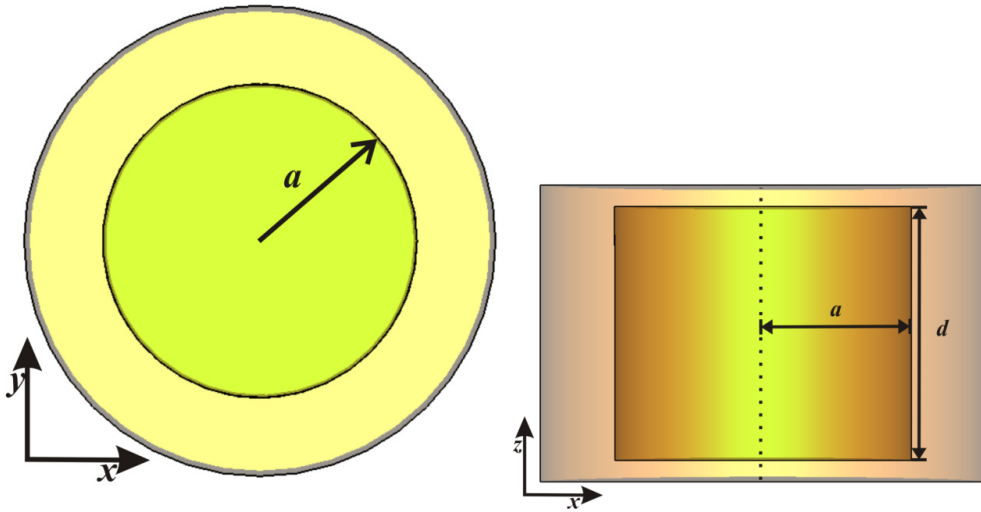


Figure 2.1: An ideal cylindrical pillbox cavity with radius a and length d .

2.1.1 TM_{010} and TM_{110} Fields

The lowest TM mode, TM_{010} or monopole mode, is characterized by a longitudinal electric field which is maximal at $r=0$, and an azimuthal magnetic field which is zero at $r=0$ [2]. A schematic cross-sectional representation can be seen in Fig. 2.2.

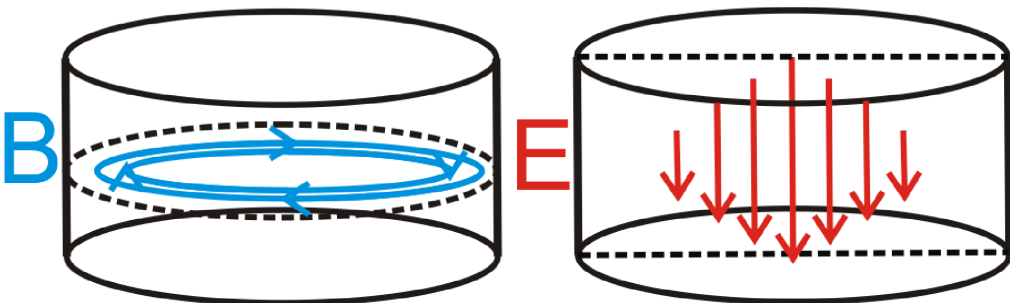


Figure 2.2: Cross-sectional view demonstrating the magnetic and electric fields in the TM_{010} pillbox cavity.

The next mode higher in frequency is the TM_{110} , or dipole mode. It has a longitudinal electric field, which is zero at $r=0$, and a transverse magnetic field that is strongly present at $r=0$, as seen in Fig. 2.3.

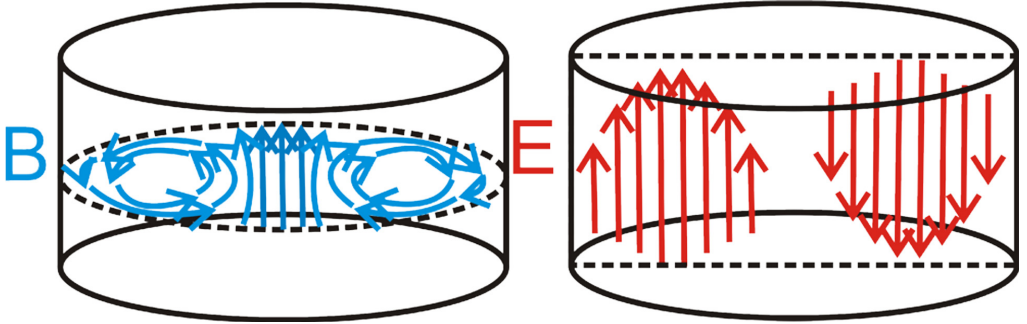


Figure 2.3: Cross-sectional view demonstrating the magnetic and electric fields in the TM_{110} pillbox cavity.

At this point, assuming the electrons travel through the center of the cavity ($r=0$) along the length, it is clearly obvious that the two cavities work differently, with the TM_{010} cavity utilizing the E-field to interact with the electrons, while the TM_{110} cavity uses the B-field. Also, as can be expected from the Lorentz formula, $\vec{F} = q(\vec{v} \times \vec{B} + \vec{E})$, an electron with initial velocity in the z-direction will have the z-properties affected by the TM_{010} cavity, while the transverse (x and y) properties will be affected by the TM_{110} cavity.

The field components of the TM_{010} mode in cylindrical coordinates, where $r = \sqrt{x^2 + y^2}$ and θ are the radial and azimuthal coordinates, respectively, are written as [2]

$$E_z = E_0 J_0(kr) \cos(\omega t), \quad 2.1$$

$$B_\theta = \frac{E_0}{c} J_1(kr) \sin(\omega t), \quad 2.2$$

where E_0 is the electric field amplitude, c is the speed of light in a vacuum, J_n is the n^{th} order Bessel function of the first kind, $k = \frac{\omega}{c}$ is the wave number, and $\omega = 2\pi f_0$ is the angular frequency which is related to the resonant frequency f_0 of the mode by 2π . For the TM_{010} mode, the boundary conditions force the electric field to go to zero as $r \rightarrow a$. This forces the inner portion of the Bessel function to be $ka = 2.4048$. For a monopole vacuum pillbox operating at $f_0 = 3$ GHz, this gives a radius of $a = 38.3$ mm.

The field components for the TM_{110} mode in cylindrical coordinates are compactly written, as [3]:

$$E_z = 2cB_0 J_1(kr) \cos(\theta) \sin(\omega t), \quad 2.3$$

$$B_r = \frac{2cB_0}{r\omega} J_1(kr) \sin(\theta) \cos(\omega t), \quad 2.4$$

$$B_\theta = \frac{2cB_0}{\omega} J_1'(kr) \cos(\theta) \cos(\omega t). \quad 2.5$$

Here the magnetic field amplitude B_0 is defined such that $B_y(r=0)=B_0$. Same as for the TM_{010} cavity, the boundary conditions determine the radius of the cavity; a quick comparison of Eq. (2.1) and (2.3) shows that the two Bessel functions are different. For the TM_{110} mode, the condition $ka=3.8317$ must be satisfied. For $f_0=3$ GHz, the radius of the TM_{110} mode vacuum pillbox cavity is $a=60.9$ mm. The number two arises in all of the equations for the dipole mode because the magnetic amplitude is defined as the magnetic field at $r=0$, as that is the area that the electrons will be interacting with the fields. Close to the z-axis the magnetic field components can be approximated using $\frac{1}{r} J_1(kr) \approx \frac{\partial}{\partial r} J_1(kr) \approx \frac{k}{2}$, holding only when $r \ll a$. This yields, near the z-axis, $E_\theta=2cB_0$. When translated to cartesian coordinates, this gives $B_x = 0$ and $B_y = B_0 \cos(\omega t)$ near $r=0$. However, because the pillbox is cylindrically symmetric, θ is arbitrarily defined, allowing B_x and B_y to be exchangeable.

It may be important to note that neither of the two modes depend on the length of the cavity, d , but instead only upon the radial size, a , which has been determined by the frequency being set to 3 GHz. This is an arbitrary frequency that has been chosen due to simplicity, well documented properties of materials at this frequency, cheap availability of equipment, and it is the 40th harmonic of 75 MHz. This last point is important for synchronization of the cavities with a 75 MHz Ti:Sapph laser oscillator.

The length of the cavity, d , is determined by the purpose of the cavity and the incoming electron energy. The two cavities have different purposes, as already briefly mentioned and will be described in detail further in this chapter. For now, suffice to say that the dipole mode is designed such that the length of the cavity corresponds to the distance traveled by electrons in half a period of the cavity, $d = \frac{v_e}{2f_0}$, where v_e is the velocity of the electrons and

f_0 the resonant frequency of the cavity. This is done to maximize the force from the magnetic field on traversing electrons. For 30 keV and 3 GHz, this gives a length of $d=17$ mm. The monopole mode was designed for the cavity length to be approximately equal to the fastest changing section of a sine curve for the given frequency and electron velocity; for a basic sine curve $\sin(\omega t)$, this corresponds to the nearly linear section around the zero crossing. This comes to $d=6$ mm for the TM_{010} mode, given the same energy and frequency.

2.1.2 Power, Energy, and Quality factor

Due to the simplistic shape of the pillbox cavity and well defined field patterns, the power lost to the surrounding walls as well as the energy stored in the fields can be calculated analytically as the perfectly conducting metal walls are replaced with copper. The ratio of the energy stored in the fields, U , and the power lost to the cavity, P_{loss} , is proportional to how well a resonator performs; this is quantized in the unit-less Quality factor, or Q for short, $Q = \frac{\omega U}{P_{loss}}$. In these calculations, the time dependence is neglected and attention is placed upon either the electric or magnetic fields. This time averaging is a shortcut taken because the fields have a 90 degree phase shift with respect to each other, so essentially the total power or energy in the cavity at any given time is constant, “sloshing” back and forth between the electric field and magnetic field. Solving through either field components can be accomplished.

The power loss within the vacuum pillbox cavity is entirely in the surrounding metallic conducting walls. The field equations (2.1-2.5) are derived from perfectly conducting walls; they are used perturbatively to calculate currents induced in the walls, and thus power lost to the walls. Taking an integral of the magnetic field parallel to the surface at the boundaries yields the time averaged power loss in the conducting walls [1].

$$P_{vac} = \frac{1}{2} \iint_{surface} \frac{|\vec{n} \times \vec{B}|^2}{\mu^2 \sigma \delta} dS. \quad 2.6$$

In Eq. (2.6), \vec{n} is the surface normal, μ is the permeability of the metal, σ is the conductivity of the metal, and $\delta = \sqrt{\frac{2}{\mu \omega \sigma}}$ is the frequency dependent skin depth. For the case of copper at 3 GHz, $\mu \approx \mu_0 = 4\pi \times 10^{-7} \text{ N A}^{-2}$, and $\sigma = 5.84 \times 10^7 \text{ } \Omega^{-1} \text{ m}^{-1}$ at a temperature of 298 K, resulting in a skin depth of $\delta = 1.2 \times 10^{-6} \text{ m}$ [2]. Solving Eq. (2.6) for the TM_{010} mode and TM_{110} mode yields,

$$P_{vac,010} = \frac{\pi E_0^2 a}{\sigma \delta c^2 \mu^2} (d+a) J_1^2(ka), \quad 2.7$$

$$P_{vac,110} = \frac{2\pi B_0^2 a}{\delta \mu^2 \sigma} (d+a) J_0^2(ka). \quad 2.8$$

The time averaged energy stored in the cavity can be calculated in a similar fashion, integrating over the volume of the cavity, rather than the surrounding walls.

$$U_{010} = \frac{1}{2} \iiint_{\text{volume}} (\epsilon |\vec{E}|^2 + \frac{1}{\mu} |\vec{B}|^2) dV = \frac{\pi E_0^2 a^2 d}{2c^2 \mu} J_1^2(ka), \quad 2.9$$

$$U_{110} = \pi dB_0^2 c^2 \epsilon a^2 J_0^2(ka). \quad 2.10$$

where $\epsilon = \epsilon_r \epsilon_0$ is the permittivity of the medium filling the cavity (in the case of vacuum, $\epsilon = \epsilon_0$ and $c = \frac{1}{\sqrt{\epsilon_0 \mu_0}}$). The use of a relative permittivity ϵ_r will be treated in the next section.

As previously mentioned, a unit-less quantity used to measure how well a resonator works is the Q factor. Shown previously $Q = \frac{\omega U}{P_{\text{loss}}}$, the Q factor is inversely proportional to the loss of power; it is clear that the highest Q possible is desired since larger Q means less power required. Solving for both modes yields the same result,

$$Q = \frac{1}{\delta} \frac{ad}{a+d}. \quad 2.11$$

For the TM_{110} mode, if a magnetic field amplitude of $B_0=3$ mT is desired for a vacuum filled copper cavity operating at 3 GHz, with a radius of 60.9 mm and length of 17 mm, a stored energy of $U_{110}=18$ μ J is found. For a copper cavity, the resulting power consumption is $P_{\text{vac},110}=393$ W, corresponding to a quality factor of $Q=11,100$. The equivalent Q for the TM_{010} mode is 4,300.

The cavity geometry greatly influences the Q of the cavity, as can be seen in Eq. (2.11). Deviations from the standard pillbox cavity can influence the Q; the TM_{110} cavity keeps the pillbox shape but is dielectrically loaded, reducing the size and power consumption of the cavity, which will be described in the next section.

2.2 Dielectric filled TM_{110} Pillbox

By inserting a dielectric material into the vacuum of the cavity, the properties of the standing wave modes are changed. The speed of propagation of the electromagnetic wave through the dielectric material is impeded by a factor $\sqrt{\epsilon_r}$, making $v_p = \frac{c}{\sqrt{\epsilon_r}}$. As a result,

the wave number $k = \frac{\omega}{v_p} = \frac{\omega\sqrt{\epsilon_r}}{c}$ is increased by a factor $\sqrt{\epsilon_r}$; logically following, the

cavity radius a , is decreased by the same factor $\sqrt{\epsilon_r}$. Finally, the ratio of the amplitudes of the electric to magnetic fields is decreased in a similar fashion to $\frac{E_0}{B_0} = \frac{c}{\sqrt{\epsilon_r}}$.

An ideal dielectric creates a reduction in the size of the cavity, thus decreasing the surface area of the metallic boundaries. Quick analysis of Eq. (2.8) with the previously mentioned corrections finds the ratio of power loss with an ideal dielectric P_{id} , to the power loss of a vacuum cavity P_{vac} in the TM_{110} mode to be

$$\frac{P_{id}}{P_{vac}} = \frac{1}{\sqrt{\epsilon_r}} \frac{(d/a_{vac} + 1/\sqrt{\epsilon_r})}{(d/a_{vac} + 1)}. \quad 2.12$$

where a_{vac} is the radius for the vacuum pillbox at the same frequency. Inspection of Eq. (2.12) shows it is clear that the power lost in an ideal dielectric will be less than in a vacuum filled counterpart. If $\epsilon_r \gg 1$, then $\frac{P_{id}}{P_{vac}} \propto \frac{1}{\sqrt{\epsilon_r}}$. New advances in ceramic materials have allowed

for the creation of dielectrics with $\epsilon_r \geq 40$ at GHz frequencies [4,5].

Ideal is, however, far from realistic, and reduction of power and size comes at the price of power loss in the dielectric. Treating the relative permittivity, ϵ_r , as a complex permittivity, $\epsilon_r = \epsilon' + i\epsilon''$, allows for the losses to be calculated analytically. By treating the imaginary part of the permittivity as a frequency dependent effective conductivity that induces a conduction current, the power loss within the fields is calculated as an integral over the volume of the dielectric:

$$P_d = \frac{\omega\epsilon''\epsilon_0}{2} \iiint_{vol} |\vec{E}|^2 dV = \frac{\pi\omega B_0^2 c^2 d\epsilon''\epsilon_0 a^2}{\epsilon'} J_0^2(ka). \quad 2.13$$

Using Eq. (2.12) and (2.13), the following equation is arrived upon for the power loss in a TM_{110} cavity filled with a lossy dielectric:

$$\frac{P_{id} + P_d}{P_{vac}} = \frac{1}{\sqrt{\epsilon'}} \frac{(d/a_{vac} + 1/\sqrt{\epsilon'})}{(d/a_{vac} + 1)} + \frac{\epsilon''}{\epsilon'^2 \delta} \frac{d}{(d/a_{vac} + 1)}. \quad 2.14$$

where a_{vac} is the radius in the vacuum cavity. Comparison between the stored energy U and the power loss in the dielectric P_d (Eq. (2.10) and (2.13), respectively) shows a difference of $\frac{\omega \epsilon''}{\epsilon'}$, as expected by the equation $P = \frac{\omega U}{Q}$. Logically following, the Q for the dielectric is determined to be [6]

$$\tan \delta = \frac{\epsilon''}{\epsilon'} = \frac{1}{Q_{dielectric}}, \quad 2.15$$

where $\tan \delta$ is known as the loss tangent, and is often used in the case of dielectric materials. With many materials the relative permittivity is large and the loss tangent is low, meaning $\epsilon' \gg \epsilon''$, thus allowing the approximation $\epsilon' \approx \epsilon_r$.

By taking the entire power loss $P_{loss} = P_{id} + P_d$ as a summation of the losses in the reduced size cavity and the losses to the dielectric, and selecting a material with a large ϵ_r and small $\tan \delta$, it is possible to design a pillbox cavity that is smaller in size and requires less power to obtain the same desired field patterns and amplitudes along the z -axis.

Figure 2.4 is a contour plot of Eq. (2.14) as a function of ϵ_r and $\tan \delta$. The curves indicate lines of constant P_{loss}/P_{vac} . The symbols represent various materials that are well known, taken from Ref. [6]. The square and star represent the dielectric material chosen for the TM_{110} cavity, measured at 10 GHz by the company that produces it, and 3 GHz in our lab.

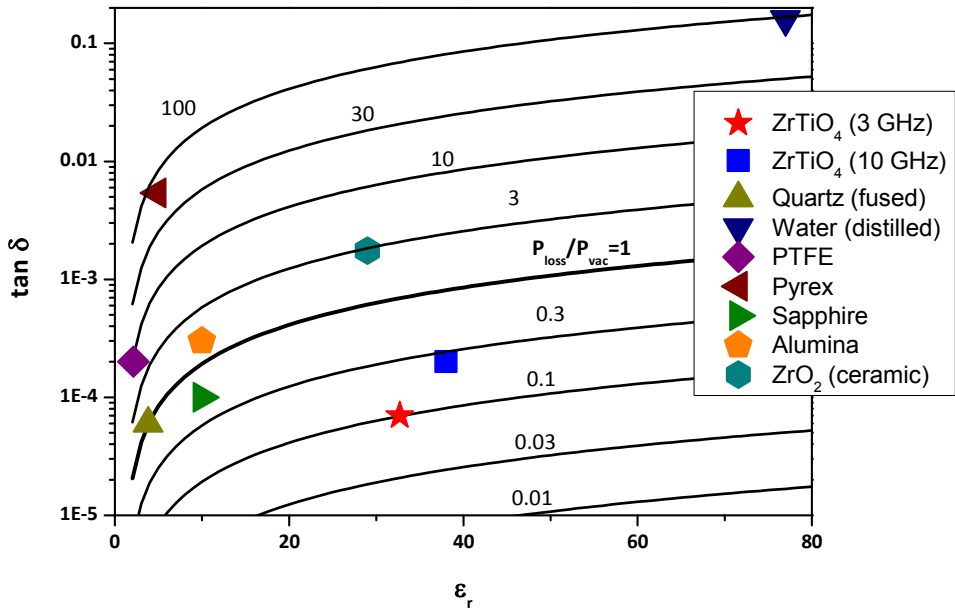


Figure 2.4: A contour plot of $P_{\text{loss}}/P_{\text{vac}}$ as a function of $\tan \delta$ and ϵ_r . The lines represent values of constant $P_{\text{loss}}/P_{\text{vac}}$. The symbols represent various common dielectric materials and their typical values measured at 3 GHz. The blue square represents the material chosen, measured at 10 GHz, while the red star represents the same material measured at 3 GHz.

By carefully choosing an appropriate dielectric with a large relative permittivity and low loss tangent to fill the cavity, power loss can be reduced to less than a tenth of the power consumption a vacuum filled pillbox cavity requires for the same field amplitude and frequency.

2.3 Comparison of Vacuum and Dielectric filled Pillbox

The dielectric chosen is a ZrTiO_4 ceramic doped with $<20\%$ SnTiO_4 , seen in Fig. 2.4. The relative permittivity was quoted by the company, T-Ceram, s.r.o., as $\epsilon_r = 36.5\text{-}38$ in the frequency range 0.8-18 GHz, with a loss tangent of $\tan \delta = 2 \times 10^{-4}$ measured only at 10 GHz [5]. The desired operating frequency is 3 GHz, with a magnetic field amplitude of 3 mT, designed for 30 keV electrons (it is clear that a beam of electrons will not traverse through a dielectric, so deviations from a fully filled dielectric cavity must be taken; this will be discussed in Sect. 3.1.1). Table 2.1 shows the differences obtained in size and power consumption between the dielectric and vacuum cavities, with the given parameters aforementioned.

	Vacuum Pillbox	Dielectric Pillbox
Radius	60.9 mm	10.6 mm*
Length (d)	17.1 mm	17.1 mm
Power loss	393 W	45 W*

Table 2.1: Comparison of sizes and power consumption between vacuum and dielectric filled 3 GHz pillbox cavity with a magnetic field amplitude $B_0=3$ mT. The asterisk (*) is used to denote when the measured values at 3 GHz for permittivity and loss tangent are used for calculations.

The table clearly shows a reduction in both the radial size of the cavity, as well as the power consumption. The length of the cavity does not change size, as the length is determined by the incoming speed of the electrons and the resonant frequency.

The Q of the dielectric cavity is related to the loss tangent as shown in Eq. (2.15). The total Q of the dielectric filled cavity would be correlated with the following relation [1,6]

$$\frac{1}{Q_{cavity}} = \frac{1}{Q_{id}} + \frac{1}{Q_{diel}}. \quad 2.16$$

Combining Eq. (2.16) with Eq. (2.15), using the quoted loss tangent, and finding from Eq. (2.11) that $Q_{id} \cong 5300$, the final calculated unloaded Q of the entire cavity is 2600. Due to the reduction in size from the dielectric, and taking into account the loss tangent, the total power consumption for the dielectric filled cavity would be about 45 W to maintain a field magnitude of 3 mT, a large contrast from nearly 400 W for the vacuum pillbox.

2.4 Principle of RF Compression (TM_{010} cavity)

As previously mentioned, the TM_{010} cavity has an electric field oriented in the z-direction along the $r=0$ axis. This electric field can be used to manipulate the longitudinal properties of electrons traversing it. And because the field is time dependent, the manipulation of the electrons is dependent upon the phase of the electrons with respect to the cavity.

One way to create fs electron bunches is to shine a fs laser pulse onto a photocathode. This allows for the extraction and acceleration of fs electron bunches. However, in order to achieve a diffraction image from a single bunch, roughly 10^6 electrons must be contained in the bunch for sufficient resolution of the diffraction peaks. When the laser is focused to a radius of 25 μm in combination with the fs time scale, the current density of the million

electrons in the tiny volume ($\sim 60,000 \mu\text{m}^3$) creates a repulsive field on the order of $\sim \text{MV/m}$ within the bunch. This will cause the electron bunch to expand in all directions as the electrons are repelled away from each other [2].

To correct for the expansion in the transverse directions (x, y), solenoids are used to focus the beam back down. This does nothing to correct for the rapid expansion in the z -direction. This longitudinal expansion causes the original fs electron bunch created by the laser at the photocathode to rapidly expand into tens of ps before it can be used.

The TM_{010} compression cavity was designed to reverse this expansion, and compress an electron bunch spatially along the longitudinal axis. As the bunch approaches the cavity, it is expanding longitudinally. If the cavity is matched to the correct phase, the front of the bunch that is speeding away fastest will be struck with an electric field oriented in z and with opposite sign from the direction of the front electron, causing it to slow down. As the center of the bunch passes, it is at just the right phase so that it does not have any overall effect to its speed longitudinally from the cavity. As the electrons at the back, which are going the slowest and stretching the bunch, enter the cavity, they are met with an electric field that has reversed sign and is accelerating the back electrons towards the rest of the bunch. The net effect is that longitudinally, the electrons are focused. This longitudinal focusing is directly proportional to the temporal resolution.

Using Eq. (2.7), assuming a field amplitude of $E_0=6 \text{ MV/M}$ in the cavity to offset the expansion of the bunch, the power consumption of a pillbox cavity is found to be more than 5 kW. For this reason, a power efficient shape was designed and commissioned as part of a photocathode driven project [2].

The TM_{010} cavity was designed specifically to compress high charge electron bunches to fs temporal resolutions. The scope of this thesis focuses on the cavity's ability to manipulate longitudinal properties of a charged particle beam, expanding upon the specific design parameters of the cavity and offering useful experimental possibilities in combination with the TM_{110} cavity. For more details on the design and construction of the TM_{010} cavity, see Ref. [2].

2.5 Principle of RF Chopping (TM₁₁₀ cavity)

Previously in the chapter, the approximation $\frac{1}{r}J_1(kr) \approx \frac{\partial}{\partial r}J_1(kr) \approx \frac{k}{2}$ was used to determine the magnetic field amplitude on the z-axis where the electrons will interact with the field. If this approximation is fed back into the field equations, and converted to Cartesian coordinates, it is found that along the $r=0$ axis the magnetic field behaves the same as a uniform magnetic field \vec{B} oscillating with amplitude B_0 and radial frequency $\omega=2\pi f_0$:

$$\vec{B} = B_0 \cos(\omega t + \varphi_0) \hat{y}, \quad 2.17$$

with t being the time and φ_0 the phase of the field at time $t=0$.

Consider an electron moving along the z-axis with velocity $\vec{v} = v_e \hat{z}$. A slit of size s is placed at a distance l from the cavity, along the z-axis, as seen in Fig. 2.5. With the cavity centered around $z=0$, the slit extends over the range $-\frac{s}{2} \leq x \leq \frac{s}{2}$ at $z = l + d/2$.

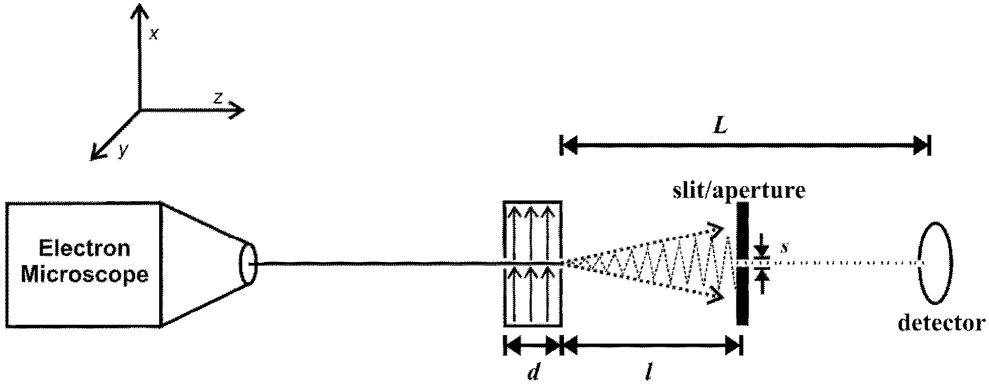


Figure 2.5: General schematic demonstrating the basic principle of RF chopping with a TM₁₁₀ cavity and slit. The arrows in the cavity represent the transverse force.

Since the transverse velocity gained by traversing the cavity will be much smaller than v_e , we approximate the velocity through the cavity as $\vec{v} \approx v_e \hat{z}$. The Lorentz force $\vec{F} = q\vec{v} \times \vec{B}$ acting on the electron will thus lead to a momentum kick in the x-direction:

$$\bar{p} = \frac{qv_e B_0}{\omega} [\sin(\omega t_1 + \varphi_0) - \sin(\varphi_0)] \hat{x}, \quad 2.18$$

with $t_1 = d / v_e$ being the cavity transit time. The maximum deflection

$$p_{x,\max} = -\frac{2qv_e B_0}{\omega} \sin(\varphi_0), \quad 2.19$$

occurs for $t_1 = \pi / \omega$, corresponding to a transit time equal to half of a period of the cavity, i.e. a cavity length given by $d = \pi v_e / \omega$, as mentioned earlier in this chapter. The corresponding sweep angle α of the electron trajectory with the z-axis is given by

$$\alpha(\varphi_0) = \frac{p_{x,\max}}{mv_e} = -\frac{2qB_0}{m\omega} \sin(\varphi_0), \quad 2.20$$

where the small angle approximation was used. Only those electrons will get through the slit whose entrance phase is such that the sweep angle is smaller than the angle subtended by the slit, i.e. $|\alpha(\varphi_0)| < s / 2l$. Since the slit is centered on the z-axis and, following from Eq. (2.19), $|\varphi_0| \ll 1$, it stands to reason that only those electrons will get through the slit whose entrance phase φ_0 lies in the range

$$-\frac{sm\omega}{4lqB_0} < \varphi_0 < \frac{sm\omega}{4lqB_0}, \quad 2.21$$

corresponding to a bunch length

$$\tau \equiv \frac{\Delta\varphi_0}{\omega} = \frac{sm}{2lB_0q} \quad [7]. \quad 2.22$$

To achieve a bunch length of ~ 100 fs, modest values of $s=10 \mu\text{m}$, $l=10$ cm, and $B_0=3$ mT are needed. To realize an oscillating magnetic field of 3 mT with minimal power consumption, a resonant RF cavity is used.

In practice, the TM_{010} cavity is vacuum filled but takes a unique shape to conserve power, while the TM_{110} cavity utilizes a dielectric filled pillbox shape to conserve power. In principle, a dielectric pillbox could be used for the TM_{010} cavity, but is expected to not be advantageous as far as power is concerned. This is because dielectrics in general suppress external electric

fields; to be power efficient, the TM_{010} cavity would have to be loaded with a high relative permeability (μ_r) material which also possesses a low magnetic loss tangent. No materials hold these properties and are easily accessible to the current knowledge of the author.

2.6 Conclusion

The two types of cavities used in this project, the TM_{010} compression cavity and the TM_{110} streak cavity, have been presented. The general characteristics of the cavities were described, including equations to predict the energy in a given field, and the power required to produce a given field amplitude. A dielectric filled TM_{110} cavity was presented, and compared to the vacuum equivalent. By choosing an appropriate dielectric, it was shown that the power consumption and size of the cavity can be reduced, but at the cost of the Q factor, i.e. how well the cavity resonates.

Once the general description of the cavities were given, the general operation of the cavities was discussed: the TM_{010} cavity uses the electric field to manipulate the longitudinal properties of an electron bunch, while the TM_{110} cavity was designed to streak a DC electron beam transversely across a slit to generate ultrashort electron bunches at a high repetition rate. The temporal length of any given electron bunch using this method is given by Eq. (2.22). It is shown that with the modest field amplitude and slit size of 3 mT and 10 μm , respectively, that 100 fs electron bunches can be generated, all for under 50 W of power with the dielectric filled cavity.

References

- [1] W.K.H. Panofsky, and M. Phillips. *Classical Electricity and Magnetism*. Menlo Park: Addison-Wesley Publishing Company, 1978.
- [2] van Oudheusden, T. *Electron Source For Sub-Relativistic Single-Shot Femtosecond Diffraction*. Eindhoven: TU Eindhoven, 2010. Thesis.
- [3] Lee, S.Y. *Accelerator Physics*. 2. Singapore: World Scientific, 2004.
- [4] National Magnetics Group. "National Magnetics Group." n.d. <www.magneticsgroup.com/tci>.
- [5] TCI Ceramics. "t-ceram dielectric resonators." n.d. *TCI Ceramics, s.r.o.* <www.t-ceram.com/dielectric-resonators.htm>.
- [6] A.W. Chao, and M. Tigner. *Handbook of Accelerator Physics and Engineering*. Singapore: World Scientific, 1999.
- [7] Lassise, A., P.H.A. Mutsaers and O.J. Luiten. "Compact, lowpower radio frequency cavity for femtosecond electron microscopy." *Review of Scientific Instruments* 83 (2012): 043705.

3 TM₁₁₀ Cavity Design and Characterization

In the previous chapter, the general analytical solutions for a standard TM₁₁₀ dielectric filled pillbox cavity were described. However, in order to make the cavity useful in practice, certain alterations must be made from the pillbox design.

The alterations that must be made to the cavity are to accommodate the electrons passing through the cavity, coupling RF power into the cavity, mode degeneracy breaking, and frequency tuning. All of these are achieved with three alterations from the pillbox cavity: a hole through the center, side ports, and breaking cylindrical symmetry. The effects of each will be presented and discussed. The final technical drawings of the cavity can be found in Appendix A.5.

To assure that the cavity still operates similar to the pillbox cavity, the cavity is simulated in CST Microwave Studio [1], giving the electromagnetic field patterns to compare with the analytical pillbox described in Ch. 2.

Before final implementation into a beam line, the microwave characteristics of the cavity are measured. The power consumption, magnetic field profile, frequency tuning, and temperature dependence are all measured and discussed.

3.1 Construction

A more detailed technical drawing of the entire cavity can be found in Appendix A.5. The core of this section discusses why the alterations from an ideal pillbox were made.

3.1.1 Electron pathway

The starting point for the design is a pillbox cavity of radius $a = \frac{3.8317}{k\sqrt{\epsilon_r}}$ and length

$d = \frac{v_e}{2f_0}$, as seen in Fig. 2.1 in the previous chapter; with the company quoted $\epsilon_r \approx 37.25$,

$f_0 = 3$ GHz, and $v_e \approx \frac{c}{3}$, the dimensions of the dielectric inside the pillbox are found to be

$d = 17.1$ mm and $a \approx 10$ mm. The surrounding metal is chosen to be copper, for its high conductivity, low cost, and ease of manufacturing.

The first step is to add a pathway for the electrons to traverse the cavity. Previous trial testing revealed that the dielectric material will accumulate charge and disturb the beam to

the extent that beam quality will be degraded and even lost from detection. To avoid this charging, the diameter of the hole through the dielectric is made to be 3 mm, while that in the copper is cut at 2 mm, seen in Fig. 3.1. This allows for the high brightness beam to traverse the cavity without any charging effects.

3.1.2 Side ports

The pillbox does not resonate on its own, and needs power fed into it. This is accomplished by means of a hertzian dipole loop antenna [2,3], seen in Fig. 3.1. By extending the inner conductor of a coaxial cable into the cavity and creating a loop that then shorts to the outer conductor, a magnetic flux is created through the loop. Matching the magnetic flux from the loop with the magnetic field of the mode allows for power to be coupled into the cavity. Matching is achieved by rotating the loop. The magnetic coupling of the antenna with the cavity is chosen at the outer side wall, far away from the electron pathway, to avoid any field disturbances from the antenna along the $r=0$ axis. For these reasons, a loop antenna was chosen over a dipole shorted antenna.

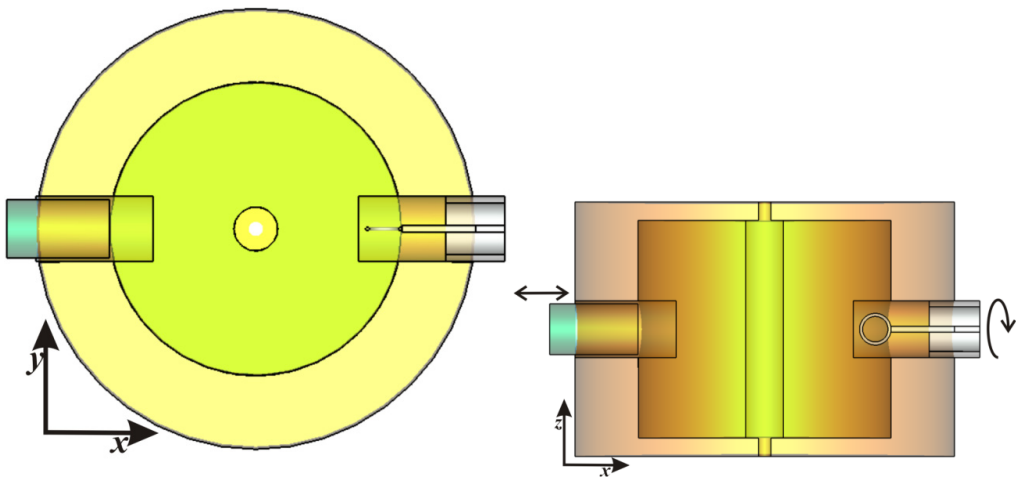


Figure 3.1: A dielectric filled pillbox cavity with side ports added for a frequency tuner and loop antenna for RF power to be fed into the fields.

For frequency tuning, a second port of the same diameter, 4.5 mm, is added on the opposite side of the antenna port, keeping symmetry, seen in Fig. 3.1. As a dielectric plunger is inserted into the port, the amount of dielectric in the cavity is increased and thus the frequency decreases. If a metallic plunger is inserted, the effective radius of the cavity decreases, causing the frequency to shift upwards.

As can be seen in Fig. 3.1 above, the tuning and coupling ports are opposite one another in one of the (arbitrary) x/y directions. Because the cylinder is rotationally symmetric, there is no preference and thus no difference in frequency between the degenerate TM_{110} modes oriented in the x and y directions in the absence of ports. The additional ports break the rotational symmetry and thus lift the degeneracy of the two modes, see Fig. 3.2, and separate the frequencies. This allows the driving of only one mode, as desired. Utilizing the two separate modes will be discussed further in Sec. 6.2.1.

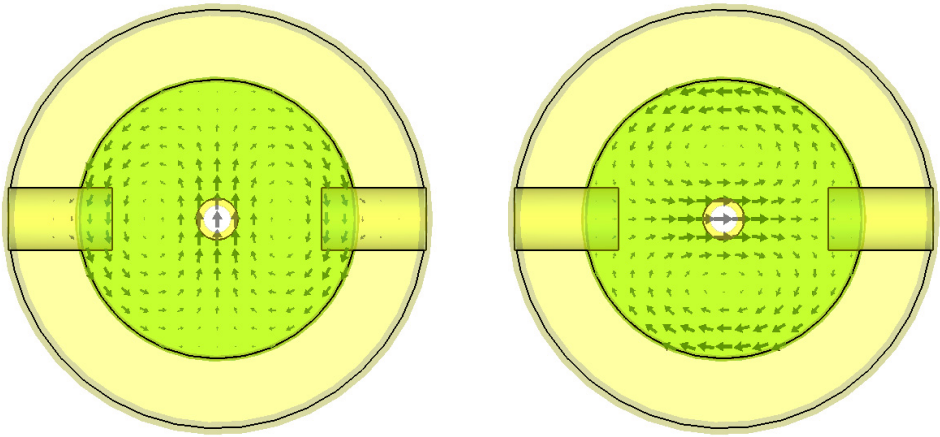


Figure 3.2: Visual of the two TM_{110} modes, which are degenerate in a rotationally symmetric cylindrical cavity.

3.1.3 Elliptical shape

Initial tests and measurements of the dielectric at 3 GHz showed that the relative permittivity was $\epsilon_r \cong 32.7$, instead of 37. As a result, the dielectric filled pillbox cavity had a resonant frequency that was above a drivable frequency with oscillators at the disposal of this project. To reduce the resonant frequency, vacuum gaps were added at the positions of the ports by making the cavity elliptical.

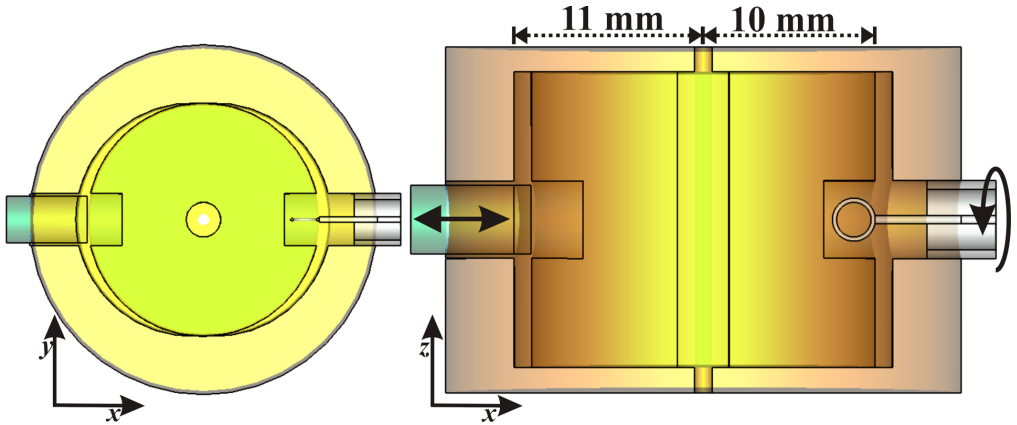


Figure 3.3: Realistic dielectric filled cavity. The expanded radius in one direction further reduces the frequency to the intended operating frequency.

The new elliptical shape keeps the same transverse width in one direction to 20 mm, while increasing the transverse width in the other direction to 22mm. In addition to bringing the frequency into the desired tunable oscillator bandwidth, the extension of the radius in one direction further separates the degenerate modes to a peak-to-peak distance of approximately 100 MHz, as will be shown in the next section.

3.2 CST Microwave Studio Simulations

The cavity is no longer a rotationally symmetric pillbox. Due to technical constraints, the cavity has been altered; and as discussed in Ch. 2, the cavity's dimensions play an important and influential role upon the characteristics of the cavity. The realistic dielectric filled cavity is modeled in CST Microwave Studio [1] to determine deviations in the characteristics of the cavity from that of the ideal pillbox, particularly field profile characteristics along the beam trajectory at $r=0$.

As previously mentioned, the relative permittivity was not as high as expected, leading to deviations from the initial pillbox cavity. To determine the proper ϵ_r , the frequencies of the two TM_{110} modes in simulations were matched with experiment, as seen in Fig. 3.4.

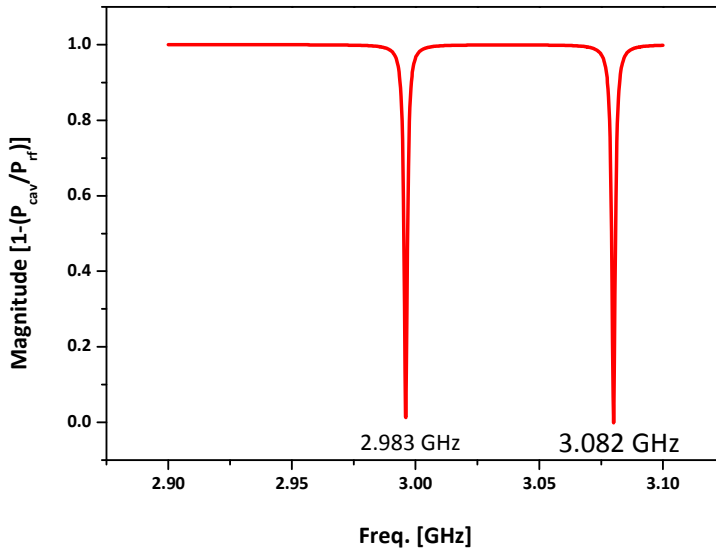


Figure 3.4: Two TM_{110} modal frequencies after alterations to cavity.

To ensure that the field has not changed significantly along the interaction volume, the normalized magnetic field amplitudes B/B_{max} along the axis $r=0$ are shown in Fig. 3.5, both for an ideal pillbox cavity and the actual cavity geometry (Figs. 2.1 and 3.3, respectively).

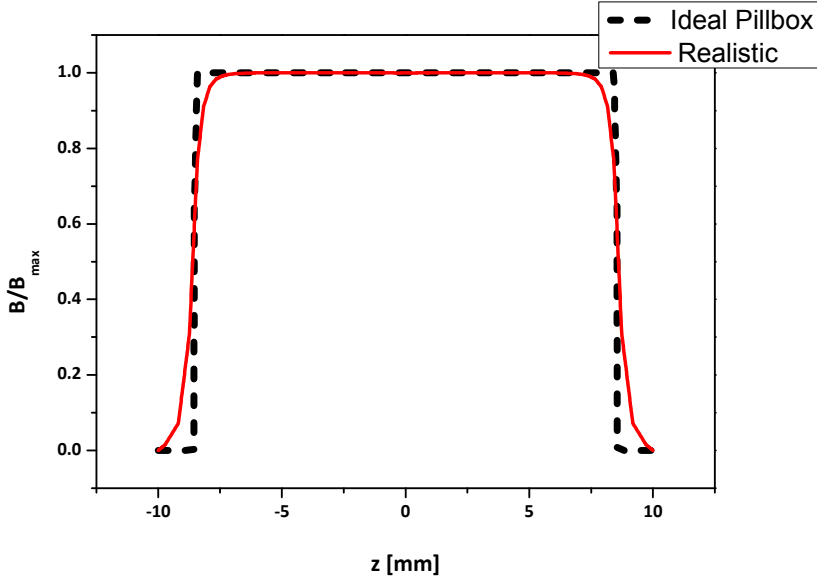


Figure 3.5: The magnetic field profile along the longitudinal axis of the cavity at $r=0$ for the realistic cavity geometry (red solid line) and the ideal pillbox cavity (black dashed line).

As can be seen, the adjustments to the cavity have not significantly disturbed the ideal field configuration desired for the cavity.

To appropriately simulate losses and Q factor, the quoted loss tangent $\tan \delta = 2 \times 10^{-4}$ was also taken into account. As a result, the Q of the pillbox was calculated to be 2600, while that of the final cavity to be 2650; a negligible change in the Q of the cavity. With this, it is reasonable to assume power loss can be approximated with equations for the perfect pillbox, despite the alterations made to the ideal case.

3.3 RF Cavity Characterization

In this section, the cavity's operational characteristics are tested and checked before implementation into a beam line. The power absorption spectrum is measured, yielding the Q factor and loss tangent. Following is a field profile measurement along the longitudinal axis. Next, a measurement of the frequency shift as a result of the tuning stub insertion depth is presented, demonstrating the frequency tunability of the cavity. Finally, the temperature dependence of the frequency is measured with the implications in turn discussed.

3.3.1 Power Absorption

The ratio of the power absorbed by the cavity P_{cav} and the incident power P_{rf} as a function of frequency is described by a Lorentzian curve with a full-width-at-half-maximum

$FWHM = \frac{2f_0}{Q_d}$ when impedance matched. Figure 3.6 shows the absorption spectrum taken from a network analyzer and a Lorentz curve fit.

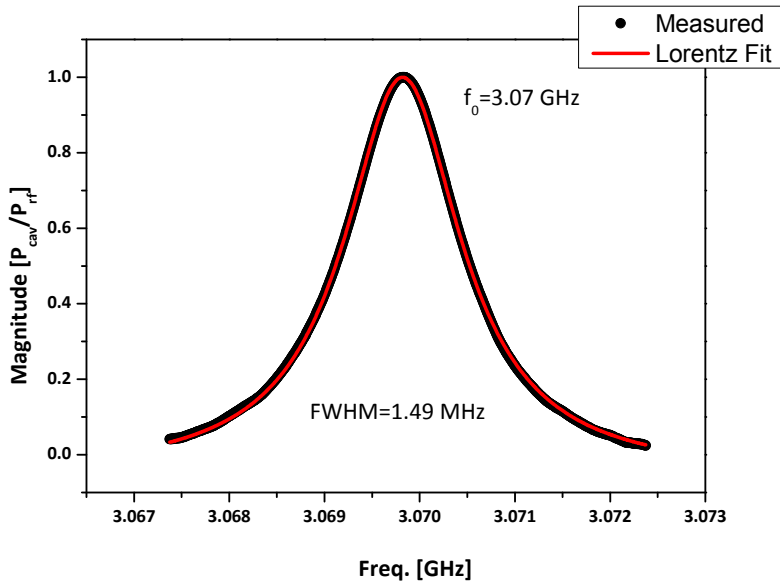


Figure 3.6: The absorption spectrum of the cavity as a function of frequency with a Lorentzian fit.

The total Q for the entire cavity is measured to be $Q_d=4100$. This is not in agreement with the simulated $Q=2650$, but suggests better. Using the calculated $Q_{id}=5300$ from Sec. 2.3, and Eq. (2.16), the measured loss tangent is found to be $\tan \delta=5.5 \times 10^{-5}$. This falls much lower than the company quoted value $\tan \delta=2 \times 10^{-4}$, making the power loss lower than expected. The large differences between the measurements and quoted values for the relative permittivity and loss tangent could be accounted for in the high frequency dependence of both the real and imaginary parts of the permittivity, particularly as the company's quoted value was measured at 10 GHz, while the cavity is operated at 3 GHz. Simulations in CST using $\tan \delta=5.5 \times 10^{-5}$ gives a total $Q_d=4250$. This is much closer in agreement to the measured value of 4100.

3.3.2 Field Profiles

For measuring the field profile along the electron trajectory, we make use of the so-called “bead pull” method, based on the perturbation method of Maier and Slater [4]. Slater demonstrated in 1952 that the local electric and magnetic field amplitudes of a cavity can be measured by means of a small perturbation at the same position of the fields inside the cavity. This perturbation manifests a shift in frequency following the formula,

$$\omega^2 = \omega_0^2 \left(1 + \int_{V_{pert.}} (b_n^2 - e_n^2) dV \right). \quad 3.1$$

In Eq. (3.1), ω is the perturbed radial frequency, ω_0 is the unperturbed radial frequency, and b_n and e_n are proportional to the unperturbed magnetic and electric field amplitudes, normalized so that the integral of b_n^2 or e_n^2 over the entire cavity volume is unity; the integration in Eq. (3.1) is over the volume $V_{pert.}$ of the perturbation. For very small volumes, e_n and b_n are to a good approximation constant across the volume $V_{pert.}$ If, in addition, the frequency shift is very small, $|\omega - \omega_0| \ll \omega_0$, then Eq. (3.1) can be reduced to a proportionality [4]:

$$\frac{\Delta\omega}{\omega_0} \propto b_n^2 - e_n^2, \quad 3.2$$

where $\Delta\omega = \omega - \omega_0$. The importance of the proportionality is that the shift in frequency is directly dependent upon the strength of the unperturbed fields at the point of perturbation. In the case of the dielectric cavity, a small perturbation was taken in the form of a cylindrical piece of metal of radius 0.25 mm and length 1 mm, secured to a fishing line. The piece of metal is pulled through the cavity, along the z-axis. According to (3.2), a shift up in frequency relates to a magnetic field, while a shift down in frequency will correspond to an electric field. The size of the metal used was as small as possible so as to fit through the cavity without touching the sides, yet large enough to detect a frequency shift on the network analyzer. A larger piece of metal would give a larger shift in frequency, but would cause a drop in the spatial localization of the measurement. Looking back at Fig. 2.2 and 2.3, it can be seen that as the metal bead is pulled down through the TM_{010} cavity, the frequency will shift down due to the electric field; the metal bead pulled through the TM_{110} cavity will cause an increase in the frequency due to the magnetic field.

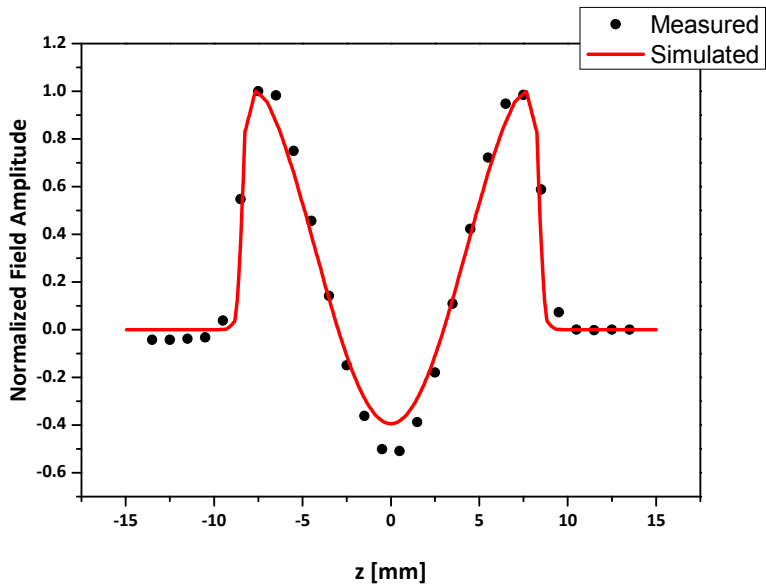
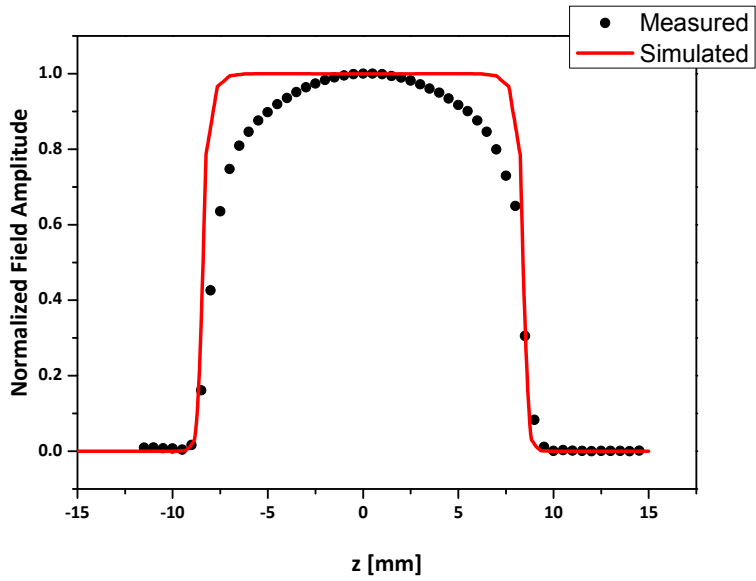


Figure 3.7: Field profile measurements (black circles) and calculated field profiles (red solid curve) of the TM_{110} mode and TE_{010} mode, normalized by the magnetic field amplitude B_0 at $r=0$.

Figure (3.7) compares the measured field profile to the field profile calculated with CST Microwave Studio for the TM_{110} mode and TE_{010} mode. The general shape gives clear

evidence that this is a TM_{110} mode since the frequency shift is in the correct direction pointing to a large magnetic field and little electric field at the position of the metal on the fishing line. The discrepancies appearing when the metal bead is close to the copper shell enclosing the dielectric material, can be attributed to mirror charges [5], but also to electric fringe fields which are found in simulations and discussed further in Sec. 5.2.1. To illustrate how effective the bead-pull method is for identifying the resonant modes at hand, shown in Fig. 3.7b is a field profile measurement of a higher frequency mode that is resonant within the cavity. Notice in Fig. 3.7b that the two peaks at the beginning and the end are positive while the trough in the center is negative correlating to a magnetic and electric field, respectively. With this in mind and comparing to simulations, it was determined that the mode is a TE_{010} mode oriented such that a transverse electric field component exists, rather than longitudinal, while the magnetic field runs azimuthally around the transverse electric component. Correct mode identification is important for the determination of the measured ϵ_r and frequency.

3.3.3 Tuning Screw

A dielectric tuning stub was made from the same dielectric material as the inner portion of the cavity. The tuning stub is inserted into the side of the cavity, entering through the vacuum area, and into the dielectric filling inside of the cavity, seen in Fig. 3.3 on the left side of the cavity. Since more dielectric is added to the effective volume of the cavity, the frequency decreases. Figure 3.8 shows this behavior; as the dielectric tuning stub is inserted into the port, the frequency shifts down.

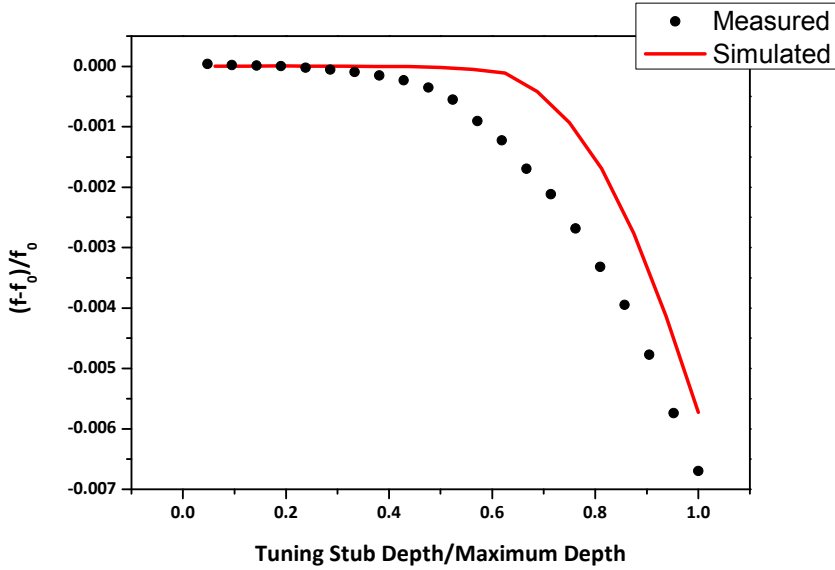


Figure 3.8: Frequency shift versus the depth of the dielectric tuning stub, measurement (black dots) plotted against CST Microwave Studio simulation (red solid curve).

The tuning range with the dielectric tuner is a maximum of 21 MHz, in reasonable agreement with CST Microwave Studio simulations. The difference between simulations and measurements may point to anisotropy in the relative permittivity [6] or the dielectric filling shifting inside the cavity.

3.3.4 Temperature Dependence of Frequency

As described in Ch. 2, the use of realistic materials leads to power losses in the fields. Because the losses occur directly in the material of the cavity, be in dielectric or copper, the losses cause the cavity to heat up. As metal heats up, it expands, creating a larger radius and in turn causes the frequency to shift downward. For any $TM_{l,m,0}$ mode, the frequency shift is given as [7]

$$\frac{\partial f}{\partial T} = \frac{-x_{l,m} c}{2\pi\sqrt{\epsilon_r}} \frac{1}{a} \frac{\partial r}{\partial T} = -f_0 \kappa_T, \quad 3.3$$

where $x_{l,m}$ is the m^{th} zero of the l^{th} order Bessel function and κ_T is the thermal expansion coefficient. For the TM_{110} mode, $x_{11}=3.8317$ and for copper, $\kappa_T=16.4 \times 10^{-6} \text{ K}^{-1}$. For a copper vacuum pillbox cavity operating in the monopole or dipole mode at 3 GHz, the shift in frequency as a function of the change in temperature is calculated to be $\Delta f/\Delta T=-51 \text{ kHz/K}$.

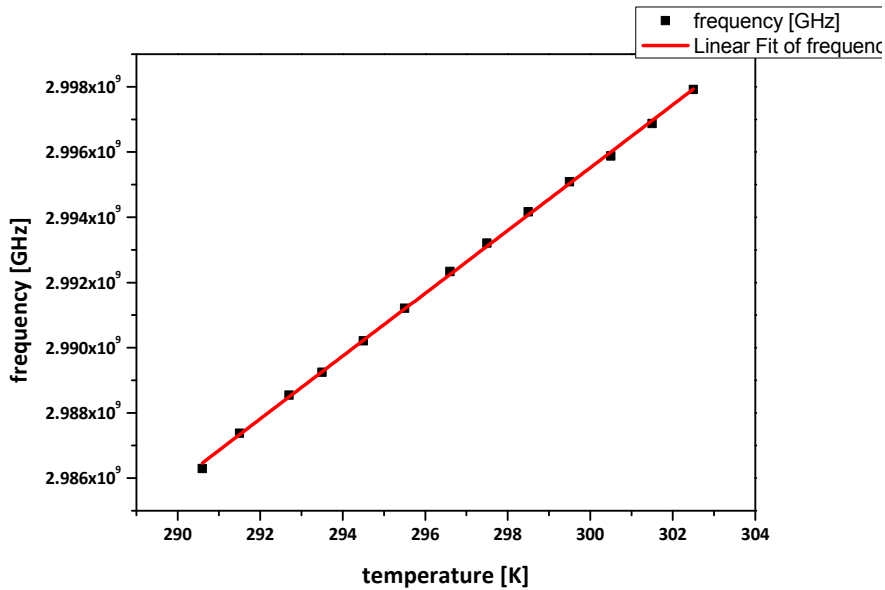


Figure 3.9: Resonant frequency of the TM_{110} dielectric cavity as a function of temperature. The change in frequency is found to be 963 kHz/K.

Adding the dielectric greatly changes the overall thermal properties of the cavity. The cavity was attached to a temperature stabilization unit, and the temperature was scanned across values near room temperature. A linear fit shows that for the dielectric TM_{110} cavity that has been constructed, a frequency shift of $\Delta f/\Delta T=963$ kHz/K. This is an order of magnitude larger than the vacuum cavity, and in the opposite direction. This suggests to either a negative thermal expansion coefficient which is unlikely or the more probable temperature dependent relative permittivity [6].

Because the frequency is so sensitive to temperature change, a practical way to achieve frequency tuning in situ is by changing the setting of the temperature stabilization unit. Also, because of the large frequency sensitivity, the temperature stabilization unit has to be very accurate. The temperature stabilization unit used is an in-house water cooling design using a peltier element as well as a heating element to stabilize the cavity at a temperature between 20° and 45° celsius, with a standard deviation from the mean of 1.2 mK over 14 hours. This corresponds to a resonant frequency deviation in the cavity of 1.1 kHz; to maintain stable field amplitudes, the frequency drift of the cavity should be $<1/10$ of the FWHM seen in Fig. 3.6, or about 150 kHz. From this it is clear that the temperature stabilization device gives more than the required frequency stability to drive the cavity on resonance for long periods of time with stable field amplitudes.

3.4 Conclusion

The final construction, found in Appendix A.5, was described in detail in Sec. 3.1. The cavity, based upon a dielectric filled pillbox, was altered to accommodate the electrons traversing the cavity, coupling RF power to the cavity, frequency tuning, and mode degeneracy breaking. It was found that the cavity had very nearly the same behavior as the standard pillbox cavity, allowing for the basic analytical equations of Ch. 2 to apply.

The mode of the cavity was determined beyond a reasonable doubt using the bead-pull method, measuring the field profile of the cavity. The magnetic field profile was found to agree with simulations, confirming that the TM_{110} mode was in fact at the appropriate and expected resonant frequency.

The temperature dependence of the cavity was found to be opposite to a vacuum cavity, and have a sharper gradient. This implies that in order to operate the cavity for long periods of time, the temperature must be accurately controlled, which we have also done. It also means that once in the beam line, slight adjustments to the resonant frequency of the cavity can be done by raising or lowering the temperature stabilization point.

In addition to using the temperature as a frequency shifter, it was demonstrated that with a dielectric tuning screw, the frequency can be shifted downwards, while a metal tuning screw can tune the frequency upwards. This gives a larger range of control to properly tune the cavity to the desired resonant frequency.

Finally, the two degenerate modes of the cavity were separated to avoid operating the same mode in two orthogonal directions. This was done on purpose, but will be re-considered and discussed further in Sec. 6.2.1.

The TM_{110} dielectric cavity was designed and commissioned for operation in a beam line. Before implementation, the microwave characteristics of the cavity had to be checked to ensure that the cavity operated as expected. The power consumption, field profile, field strength, and resonant frequency all performed as expected. The cavity works and is suitable for implementation into a beam line.

References

- [1] Computer Simulation Technology. "CST Microwave Studio 2011 User Manual." n.d. *CST Microwave Studio 2011*. <www.cst.com>.
- [2] Orfanidis, S.J. *Electromagnetic Waves and Antennas*. Camden: Rutgers University Press, 2010.
- [3] Pozar, D.M. *Microwave Engineering*. 3. Hoboken: Wiley, 2005.
- [4] L.C. Maier, Jr., and J.C. Slater. "Field Strength Measurements in Resonant Cavities." *J. Appl. Phys* 23 (1952): 68.
- [5] Kiewiet, F. *Generation of Ultra-Short, High-Brightness Relativistic Electron Bunches*. Eindhoven: TU Eindhoven, 2003. Thesis.
- [6] L.F. Chen, C.K. Ong, C.P. Neo, V.V. Varadan, and V.K. Varadan. *Microwave Electronics: Measurement and Materials Characterization*. West Sussex: Wiley, 2004.
- [7] van Oudheusden, T. *Electron Source For Sub-Relativistic Single-Shot Femtosecond Diffraction*. Eindhoven: TU Eindhoven, 2010. Thesis.

4 Experimental Setup and Beam line

In this chapter, the implementation of the dielectric TM_{110} cavity in an altered electron microscope beam line is discussed. Streaking of the electron beam is demonstrated, and the length of the streak is measured for various input powers. The beam line in question was designed and built for this project. It consists of an old W-hairpin XL-30 (30 keV) scanning electron microscope (SEM) that was disconnected from the sample chamber, and placed horizontally on an optical table. With the SEM mounted horizontally and used as an electron source, a beam line of up to 2 ½ meters can be implemented downstream of the microscope, with easily accessible and changeable sections placed in and out of the beam for whatever is desired and necessary for the experiment in progress.

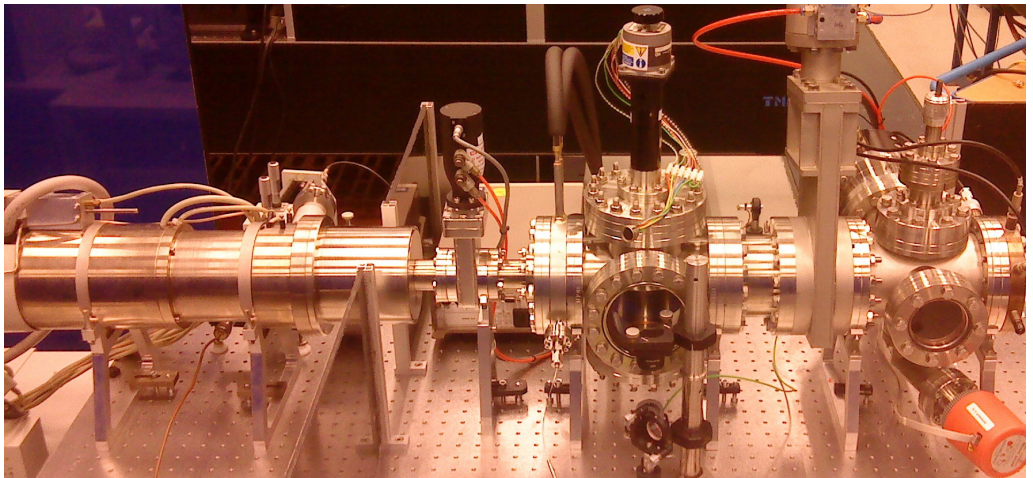


Figure 4.1: 30 keV SEM table top Beam line. Starting from left: SEM column, valve, TM_{110} cavity with cooling hoses, 6-sided cube with port windows on the side and manipulator on top connected to the slit, valve, 6-sided cube with linear translation stage and vacuum pressure gauge, and MCP.

Because the large size of the optical table, the extra room makes it suitable for an optical beam line to be built on the table with ease, as will be discussed further in Sec. 7.4. The beam line is also oriented North-South, to minimize the effect of the Earth's magnetic field on the electrons since the field does not run completely perpendicular to the table's surface plane. Finally, the beam line is kept relatively close to the optical table, and all electronic equipment is kept either far away from the table or under the table, allowing the table to act as a grounding plane isolating the beam from unwanted stray fields.

4.1 Implementation

The entire beam line was designed and built with CF flanges, to create an easily changeable beam line. The core of the beam line is broken into three parts as can be seen in Fig. 4.2. The first section is the SEM, which provides a high quality stable electron beam. After the SEM is the TM_{110} dielectric cavity and a slit which can be moved in and out of the beam line as desired. Finally, following the cavity and slit is the rest of the beam line, which can be extended up to 2 meters. In this third area, depending on the experiment, we implemented beam pipes, steering coils, solenoids, quadrupoles, alignment grids, extra cavities, phosphor screens, and samples on TEM grids. This section will detail these three parts in more detail. All three sections are separated by valves, which allows for a single section to be vented and opened and worked on, while the other two remain in vacuum conditions.

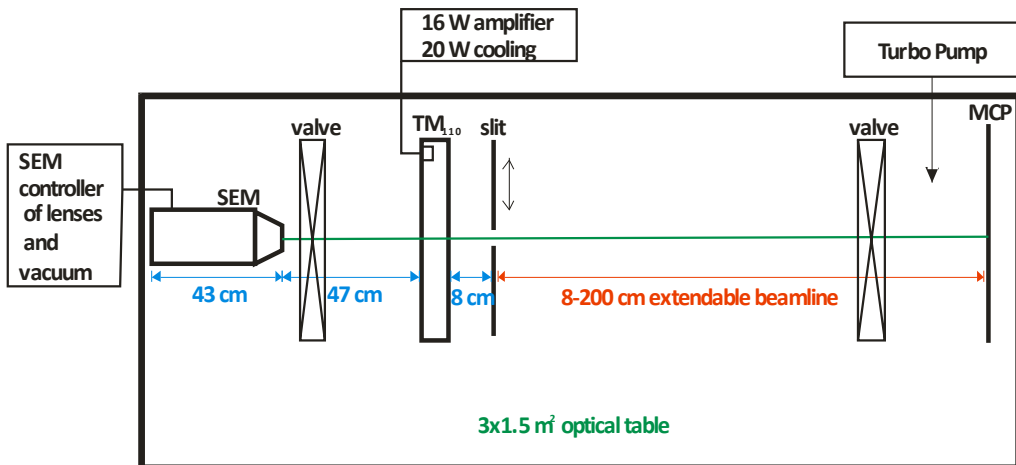


Figure 4.2: General schematics of the beam line of a 30 keV SEM on an optical table. The entire system is controlled by two vacuum pumps, one located on the SEM control area, the other located near the MCP. The valves are used so that only part of the system that requires changing can be vented while the rest is kept under vacuum. The red arrow represents the part of the beam line that was regularly changed with various beam pipes, translation stages, ports, steering coils, focusing magnets, and samples, depending on the experiment at hand.

4.1.1 30 keV SEM

The entire beam line is schematically shown in Fig. 4.2. The SEM is an XL-30 keV W-hairpin emitter mounted in a Wehnelt cylinder, originally built by Philips, and donated by FEI [1]. It was dismantled from the sample chamber, and placed horizontally along the optical table, seen in Fig. 4.1 on the far left.

The SEM is controlled by the original system software on another table, only connected to the optical table by the cables running to the SEM column and a vacuum pipe. The maximum probe current achievable from the system is 2 μ A. To control the beam, the SEM is put into “spot” mode, and the DC coils in the SEM are used to adjust the beam. The final lens of the SEM is used for focusing. In order to focus the beam beyond the 10 cm maximum distance it was designed for, a master key to override the system software was supplied by FEI, allowing for the current to the final lens to be adjusted beyond the initial parameters of the machine.

The SEM was originally designed to be fitted with either a W-hairpin, or a field emission gun (FEG) [1]. The tungsten hairpin in general is easier to replace and is more durable and reliable at higher pressures. On the other hand, the FEG gives a higher quality beam. Through the entire project, a W-hairpin was used. However, as will be shown in Sec. 7.3.1, a higher quality beam may be useful and advantageous for future experiments.

The SEM was also designed for differential pressure zones, allowing for environmental SEM work. The column would be kept at a low pressure, while the sample chamber could be brought to a much higher pressure. The entire beam line was built much in the same way; the SEM has its own turbo pump, which only pumps down the SEM column, while the rest of the beam line following the SEM is pumped down by a second turbo pump, with sealable valves placed in between. This was done for practical reasons, for working on the beam line, rather than environmental electron microscopy.

4.1.2 TM_{110} Dielectric Cavity

The design and testing of the dielectric TM_{110} cavity was discussed previously in Ch. 3, with detailed technical descriptions given in Appendix A.5. To mount the cavity in the beam line, a special 100 CF flange was altered, seen in Fig. 4.3. The flange had four feed-through ports welded on to it. The first two are for water cooling, one for the flow in, the other the flow out. These water ports were connected to a copper cooling baseplate, which the cavity is mounted to.

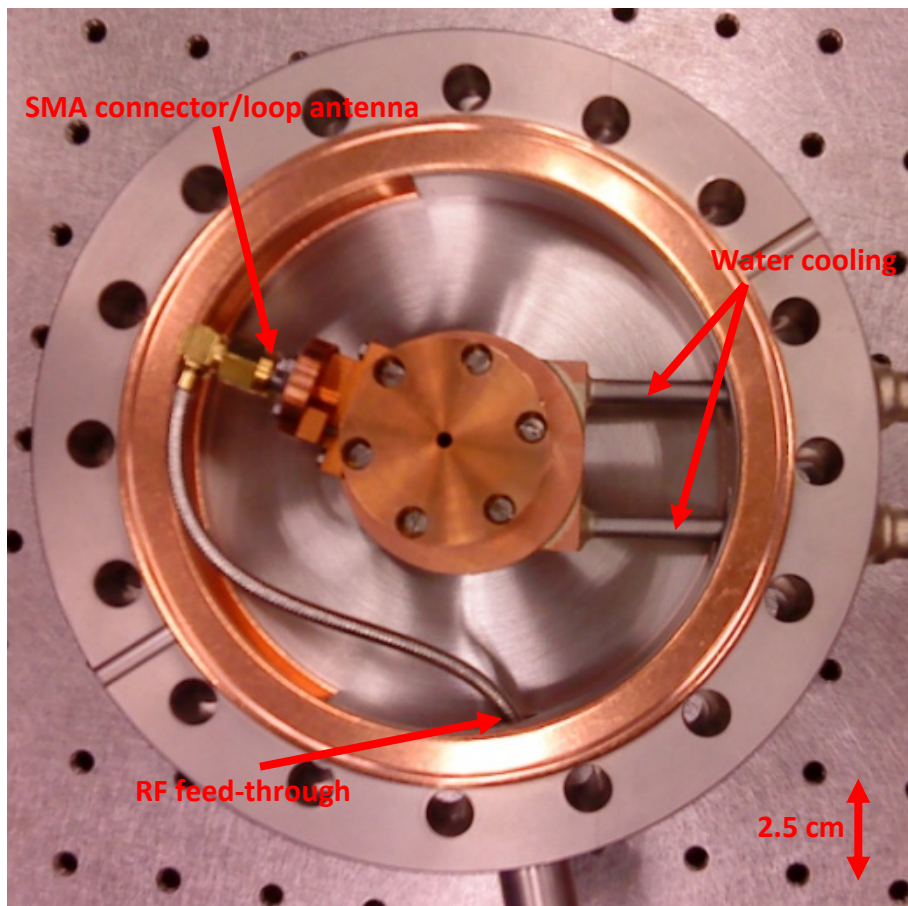


Figure 4.3: The dielectric filled TM_{110} cavity mounted on a 100 CF flange with RF feed-through (bottom) and two water cooling pipes (right). The thermocouple feed-through cannot be seen in this photo.

The third port on the flange is to connect a thermocouple to the cavity, for a feedback loop to control the temperature (not seen in Fig 4.3). To cool the cavity, an in-house tunable peltier cooling unit was built. The maximum cooling of the unit is 20 W, tunable between 20° and 45° Celsius. Once the temperature has stabilized to the set point, the cavity would remain temperature stable to a standard deviation of 1.2° mC.

The fourth port on the flange is for the RF input. The chosen size for the coaxial connector both at the feed-through and on the cavity is SMA. As can be seen in Fig. 4.2, the cavity is fed power by a 16 W peak continuous-wave amplifier. The amplifier is powered by a tunable 3 GHz oscillator, although it is also capable of working with the oscillator designed by Kiewiet *et al.* which synchronizes to a 75 MHz laser oscillator with <20 fs precision [2].

Because of the location of the feed-throughs for water, power, and a thermocouple; and the mounts holding the beam pipe in place above the optical table, the cavity is incapable of being mounted so that the magnetic field in the cavity is perpendicular or horizontal to the table. For this reason, all of the pictures of a streak are slanted with a 27° tilt from the vertical, as will be seen later in Fig. 4.5.

4.1.3 Extensions

As shown in Fig. 4.2, the beam line can be extended up to 2 meters beyond the cavity/slit area. It is in this area that detection was carried out. Figure 4.2 shows an MCP placed at the end of the beam line for detection. However, with a beam current of up to 2 μA , the single plate MCP would easily be damaged. For this reason, a single phosphor screen was often mounted at the end of the beam line, along with a port window. Instead of the port window, a Faraday cup could also be placed at the end of the beam line, though this was rarely done.

The Earth's magnetic field was previously mentioned, with the beam line pointed North-South to minimize the effects of the field. This is only true for the horizontal component of the field, since the field usually points about 60° up from the horizon. This still leaves a vertical component which causes the beam to curve roughly 1 cm for every meter of beam line. In general, when the beam line is extended beyond ~1.5 meters total, from the back of the SEM forward, steering coils are usually needed to correct the beam back on course.

It was in this area that a quadrupole and solenoid were placed so as to do quadrupole waist scan emittance measurements, discussed further in Ch. 5. A TM_{010} cavity was placed in this extended area to demonstrate phase control between two cavities, which will be shown in Sec. 6.3. To power the TM_{010} cavity, a second cooling unit and a 200 W pulsed amplifier were added to the setup. The same oscillator was used with the signal split in two, one sent to the streak cavity, the other through a phase shifter and then on to the compression cavity.

Because the beam line was designed in three sections, they are divided into three parts by two valves. The SEM column has its own turbo pump, with a valve placed just in front of the SEM, completely controlled from the original SEM software. Following the TM_{110} cavity and slit, a second valve was placed. Behind this valve a second turbo pump was placed, just before the MCP. This is to ensure that the MCP was kept under vacuum conditions at all times, even when the beam line is vented and being changed around. The two vacuum pumps were capable of bringing the system down to a pressure of $<10^{-7}$ mbar.

4.2 Testing

The cavity, seen in Fig. 4.3, was mounted in the augmented SEM horizontal beam line by a 100 CF flange. Power was then fed to the cavity with a tunable 16 W peak continuous wave amplifier, allowing for a maximum magnetic field amplitude of $B_0=2.15$ mT. The water cooling is capable of keeping the cavity at a stable temperature with a drift of ~ 1 mK. The schematics as implemented are seen in Fig. 4.3.

Figure 4.4 is a beam on a phosphor screen from a 30 keV SEM at a distance $L=55$ cm from the cavity with no power fed in. Figure 4.5 is an image of the phosphor screen with $P_{rf}=3.2$ W RF power fed into the cavity, giving rise to a streak length of $\chi=15$ mm, corresponding to a magnetic field amplitude $B_0=0.7$ mT.



Figure 4.4: Electron spot on detector with no power fed to the cavity.

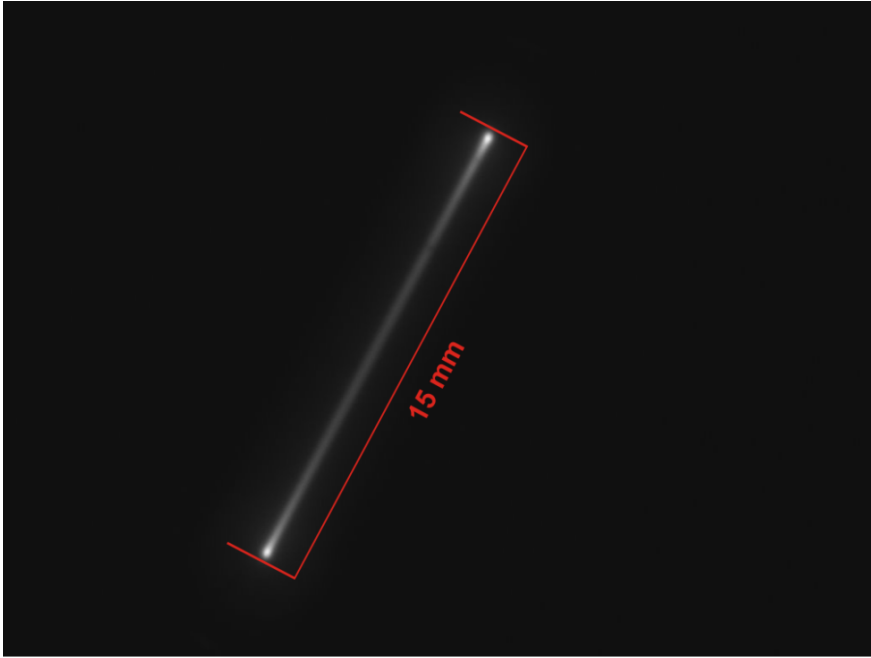


Figure 4.5: Streak electron beam on detector with $P_{rf}=1.6$ W power fed to the cavity. The streak is slanted because of the mounting of the TM_{110} cavity.

According to theory, the magnetic field amplitude required for a streak length χ is given by

$$B_0 = \frac{m\omega}{4Lq} \chi, \quad 4.1$$

where the relation $\chi=2L\alpha(\varphi_0=\pi/2)$ was used, with $\alpha(\varphi_0)$ taken from Eq. (2.20); $\varphi_0=\pi/2$ corresponds to a maximum deflection for the incoming electrons. Plugging Eq. (4.1) into Eq. (2.14), along with $\epsilon_r=32.7$ and $\tan \delta=5.5 \times 10^{-5}$, the theoretically required RF power P_{rf} is found, which is plotted in Fig. 4.6.

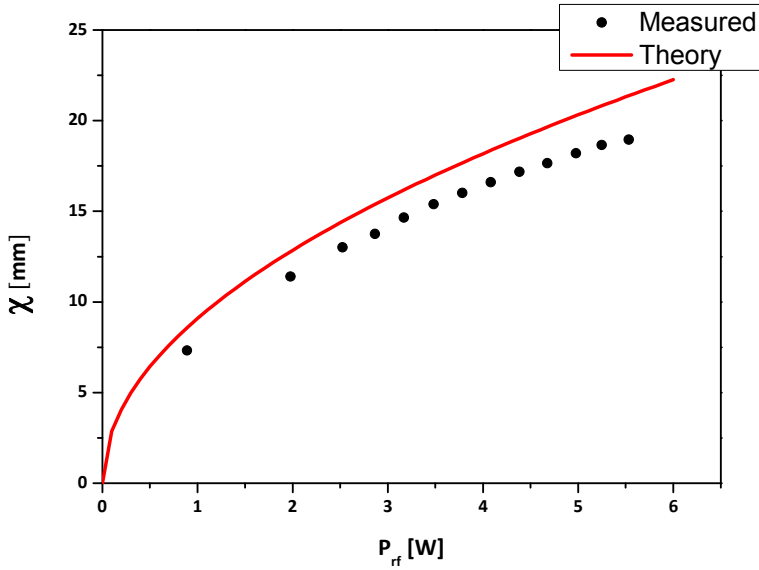


Figure 4.6: Theoretical (red solid line) and measured (black dots) streak length of the electron beam at the detector as a function of RF input power. The deviation of the measured points from the theoretical line may be attributed to losses in the coax line, as well as initial issues with the cooling unit.

Streak length χ was measured for various settings of RF input power P , as shown in Fig. 4.6. Calculating back from the highest measurement point on Fig. 4.6, it is found that with an input power of 16 W, a field amplitude of 2.15 mT is obtained in the cavity. A slit size of 10 μm at a distance of 10 cm after the cavity would result in 130 fs pulses. Satisfactory agreement between theory and measurements is obtained: the system performs as expected. At higher power input, the cavity was operated at a higher temperature, which possibly explains the small discrepancy between the measurements and the theoretical predictions. Konaka observed an increase in loss tangent at higher temperatures for many ceramic materials, including ZrO_2 , which could account for the difference [3]. Another explanation is that the cooling unit was not operating at full capacity, but had issues at the time, which was later found to be a piece of plastic wedged in the flow meter.

4.3 Conclusion

The building of a durable, reliable beam line was presented. A 30 keV W-hairpin scanning electron microscope (SEM) was donated from FEI, and altered to build a 3 meter long beam line. The SEM is used as an electron source, giving a high quality beam which can be controlled very accurately using the original SEM software and a master key to provide more control over the SEM column than the machine was originally designed for. Once mounted on an optical table, the rest of the beam line is divided into two parts: the TM_{110} streak cavity with a slit to generate ultrashort electron bunches, and then an area to do something with the bunches.

The TM_{110} streak cavity was built small enough to completely fit inside the vacuum tubes. It was mounted on a CF100 flange with water cooling for temperature stabilization, and an RF feed-through for the power. The initial testing of the cavity with a beam proved fruitful, as the cavity worked as it was designed and as Ch. 3 predicted it would.

The last portion of the beam line is where experiments upon the chopped beam were carried out. In this area, any charged particle optics that are necessary can be added: TM_{010} cavity, solenoids, quadrupoles, samples, and beam stops to name a few. All of these and more will be discussed in more detail in Ch. 5 and Ch. 6.

The beam line has proven to be a durable and reliable system delivering a high quality electron beam with a high precision of spatial control over the beam. The TM_{110} cavity works as designed; producing ultrashort electron bunches from a well-defined DC beam. Because of the length of the beam line, a number of experiments can be carried out, some of which will be discussed further in Ch. 5, 6, and 7.

References

- [1] FEI Company. "FEI Internal Document." n.d. *FEI Company*. <www.fei.com>.
- [2] F.B. Kiewiet, A.H. Kemper, O.J. Luiten, G.J.H. Brussard, M.J. van der Wiel. "Femtosecond synchronization of a 3 GHz RF oscillator to a mode-locked Ti:sapphire laser." *Nuclear Instruments and Methods in Physics Research A* 484 (2002): 619-624.
- [3] T. Konaka, M. Sato, H. Asano, and S. Kubo. "Relative permittivity and dielectric loss tangent of substrate materials for high-Tc superconducting film." *J. Supercond.* 4 (1991): 283.

5 Beam Dynamics

A dielectric loaded transverse magnetic 110 mode (TM_{110}) cavity was designed and commissioned for creation of fs electron bunches at a high repetition rate inside an electron microscope [1]. The principle of the setup works as follows: a DC electron beam traverses the center of the pillbox cavity. When the cavity is switched on, the TM_{110} mode resonates at 3 GHz. The magnetic field, oscillating perpendicular to the electrons, causes the electron beam to be streaked in one transverse direction. By placing a slit or aperture downstream from the streak cavity, ps or even fs electron bunches are created at a high repetition rate, illustrated in Fig. 5.1.

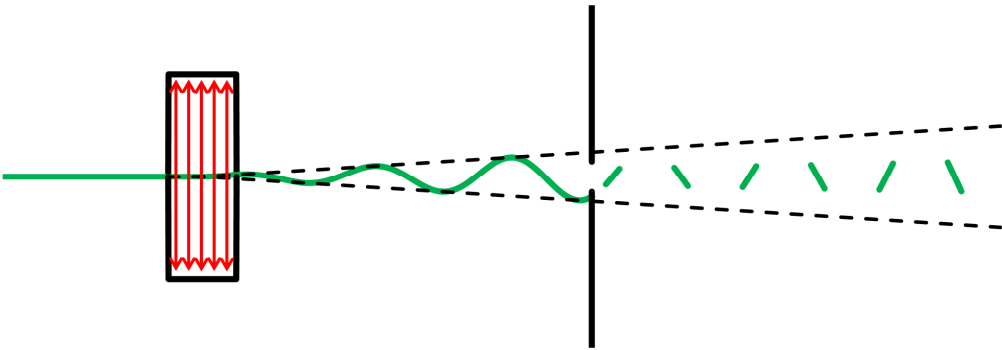


Figure 5.1: General schematic for operation of cavity to create temporally short electron bunches. The red arrows represent the Lorentz Force felt by the electrons, alternating back and forth sinusoidally. The picture is not given to scale for demonstrative purposes.

As can be seen, the general premise is simple and straightforward, but the devil is in the details. The temporal length of the electron bunches after the slit is dependent upon the magnetic field amplitude B_0 experienced by the electrons and the ratio of the slit size to that of the distance from the cavity to the slit (Eq. (2.22)). With the required field amplitudes of up to $B_0 \sim 10^{-2}$ T and $E_0 = cB_0 \sim 10^6$ V/m, it is not immediately clear whether the beam is disrupted or affected, or if the beam quality is completely lost all together.

The purpose of this chapter is to examine and analyze how the beam quality of the electron bunches is affected by traversing the cavity. First an analytical model will be built up to predict the normalized transverse emittance and the longitudinal energy spread for the case of a collimated beam and of a focused beam, seen in Fig. 5.2. Following, the analytical model will be compared to numerical simulations with the simulated fields of the actual cavity that has been built. It is found that the highly simplified model applies quite well with

realistic charged particle tracking simulations. After the comparison of the analytical model and numerical simulations, measurements demonstrating the behavior predicted will be presented. Finally, a general overview of the beam characteristics due to the cavity will be discussed.

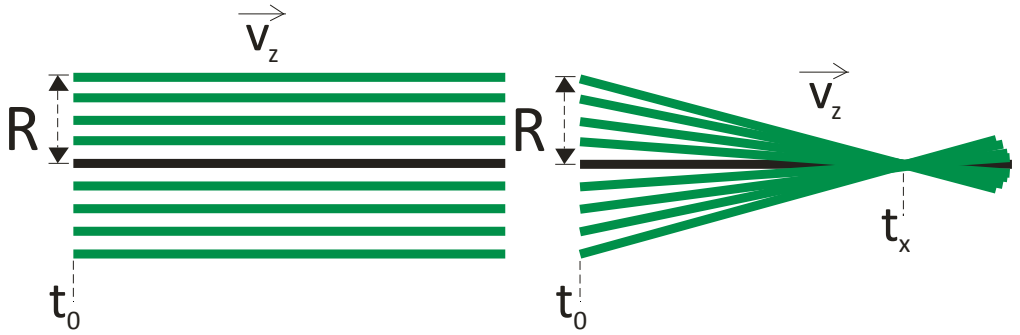


Figure 5.2: On the left, a collimated beam (or parallel beam) of radius R and velocity v_z is pictured. To the right, a focused beam (converging before t_x , diverging after t_x) of radius R at time t_0 focused at point t_x is seen.

5.1 Analytical Model

In this section, a simple analytical model is built up to predict the behavior of an electron bunch through the TM_{110} streak cavity. This model predicts the position, momentum, normalized transverse emittance and energy spread of a temporally short electron bunch created using the dielectric TM_{110} cavity.

5.1.1 Momentum and Position

To begin, the TM_{110} cavity is modeled as a uniform magnetic field oriented in y with amplitude B_0 oscillating with radial frequency ω and length $d = \frac{\pi v_z}{\omega}$ centered around $z=0$, just as was justified and used in Sec. 2.5. To a good approximation, it can be considered that the electron's velocity in the z -direction v_z is constant through the entire cavity, allowing the time/position dependence to be written as $v_z t = z$, giving for the magnetic field

$$\vec{B}(\vec{r}, t) = B_0 \sin(\varphi + \omega t) \hat{y} \quad \text{when } t_b \leq t \leq t_e. \quad 5.1$$

To reduce equations and variables, the cavity shall be positioned around the point $z=0$, giving the time $t=0$ the moment when the electrons are at the center of the cavity and the so called entrance phase φ is the phase at the moment $t=0$; because the cavity length is designed to be a half period, it follows that the beginning and end times are $t_b = -t_e = -\frac{\pi}{2\omega}$ [1]. It is clear from the Lorentz force that an electron traversing the cavity ($t_b \leq t \leq t_e$) will have

a transverse force imparted upon it in the x-direction. Subsequently, this velocity gained in x will result in a change in the z-momentum, but as this would be a higher order effect, it is neglected. This x-directed force will lead to a momentum kick and thus position change in x. This can be “tracked” through the cavity with the appropriate integration limits. In Eq. (5.2) and Eq. (5.3), the constants $p_0 = \frac{B_0 q v_z}{\omega}$ and $x_0 = \frac{B_0 q v_z}{m \omega^2}$ are used.

$$p_x = \frac{B_0 q v_z}{\omega} (\cos(\varphi + \omega t) - \sin(\varphi)) = p_0 (\cos(\varphi + \omega t) - \sin(\varphi)), \quad 5.2$$

$$\begin{aligned} x &= \frac{B_0 q v_z}{m \omega^2} \left(\cos(\varphi) - \left(\frac{\pi}{2} + \omega t\right) \sin(\varphi) + \sin(\varphi + \omega t) \right) \\ &= x_0 \left(\cos(\varphi) - \left(\frac{\pi}{2} + \omega t\right) \sin(\varphi) + \sin(\varphi + \omega t) \right) \end{aligned} \quad 5.3$$

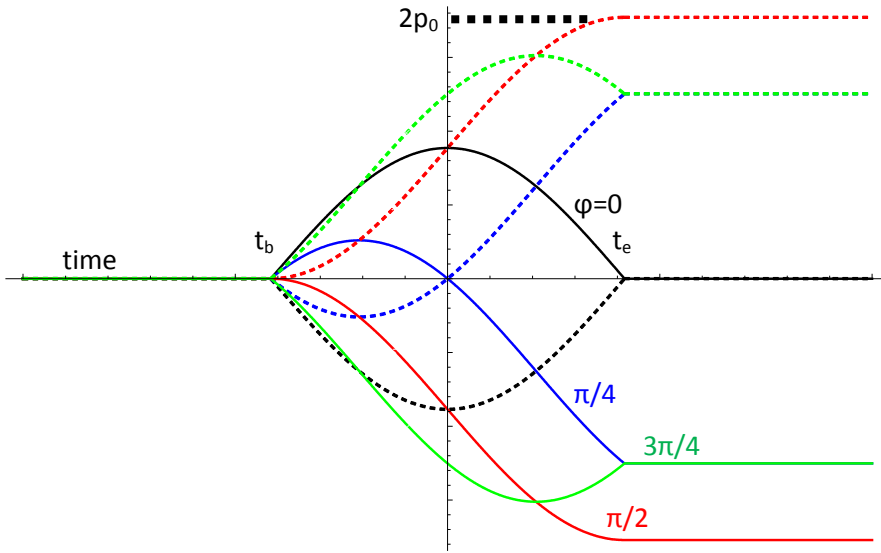


Figure 5.3: Momentum in the x-direction as the electron traverses the cavity using Eq. (5.2) for various entrance phases φ . The solid colors correspond to the following entrance phases: Black=0, Blue= $\pi/4$, Red= $\pi/2$, Green= $3\pi/4$; the dotted lines correspond to the same phase with a π phase shift.

From Fig. 5.3 it is clear that the momentum gained due to the cavity is strictly dependent upon the phase. It is also convenient for naming that the black line gives a zero net momentum as that is the zero phase case. Looking forward to Fig. 5.4, it is clear that the zero phase case will give an offset in x, while the $\varphi = \pi/2$ (red) case will give a maximum deflection after some time to propagate after the cavity.

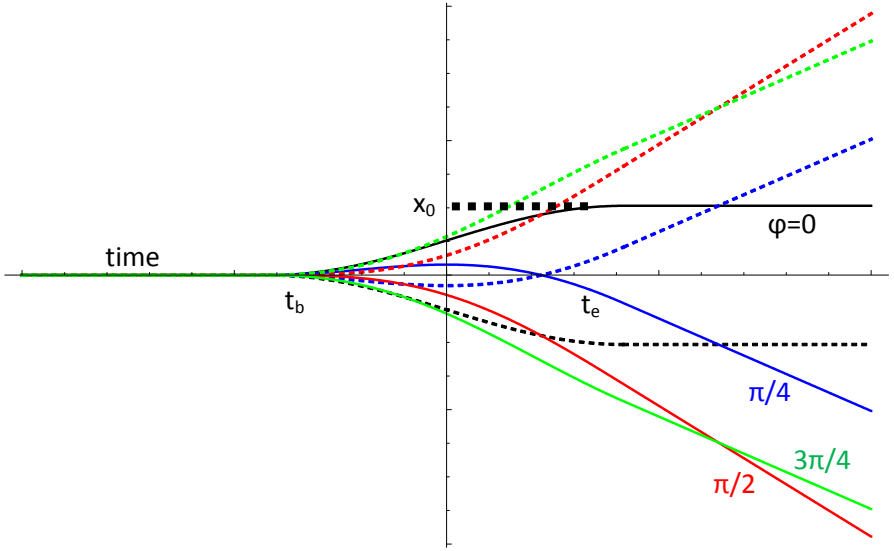


Figure 5.4: Position change as electron traverses the cavity from Eq. (5.3). The colors represent the various entrance phases, color coded the same as Fig. 5.3.

Equations (5.2) and (5.3) describe the behavior of an electron through the cavity. Because the cavity chops a small section out of a DC beam, we shall now consider what happens to a small section, or bunch, of electrons traversing the cavity.

5.1.2 Emittance

A figure of merit for the quality of a beam is the current density per unit solid angle, or brightness. However, since beams are moving in a preferred direction (z in our case), higher acceleration energies lead to smaller angles and thus a higher brightness. To compare beams of different energies, the reduced brightness should be used, defined as $B_r = \frac{Jq}{\pi kT}$, where J is the current density, q is the elementary charge, and kT is the effective source temperature. It can be shown that the reduced brightness can be written as $B_r = \frac{2q}{mc^2} \frac{I}{4\pi\epsilon_{N,x}\epsilon_{N,y}}$, where $\epsilon_{N,x}$ is the so-called root mean square (rms) normalized emittance in the x -direction [2],

$$\epsilon_{n,x} \equiv \frac{\sqrt{\langle x^2 \rangle \langle p_x^2 \rangle - \langle xp_x \rangle^2}}{mc}, \quad 5.4$$

where the brackets represent the short hand for the statistical values, written out as $\langle x^2 \rangle = \langle (x - \langle x \rangle)^2 \rangle$, $\langle p_x^2 \rangle = \langle (p_x - \langle p_x \rangle)^2 \rangle$, and $\langle xp_x \rangle = \langle (x - \langle x \rangle)(p_x - \langle p_x \rangle) \rangle$. The

emittance is a measure for the area of the two-dimensional (x, p_x) projection of the full six-dimensional phase space distribution $f(\vec{r}, \vec{p})$, which is independent of the beam energy or current. Here it is clear that for high brightness beams at a given current, a small emittance must be obtained. The emittance is a measure for the focusability of a beam; for a given focusing angle, the smaller the emittance, the smaller the spot size at the focus. Because the act of chopping the beam reduces the current by approximately 3 orders of magnitude, to compare the chopped beam with the DC beam entering the cavity, the emittances of the two should be employed, rather than the brightness.

The bunch will have a length $d_{elec} = v_z \tau \ll v_z \pi / \omega$. This will lead to a difference in entrance phases between the front and back of the bunch of $\Delta\phi = \omega\tau$, leading to a spread in momentum and position. This shall be quantified in the rms normalized transverse emittance, given in Eq. (5.4) [2].

The normalized emittance, defined in Eq. (5.4), is a measure of how laminar a group of electrons propagates through space [3]; alternatively, it can be viewed as how well collimated the electron beam is, and how tight of a focus the beam is capable of creating. Simple observation of Eq. (5.4) shows that the smaller the emittance, the better the beam; in that with smaller emittance, the beam behaves with closer agreement with the paraxial ray approximation. The treatment of Eq. (5.4) is described in detail in Appendix A for the case of a perfectly collimated uniform bunch of radius R , with the cavity fields at the phase ϕ when the bunch is at the center of the cavity. Solving for the final emittance gained after a bunch of temporal length τ has traversed the cavity simplifies to

$$\varepsilon_{n,x,col} = \frac{B_0 q R v_z \tau}{2\sqrt{3}mc} |\cos\phi|. \quad 5.5$$

Equation (5.5) clearly demonstrates that the emittance growth arises from the finite size of the bunch, both in transverse directions (R) as well as in the longitudinal direction (τ). The cosine dependence upon the entrance phase is disheartening as the general operation of the streak cavity requires chopping out sections of the beam near the zero phase, leading to a maximal emittance growth.

The question of minimizing this growth is the next logical step. What happens when the ideal bunch of electrons is focused, as illustrated in Fig. 5.2? A cross term $\langle xp_x \rangle$ arises in Eq. (5.4) when the radius R is substituted with $R(t_x - t)/(t_x - t_0)$, where t_x is the time that the center of the bunch is at the focal point and t_0 is the point before the cavity that the radius R is

measured, seen in Fig. 5.2. The full treatment in Appendix A.2 yields an approximation for the emittance growth,

$$\varepsilon_{n,foc} = \frac{B_0 q R v_z \tau}{2\sqrt{3}mc} |\cos \varphi| \left(\sqrt{\frac{(\pi + 2t_x \omega)^2}{(t_x - t_0)^2 16\omega^2}} + \sqrt{\frac{((\pi - 2t_x \omega) - 4 \tan \varphi)^2}{(t_x - t_0)^2 16\omega^2}} \right). \quad 5.6$$

Equation (5.6) clearly shows that the phase dependence becomes more complex, with additional dependence upon the focal point gained. It may be interesting to comment that the emittance in the focused case is equal to the collimated case multiplied by an extra term that is dependent upon the focal point. By taking the derivative and solving for t_x , it is found that a minimum occurs as $t_x \rightarrow \frac{-\tan(\varphi)}{\omega}$. This implies that a minimal emittance growth can be achieved for any phase, by appropriately choosing a correct focal point of the beam, with respect to the cavity. As was already specified, the cavity is centered around $t=0$. This implies, according to Eq. (5.6), that for the zero phase, emittance growth can be minimized by focusing in the center of the cavity.

5.1.3 Energy Spread

Thus far, the transverse beam degradation from the cavity has been explored. Next, the longitudinal properties shall be examined. To calculate the properties of the beam in the longitudinal direction, the Maxwell-Faraday equation, $\nabla \times E = -\frac{\partial B}{\partial t}$, is employed upon Eq. (5.1) yielding

$$E_z = B_0 \omega x \cos(\omega t + \varphi). \quad 5.7$$

Calculating the statistical rms momentum change in σ_{pz} , yields the rms energy spread $\sigma_U = \sigma_{pz} v_z$ for the collimated case; using the same substitution for the finite radial bunch size as was used in the emittance yields the focused situation, Eq. (5.8) and (5.9) respectively. The cases are treated thoroughly in Appendix C.

$$\sigma_{U,col} = B_0 R v_z |\cos \varphi|, \quad 5.8$$

$$\sigma_{U,foc} = B_0 R v_z |\cos \varphi| \sqrt{\left(\frac{t_x}{t_x - t_0} + \frac{\tan \varphi}{\omega(t_x - t_0)} \right)^2}. \quad 5.9$$

It is clear from Eq. (5.8) and (5.9) that the energy spread has the same behavior as the emittance, decreasing as the focus is brought to the center of the cavity. Analysis of Eq. (5.5), (5.6) and (5.8), (5.9) clearly show that for ideal operation of the cavity, chopping out bunches near the zero phase requires focusing in the cavity. Because small angle approximations were taken, it is expected that as the initial beam conditions worsen, the beam quality will deviate further from the analytical model; the opposite also is expected, the closer to an ideal beam one has, the more accurate the model will perform.

Often in electron microscopy, rather than discussing the beam in terms of a focal point, the convergence angle is used. It was assumed in the model that the velocity in the z direction is constant through the cavity, which allows the substitution $z=v_z t$. In the small angle regime $(t_x-t_0)v_z \gg R$, it is found that the convergence angle is $\alpha \approx R/(v_z(t_x-t_0))$, which can be extrapolated from Fig. 5.2. In both Eq. (5.6) and (5.9) there is a dependence upon $R/(t_x-t_0)$. Replacing $R/(t_x-t_0)$ with αv_z will give the dependence upon the convergence angle of the beam.

5.2 GPT

In this section, the analytical model will be compared to numerical simulations in General Particle Tracer (GPT) [4] under the same conditions given in Sec. 5.1. The numerical simulations utilize the realistic cavity fields including fringe fields, designed in CST studio suite [5]. The realistic cavity modeled is the same as the one that has been commissioned, built, and implemented in an augmented 30 keV electron microscope beam line [1]; the cavity is described in Ch. 3 and the technical drawings can be found in Appendix A.5, while the beam line is given in Ch. 4.

5.2.1 Fields, Momentum, and Position

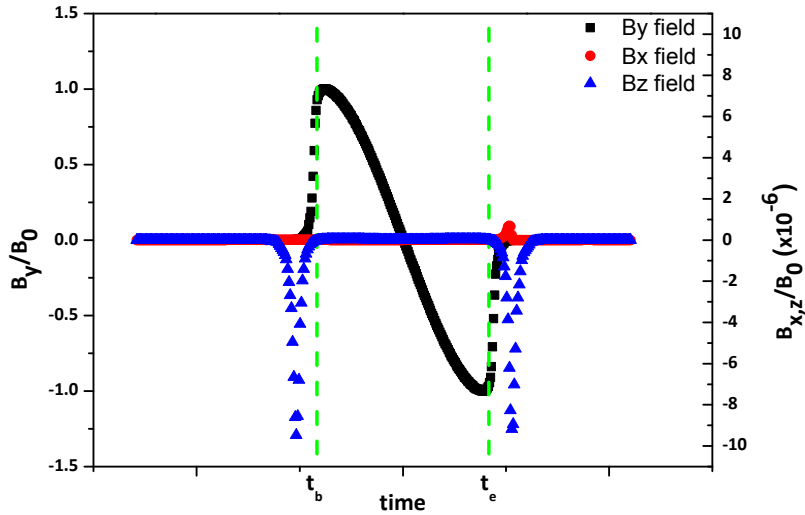


Figure 5.5: The realistic magnetic fields of the TM_{110} cavity seen by an electron bunch traversing the cavity; the cavity walls are indicated by the dotted green lines. As seen in the black squares, the B_y field dominates, while the B_x and B_z fields are 6 orders of magnitude lower in amplitude compared to B_y .

The realistic cavity magnetic fields are seen above; the B_y field dominates the magnetic field along the longitudinal axis. The phase chosen for this particular figure was the zero phase, $\varphi=0$. Because the B_y field is symmetric around $t=0$, the integration of the transverse force from this field will result in it being zero, and thus, zero transverse momentum gain. The fringe fields, B_x and B_z are negligible, since they are five orders of magnitude lower than the B_y field. It can be noted that these fringe fields occur outside of the cavity, completely in the entrance/exit holes for the electrons to traverse, as can be seen in Fig. 5.5, since the fields sit outside of the green dashed lines denoting the beginning and end of the cavity.

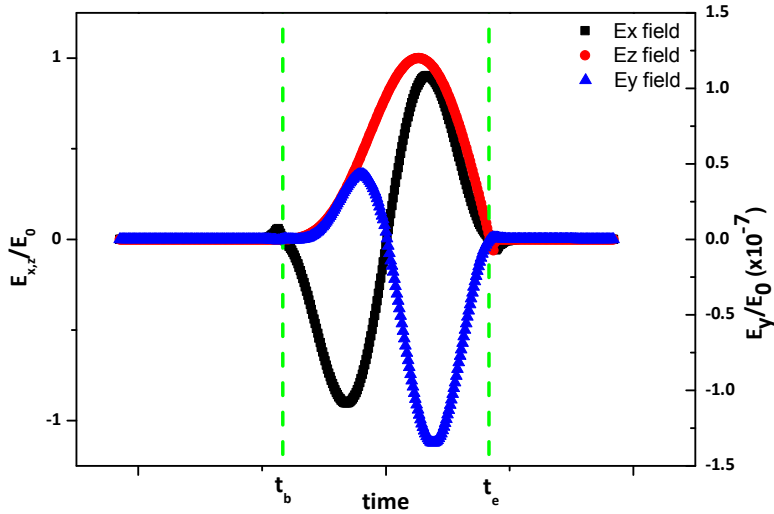


Figure 5.6: Electric Fields of the TM_{110} cavity seen by a traversing electron bunch. The red circles are the E_z field while the black squares and blue triangles are the fringe fields added due to the geometry of the cavity. It is clear that there is a large fringe field in the x-direction, while the fringe field in y is negligible.

Figure 5.6 clearly shows that there is a large electric fringe field in the x-direction that is modeled in CST and used in the GPT simulations, but neglected in the analytical model. This fringe field arises due to the hole drilled through the cavity and dielectric so that the electrons are capable of traversing the cavity. It is this extra fringe field that was mentioned briefly in Sec. 3.3.2, creating errors in the field profile measurement seen in Fig. 3.7. The contributions to emittance and energy spread from the realistic cavity with fringe fields will be compared to the analytical model in Sec. 5.2.2 and 5.2.3. It is also important to note that the fields are asymmetric because Fig. 5.6 is the electric field “seen” by a passing electron bunch which is dependent upon the x position of the bunch. Figure 5.4 demonstrates that the x position changes as the bunch crosses the cavity.

Consider a 100 fs bunch of electrons with an initial emittance and energy spread of zero. The bunch has an initial radius of $R_0=10\ \mu\text{m}$ with the cavity centered at the position $z_{cav}=0.1\ \text{m}$ with a magnetic field amplitude along the longitudinal axis of $B_0=2\ \text{mT}$.

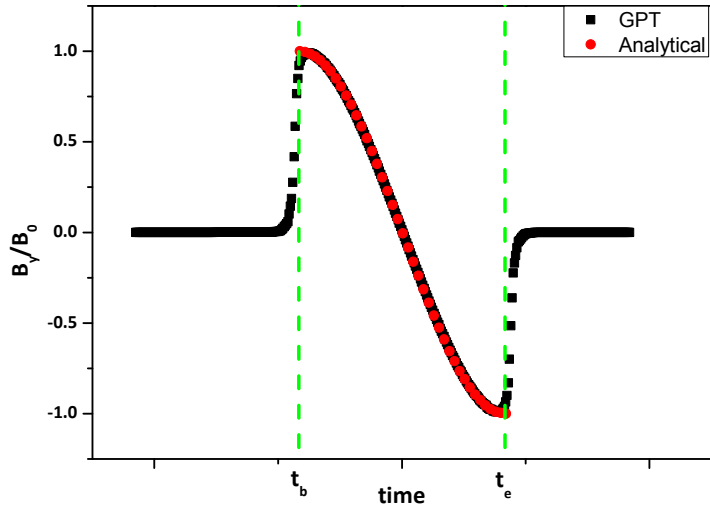


Figure 5.7: Magnetic field B_y , normalized by $B_0=2$ mT. The red circles represent the analytical model, and black squares represent the model used in GPT.

Figure 5.7 is a comparison between the magnetic field felt by the electrons in the analytical model (red) and the GPT simulations (black). In the analytical model, the field is zero outside of the cavity, while the realistic fields from CST and used in GPT are not a perfect step function.

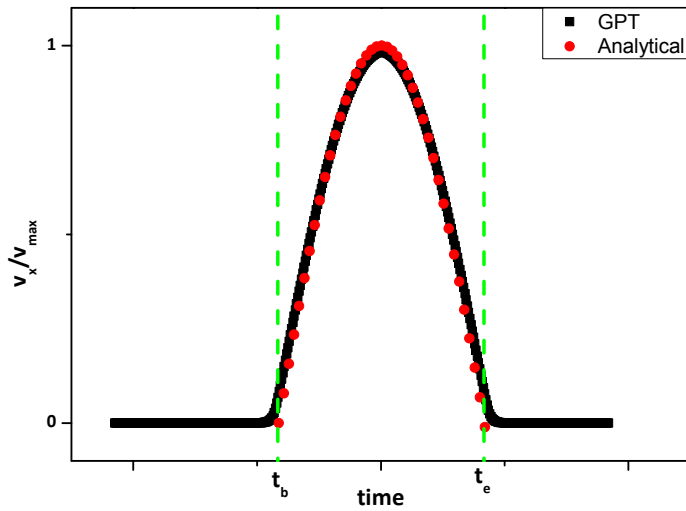


Figure 5.8: Velocity in the x-direction as a result of the magnetic field with amplitude $B_0=2$ mT.

Figure 5.8 shows a slight discrepancy between the analytical model and the numerical simulations for the transverse velocity gained/lost through the cavity. As shown in Fig. 5.7, the fields extend out beyond the length of the cavity due to holes. This, results in slightly different fields felt by the electrons between the analytical model and GPT, which explains why the velocity curves have the same shape but have different amplitudes.

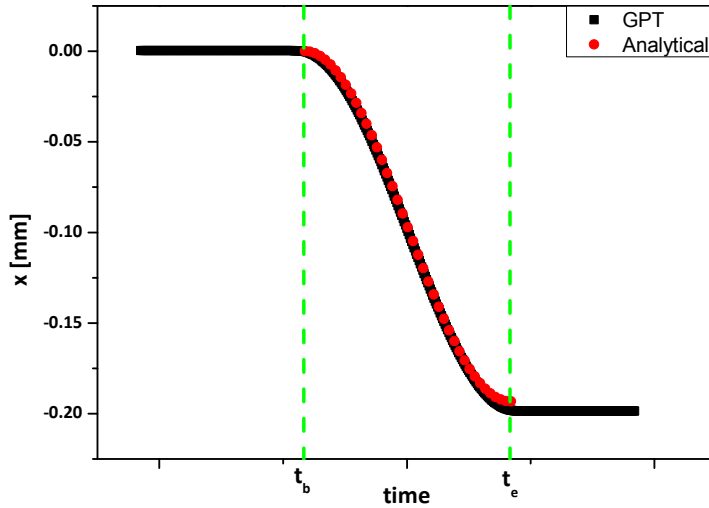


Figure 5.9: X-position, x , of the electron as a result of traversing the cavity with a field amplitude of $B_0=2$ mT and entrance phase $\varphi=0$. In the zero-momentum phase, an offset proportional to the magnetic field amplitude B_0 is seen in both the analytical model (red dots) and the numerical simulations (black squares).

As can be seen in Figs. 5.7, 5.8 and 5.9, the analytical model closely agrees with numerical simulations for the behavior of an electron bunch traversing the cavity. The transverse position and momentum of the bunch are accurately described and known. These calculations do not take into account the focusing of the beam, as it is not necessary since these calculations assumed an electron on the $r=0$ axis. The energy spread and normalized transverse emittance, however, do. First we shall examine the collimated case.

5.2.2 Collimated Case

The emittance and energy spread are calculated using Eq. (5.5) and Eq. (5.8) for a collimated (see Fig. 5.2) bunch traversing the TM_{110} cavity, and compared to GPT simulations.

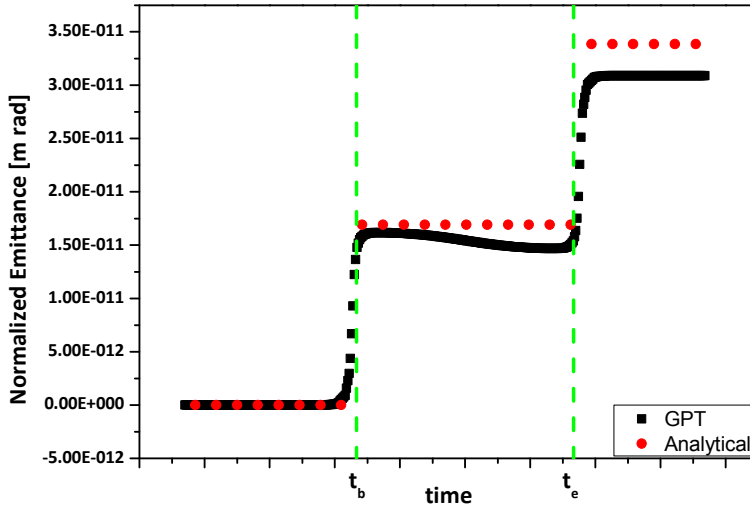


Figure 5.10: Normalized transverse emittance growth in the x-direction of the collimated beam for a field amplitude of $B_0=2$ mT and entrance phase $\varphi=0$. The behavior of growth at the beginning and end of the cavity is seen for the zero phase case. Through the cavity, the emittance appears to lower in the GPT simulations. This is not the case, as it is a correlated system passing the growth on in another dimension; this figure only shows the x-dimension.

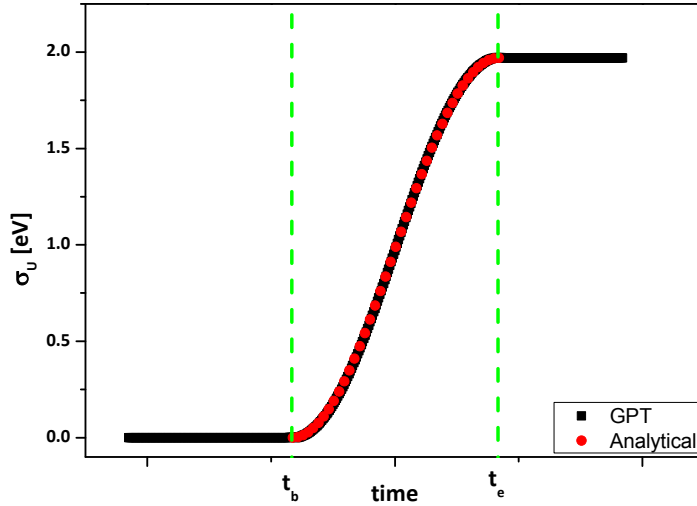


Figure 5.11: Standard deviation of the energy spread of the beam when the cavity has an amplitude of $B_0=2$ mT and entrance phase $\varphi=0$. The analytical model (red circles) matches the numerical simulations (black squares).

As can be seen in Figs. 5.10 and 5.11, for this particular phase ($\varphi=0$), the transverse emittance and energy spread analytical models match well with the numerical simulations in behavior and to a lesser extent quantity. The emittance does not fit as well with the simulations due to the fact that the simulations take into account all the fringe fields which obviously play a role in the emittance in the x -direction. It is important to note that the emittance growth occurs at the entrance and exit of the cavity, while the energy spread growth occurs during the cavity transit time. To check the accuracy of the analytical model, it is helpful to check the final emittance and final energy spread as a function of phase.

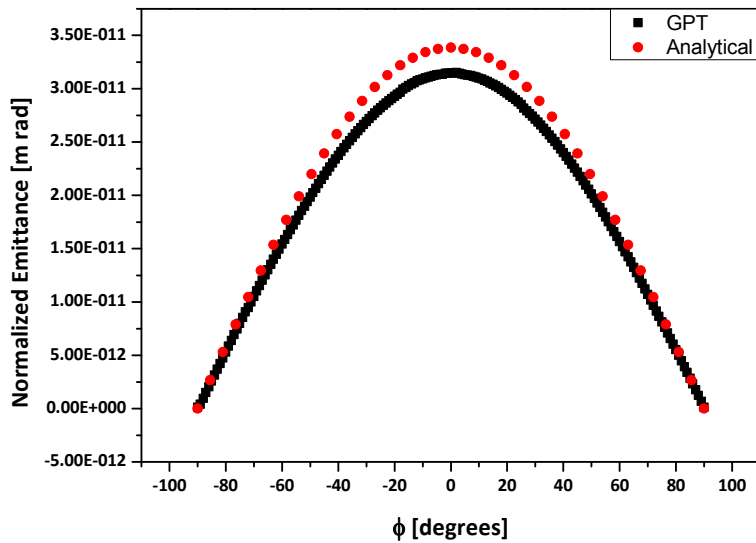


Figure 5.12: Normalized transverse emittance of a collimated bunch traversing the cavity with a field amplitude of $B_0=2$ mT versus the entrance phase ϕ of the cavity.

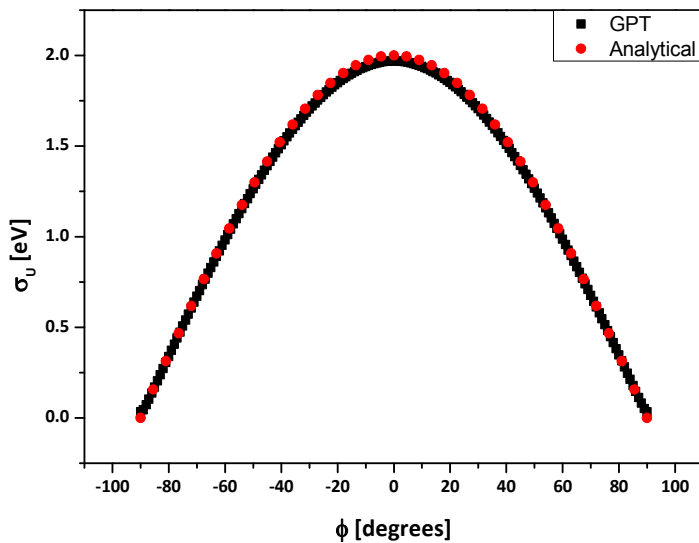


Figure 5.13: Energy spread versus the entrance phase ϕ of the cavity, comparing the analytical model (red dots) with the numerical simulations (black squares). The cavity has a field amplitude of 2 mT.

As Fig. 5.12 and Fig. 5.13 show for the collimated case, the largest growth in both transverse emittance and energy spread is obtained for the $\varphi=0$ phase, while the smallest growth occurs a quarter of a period later, as Eq. (5.5) and (5.8) predicted. In the transverse emittance case, a discrepancy can be seen between the analytical model and the simulations. This is most likely caused by the extra E_x field contribution which is in the simulations but not taken into account in the analytical model. The energy spread growth accurately agrees in amplitude for the analytical model and simulations because of a lack of fringe fields that would cause an effect in the z-direction.

5.2.3 Focused Case

The collimated case has been examined for the emittance growth and energy spread, and the analytical model successfully matches the numerical simulations of the realistic condition. Let us now turn our attention to the focused case, seen in Fig. 5.2.

Figure 5.14 considers the transverse emittance gained as a function of the focal point of the beam (with respect to the cavity, centered at $z=0$ m) and the entrance phase of the cavity. As seen in Fig. 5.14, the normalized transverse emittance reaches a minimum at the phase $\varphi=0$ when the electron beam is focused near the center of the cavity. Accurate agreement covers the full phase spectrum, with small deviations arising as a result of the electric fields.

Figure 5.15 demonstrates how the energy spread has the same behavior as the normalized transverse emittance. A minimal energy spread occurs at the same point as the minimal emittance growth; when the electron beam is focused in the cavity.

It is important to note that the analytical model describes both the behavior and amplitude of the growth in energy spread and emittance for both the collimated and focused case. Also, the deviations in the model from GPT in the emittance can be attributed to fringe fields in the x-direction. Figures 5.14 and 5.15 also show that for any given phase, there is an ideal focal point to minimize the growth in emittance and energy spread.

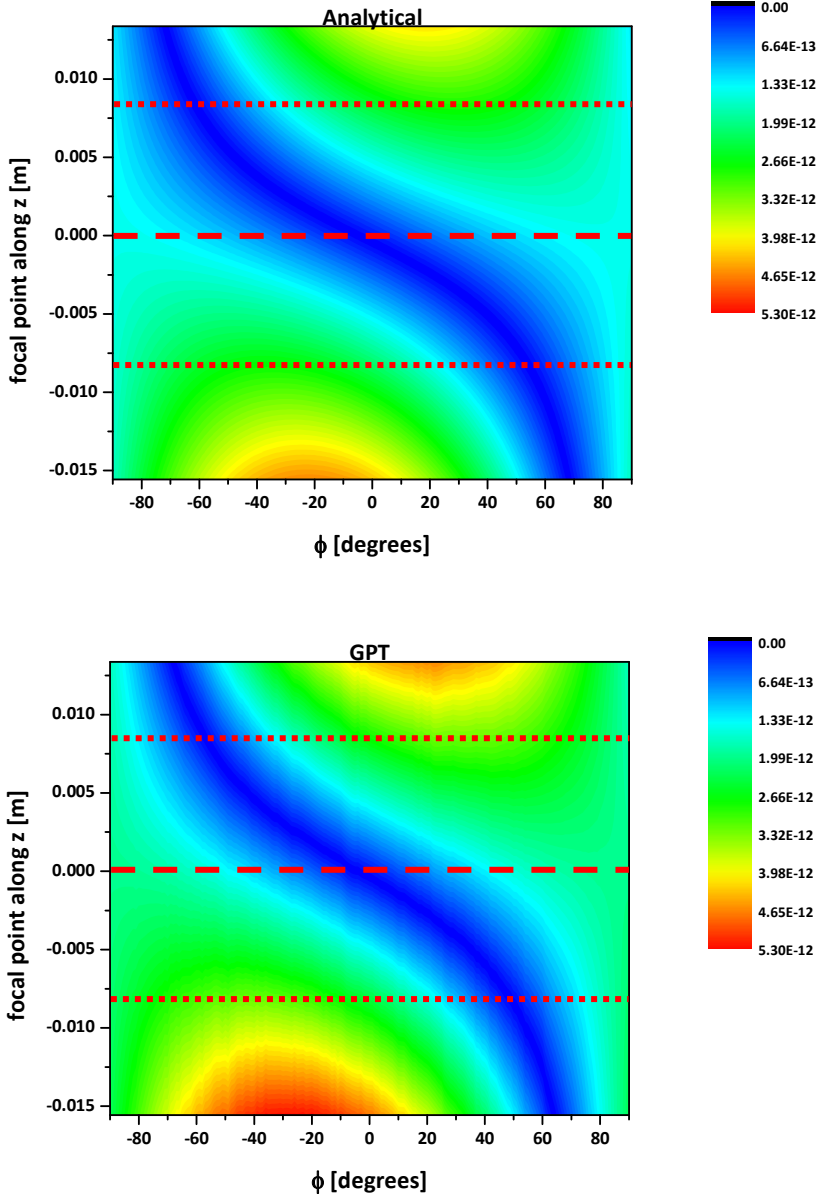


Figure 5.14: Contour plot of the transverse normalized emittance growth in [m rad] as a function of the focal point along the z-axis and the entrance phase of the cavity, with blue being small and red large. The cavity is placed at $z=0$ m and a field amplitude of $B_0=2$ mT, with the same initial beam conditions as the previous section. The dashed red line denotes the center of the cavity, while the dotted red lines denote the beginning and end of the cavity.

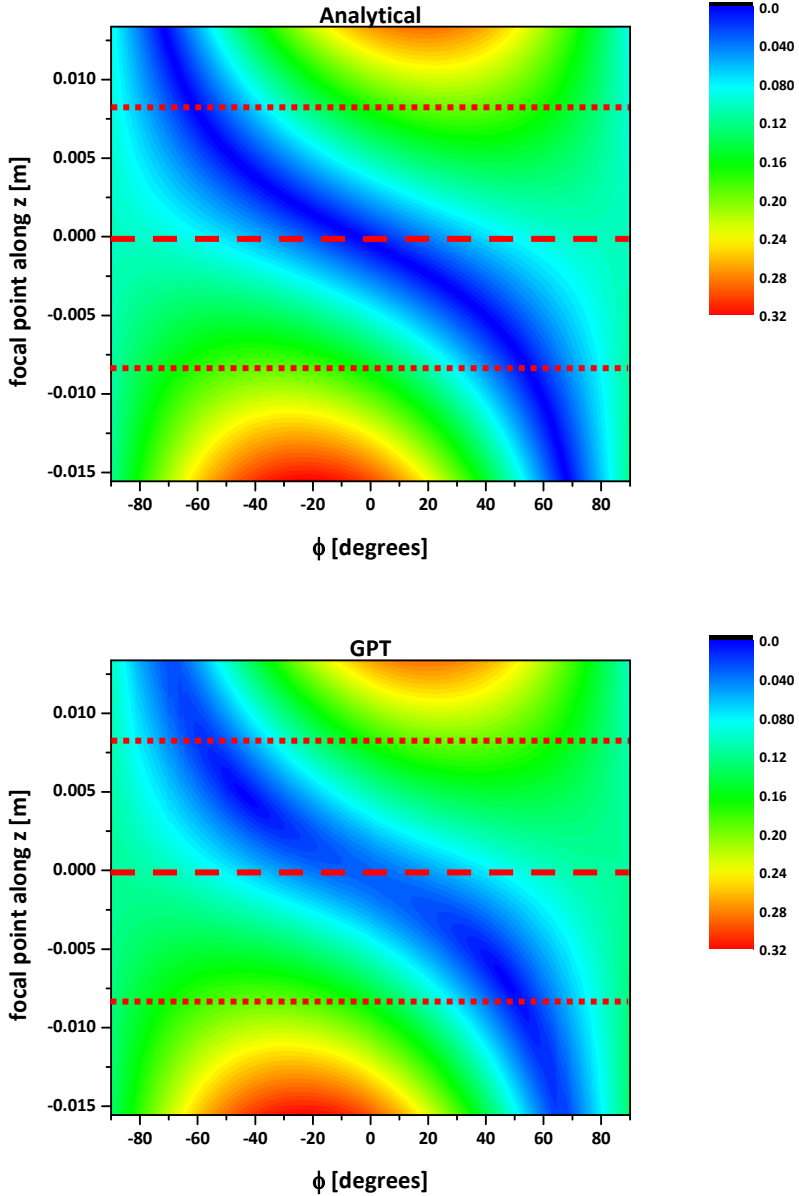


Figure 5.15: Contour plot of the energy spread growth σ_v in [eV] as a function of the focal point along the z-axis and the entrance phase of the bunch into the cavity, small values represented in blue, large in red. The cavity is placed at $z=0$ m with an amplitude of $B_0=2$ mT. The dashed red line denotes the center of the cavity, while the dotted red lines denote the beginning and end of the cavity.

5.2.4 Phase Space

At this point, it may be helpful to visualize what is going on with the bunch in the cavity. For this, we look at the x - p_x phase space distribution and how it changes as the bunch traverses the cavity for both the collimated and focused case. Because the emittance is directly proportional to the area encapsulated by the x - p_x distribution, observing the behavior in x - p_x phase space can be helpful in understanding the dynamics behind the emittance growth.

Figure 5.16 shows the x - p_x phase space distribution for the collimated and focused beams, left and right respectively. The area enclosed by the bunch in the phase space plots corresponds to the transverse emittance. As the bunch enters the cavity, the front of the bunch (colored in red) is given a greater momentum kick than that of the back of the bunch (colored in blue), resulting in the correlation between x - p_x and z . As the bunch is leaving the cavity, the back of the bunch receives an opposite momentum kick from that of the front of the cavity. This results in a doubling of the emittance for the collimated beam. However, as can be seen for the focused bunch, the focusing reverses the correlation between z and x - p_x . As the focused bunch is leaving the cavity, the negative kick in p_x upon the backside of the bunch reverses the kick received upon entering the cavity, collapsing the distribution back to a line. It should also be important to note that after the cavity, in both the collimated and focused case, the front and back of the bunch are offset in x which is a clear indicator of a slanted wave front, which is expected since the linear section of a sinusoidal curve is chopped out.

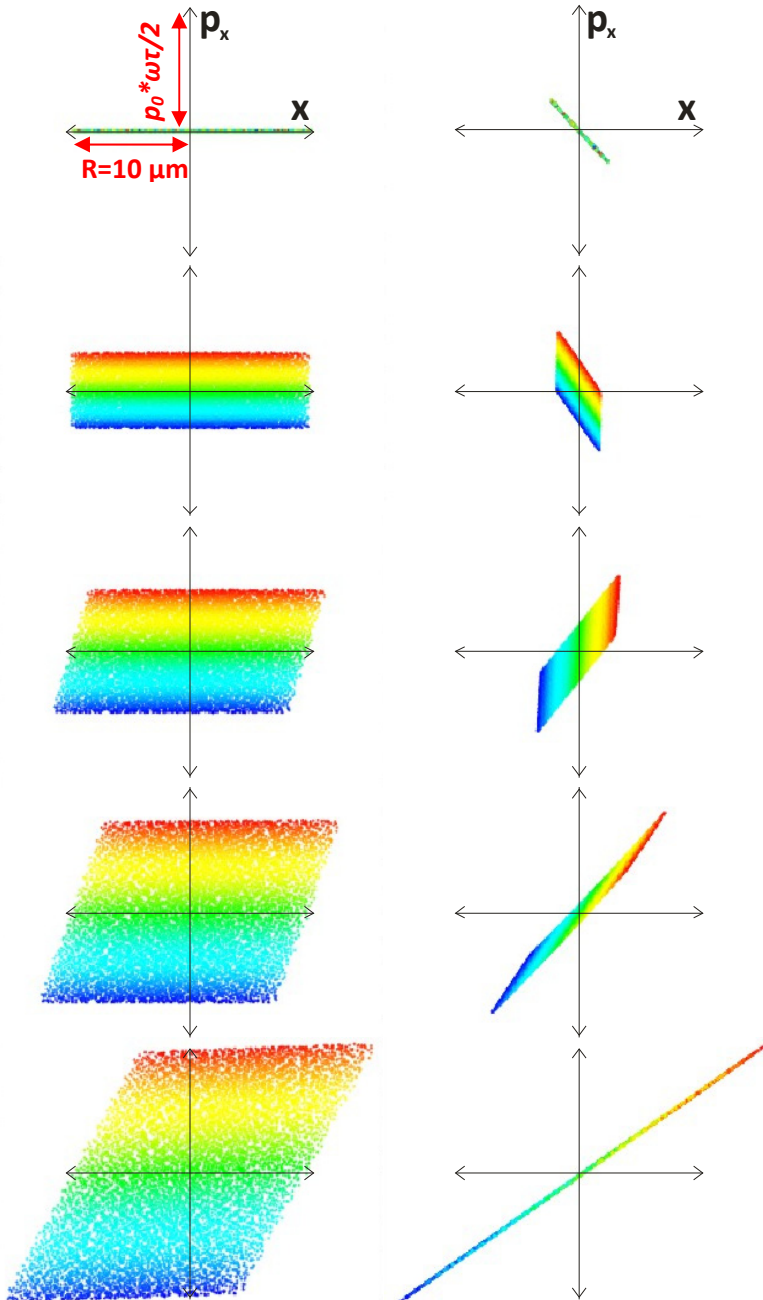


Figure 5.16: The x - p_x distribution colored in z with respect to the center of the bunch (red=front, blue=back), as a bunch crosses the cavity in the zero phase (pictures from top to bottom: $t < t_b$, $t = t_b$, $t_b < t < t_e$, $t = t_e$, $t_e < t$). The collimated bunch is considered on the left, while the focused bunch is on the right. A clear correlation between z -position in the bunch and the phase space can be seen.

The mechanism through which the emittance growth occurs through the cavity and how it is minimized has been explained analytically as well as numerically with the aid of phase space distributions. However, the model and GPT were run with zero initial emittance and zero initial energy spread: a perfect beam. This differs greatly from realistic situations. Realistic beams have initial emittance, which limits how tight the beam can be focused for a given angle, increasing the emittance growth. Despite this, one main generalized statement can be made about the cavity based on both the analytical model and simulations: smaller angles and beam sizes before entering the cavity will lead to lower beam quality degradation after the cavity, i.e. the better the beam, the better the cavity works.

A second, perhaps more important realization for implementation into a microscope or beam line is that focusing in the cavity reduces the emittance and energy spread growth. Also, if a slightly different phase-section of the beam wishes to be used, it is possible to calculate an ideal focal point to maximize the final beam quality. For example, if a slit is placed 0.1 meters behind the cavity on the longitudinal axis ($x=y=0$), the x-offset due to the cavity will require that a phase of approximately $\varphi=4^\circ$ (or 0.06981 radians) will be cut out of the streaked beam, rather than the phase $\varphi=0$.

5.3 *Emittance Measurements*

The cavity is placed inside a 30 keV altered scanning electron microscope table top beam line. The cavity was designed to be compact and small enough to be placed inside the microscope, but for the purpose of this research, the cavity is placed outside the microscope, a distance of $z_{cav}=0.47$ m beyond the last lens of the SEM. A 100 μm slit is placed a distance of 85 mm behind the cavity.

Figure 5.9 predicts an offset for the $\varphi=0$ case. But careful examination shows that a slit on the longitudinal axis will not chop the $\varphi=0$ section of the streaked DC beam, but instead the $\varphi=0.06981$ rad section. Half a period later, rather than the $\varphi=\pi$ phase, the $\varphi=\pi+0.06981$ phase will be chopped. This results in a non-zero transverse momentum for the electron bunches, alternating in sign between any two consecutive bunches. At large field amplitudes B_0 and short cavity-slit distances, bunches passing the slit become separated by their alternating transverse momentums. This results in two separate spots seen on the detector, separated in the direction of the streak, as schematically depicted below and seen experimentally in Fig. 5.18.

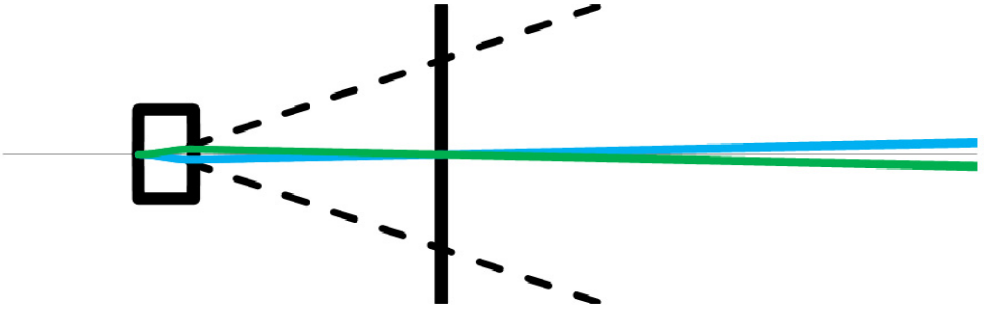


Figure 5.17: Cavity and slit schematically representing the operational use. The green line represents the phase of the DC beam that passes the slit, while the blue line represents the same with a π phase shift. It is clear to see the separation of the bunches on the detector.

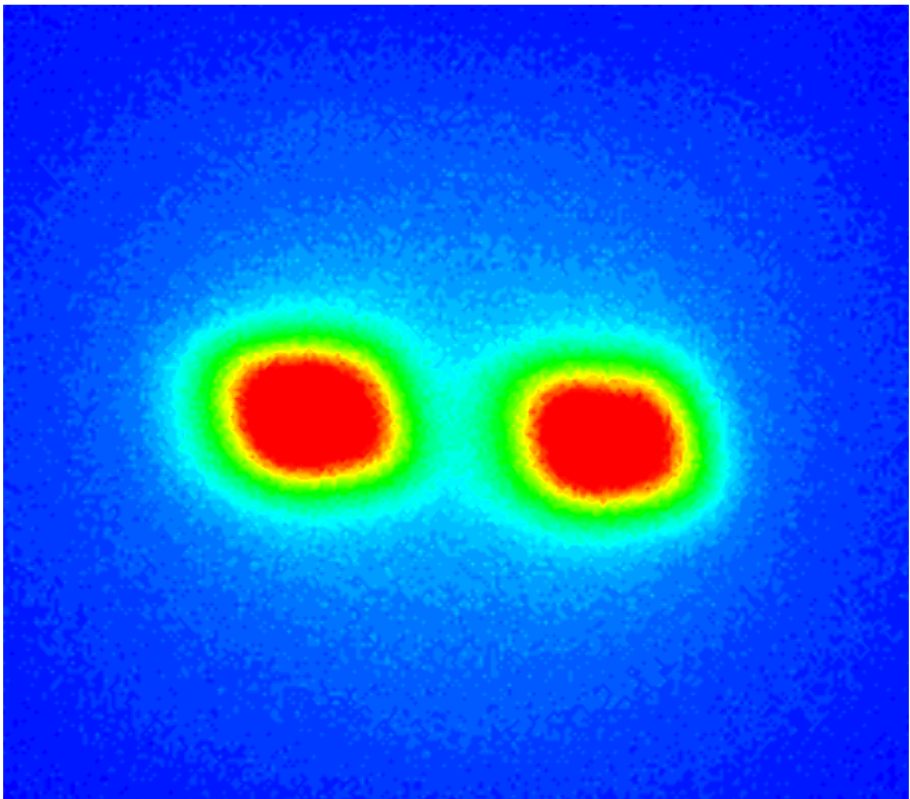


Figure 5.18: Two spots observed on the detector as a result of non-zero transverse momentum.

Figure 5.18 shows the behavior of the non-zero transverse momentum for the two beams as a result of the offset gained in the cavity. This agrees with both the analytical model and GPT, as schematically shown in Fig. 5.17.

To measure the emittance, the beam line was extended, adding a quadrupole focusing magnet between the slit and detector. A waist scan was performed upon the electron beam, varying the focal distance of the quadrupole and measuring the spot size on the detector. To first order approximation, the beam will have an RMS size σ_x on the detector given by

$$\sigma_x = \sqrt{\left[l_1 l_2 - (l_1 + l_2) f_{quad}\right]^2 \frac{\varepsilon_{N,x}^2}{\gamma^2 \beta^2 \sigma_v^2 f_{quad}^2} + (f_{quad} - l_2)^2 \frac{\sigma_v^2}{f_{quad}^2}}, \quad 5.10$$

where l_1 is the distance from the (virtual) source to the quadrupole magnet, l_2 is the distance from the quadrupole magnet to the detector, f_{quad} is the focal length of the quadrupole, σ_v is the virtual source RMS size, $\varepsilon_{N,x}$ is the normalized transverse emittance, $\beta = v_z/c$ is the normalized velocity, and $\gamma = (1 - \beta^2)^{-1/2}$ is the relativistic lorentz factor [6], as seen below in Fig. 5.19.

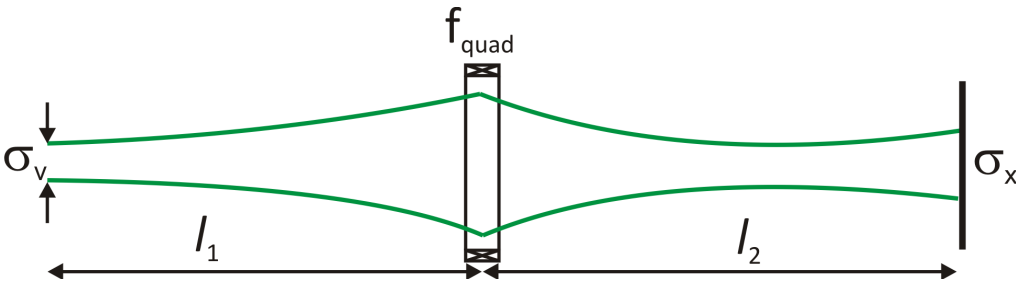


Figure 5.19: General Principle of the quadrupole waist scan.

The equation assumes the magnet to act like a thin lens, and that the beam behaves as if it had originated from a virtual source of size σ_v located a distance l_1 before the magnet. The values l_1 and l_2 are known, so plotting σ_x as a function of f_{quad} , leaving σ_v and $\varepsilon_{N,x}$ the variables to be fit. Within these parameters, σ_v is constrained to grow larger as the focal point is placed further away from the SEM and to have a reasonable value ($<750 \mu\text{m}$, usually close to $400 \mu\text{m}$). These measurements were applied to the normal DC beam, and again to the chopped beam, as seen in Fig. 5.20.

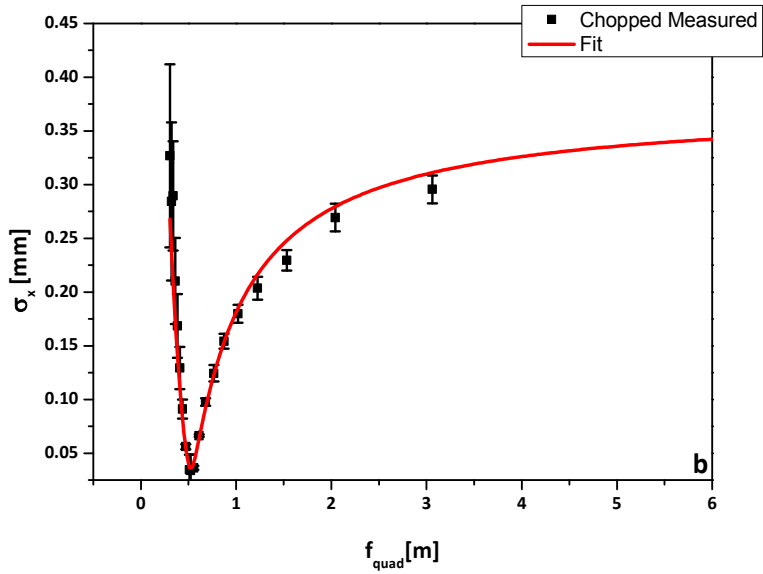
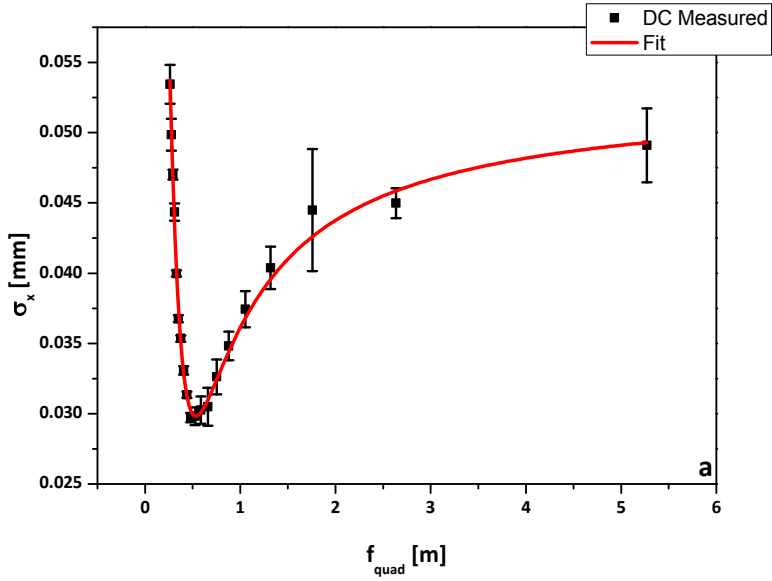


Figure 5.20: Quadrupole waist scan measurements to determine transverse emittance of a) DC beam, b) chopped beam. Black squares are measurements, with the red solid line representing a fit of Eq. (5.10).

The waist scan of the DC beam yielded a transverse emittance of $\epsilon_{N,x}^{dc} = (9 \pm 1) \times 10^{-10}$ m rad at a current of $I = 100$ nA corresponding to a brightness $B_r \approx 4 \times 10^4$ A/m² sr eV, a very standard

value for an older tungsten hairpin emitter system. The corresponding emittance with the cavity turned on and the slit moved into place was $\epsilon_{N,x}^{strk}=(9\pm 0.5)\times 10^{-9}$ m rad. This is an increase by an order of magnitude but still yields a beam quality comparable to or perhaps better than photo-cathode driven systems.

The model predicts that focusing the beam at the cavity will reduce the emittance growth, while focusing further away from the cavity will cause growth. This regime was tested in experiments and plotted against GPT simulations of the beam line. The initial emittance of the 30 keV SEM was measured to be $\epsilon_{0,x}=0.9$ nm rad. The focal point was placed beyond the cavity, and then moved closer and eventually through the cavity. A quadrupole waist scan was performed at each of the focal points to extract the final normalized transverse emittance in the direction of the streak, while the cavity was switched on and chopping occurred.

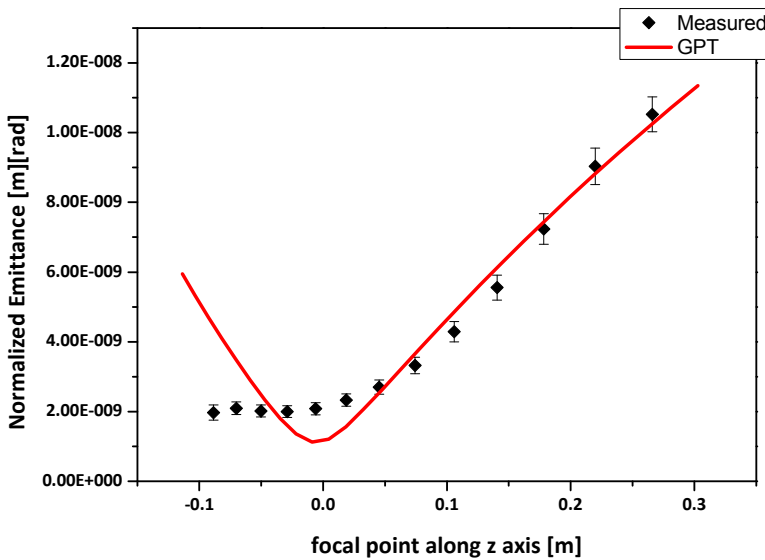


Figure 5.21: Normalized transverse emittance measurements at various z-focal points are represented by black diamonds while GPT simulations reproducing the beam line are shown in the red line.

Figure 5.21 clearly demonstrates the behavior predicted of reducing the transverse emittance by bringing the focus of the beam towards the cavity, located at $z_{cav}=0$ m in Fig. 5.21. However, it can be seen that the measurements do not follow the simulations at the point of focusing before the cavity. This is due to the fact that at those angles, the beam becomes aperture limited by the slit and the cavity entrance/exit, so a starting initial emittance of the aperture limited beam becomes lower, which was not taken into account in

Fig. 5.21. The model predicts that as a beam is focused towards infinity, it will behave more and more like the collimated case.

In the collimated case, the model predicts that the largest emittance growth will occur for the zero phase case, while the $\pi/2$ phase will give the smallest emittance growth. The beam was focused beyond the detector ($z=2$ m) and the cavity switched on; the slit was moved down to different positions, sampling different phases of the full streak, seen on the bottom of Fig. 5.22. The $\pm 90^\circ$ in Fig. 5.22 corresponds to the section of the beam that is streaked the strongest, i.e. maximum deflection.

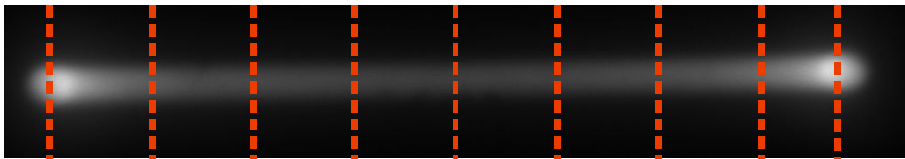
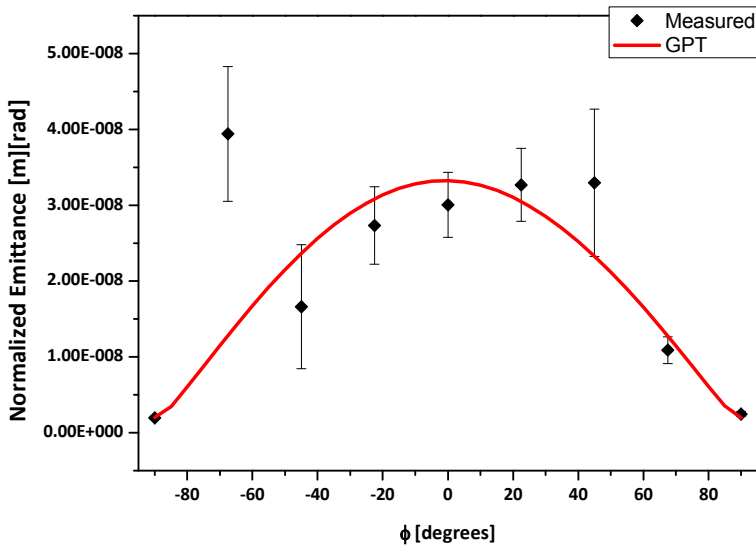


Figure 5.22: Black squares show the measured emittance values while the red solid line shows the predicted behavior in GPT. On the bottom, the red dotted lines show where the slit was placed with respect to the streak.

Figure 5.22 clearly shows that for the collimated case, the largest emittance growth occurs near the zero phase case, demonstrating the phase dependent behavior predicted by the model. The outlying point can be attributed to an instability that arose with the W-hairpin emitter in the SEM, as measurements were taken with a relatively new tip, susceptible to contamination and microscopic imperfections.

5.4 Conclusions

The analytical model has demonstrated to be a powerful tool to predict the beam properties of electrons traversing the cavity. The trajectories were predicted with both the analytical model and numerical simulations, and demonstrated experimentally with dual spots seen after chopping.

Figures 5.21 and 5.22 have demonstrated the emittance growth behavior that the model predicts: emittance growth as a function of the focal point and as a function of phase, respectively. In part to describing the behavior by means of the analytical model, numerical simulations have accurately matched measurements in behavior and amplitude.

On top of predicting the behavior of the beam, the analytical model demonstrates that there is an ideal focal point for any given phase chosen to be chopped out to maintain the emittance and energy spread of the beam. The model predicts the beam quality following the traversal of the TM_{110} cavity, adding insight into how and where the focus should be placed to operate the cavity with minimal beam quality degradation.

In order to be implemented into an existing microscope (Sec. 6.1) or to do experiments with a high temporal and spatial resolution (Sec. 6.4, and Sec. 7.3), the beam quality must be maintained, or at the very least have the degradation minimized. The model and simulations have given insight on how to do this, and where the degradation comes from: in the form of transverse emittance, this is caused by the longitudinal length of the bunch being chopped as well as the radial size of the bunch and the focal position; the energy spread comes purely from the radial size of the bunch. This implies that for higher quality beams, the less the degradation to beam quality.

Because the analytical model for both the emittance and energy spread were derived assuming ideal beam conditions (zero initial emittance beams) as well as linear fields, it is clear that as the initial emittance grows, the beam will no longer follow ideal conditions, giving rise to higher order effects that will contribute to the growth in emittance and energy spread. For this reason, the better the initial conditions of the beam, the more accurately the analytical model will predict the emittance and energy spread growth. As the field amplitudes increase, it is clear from Eq. (5.3) that the electrons will go further off axis and the linear field approximation will no longer hold, making the analytical model less accurate.

References

- [1] Lassise, A., P.H.A. Mutsaers and O.J. Luiten. "Compact, lowpower radio frequency cavity for femtosecond electron microscopy." *Review of Scientific Instruments* 83 (2012): 043705.
- [2] Luiten, O.J., et al. "Ultracold Electron Sources." *International Journal of Modern Physics A* 22.22 (2007): 3882-3897.
- [3] Humphries, Stanley. *Charged Particle Beams*. Albuquerque: John Wiley and Sons, 2002.
- [4] Pulsar Physics. "General Particle Tracer (GPT) User Manual." n.d. *General Particle Tracer (GPT)*. <www.pulsar.nl>.
- [5] Computer Simulation Technology. "CST Microwave Studio 2011 User Manual." n.d. *CST Microwave Studio 2011*. <www.cst.com>.
- [6] Stragier, X. *Towards external injection in laser wakefield acceleration*. Eindhoven: TU Eindhoven, 2011. Thesis.

6 Applications and Valorization

To now, the description of a beam line designed and built to create femtosecond electron bunches using only RF technology has been presented. It has been shown through analytical models, simulations, and measurements that the TM_{110} cavity combined with proper focusing can create electron bunches with little degradation to the beam peak brightness. This allows for femtosecond electron microscopy studies to be carried out, without the mandatory use of femtosecond laser systems for beam generation.

In this chapter, future work in the scope of this project is presented, simulated, and discussed. First, simulations demonstrating implementation of the cavity into an existing electron microscope column done in full cooperation with FEI Company [1] is discussed. There are a number of technical aspects which must be overcome in order to bring the cavity to a marketable product. These are given with possible solutions in Sec. 6.1.1.

Section 6.2 discusses the possibility of using the split degenerate modes that were purposefully separated in Ch. 3. The proposal is supported with experimental observations, and works as follows: essentially streak the beam in two directions, rather than just one. If properly synchronized, the repetition rate of the electron bunches should be based on the beat frequency between the two resonant frequencies, dramatically lowering the repetition rate to something that is more easily synchronized to lasers or deflection plates.

Section 6.3 presents measurements supported by GPT simulations of two cavities operating simultaneously. The first cavity is the TM_{110} streak cavity, the second a TM_{010} compression cavity. The two cavities are driven with one oscillator, and precise phase control between the two cavities is demonstrated. This precise phase control is key to synchronization between multiple RF cavities.

With the phase control between multiple cavities synchronized to the same RF signal demonstrated and a possible way to synchronize with a laser for pump-probe experiments presented, a femtosecond electron energy loss spectroscopic (FEELS) pump-probe setup is designed using only two cavities, both TM_{110} cavities. The energy resolution of the setup is compared to that of Zewail's ultrafast electron microscope (UEM) [11] in which FEELS has been carried out [8, 10]. To take it one step further, the setup is simulated in the 30 keV beam line. To achieve an energy resolution of <1 eV, a third TM_{010} cavity is added.

Finally, to bring the RF cavities in electron microscopy full circle back to Scherzer, a TM_{010} cavity is simulated to work as a spherical aberration corrector. A highly divergent beam is sent through two solenoid lenses, followed by the TM_{010} cavity. It will be shown that as the

cavity's field amplitude is increased, the spherical aberration is corrected for and even overcorrected. This comes at a cost, however, due to the nature of the cavity which will be discussed further.

6.1 Implementation into an Existing Electron Microscope

This project is part of a larger project between the government funding agency FOM and the electron microscope company FEI. As part of the project, close contact was kept with FEI. As the TM_{110} cavity became operational and worked as expected, interest began to pique within the company as utilization of the cavity became a realistic possibility, particularly as the demand for ps and fs time resolution grows within the microscopy community. The cheap, simplistic, compact design and operation of the TM_{110} cavity is a feasible way to create fs electron bunches without the use of pulsed photoemission. This allows for the laser to be used for pump-probe experiments, but not a requirement for electron bunch generation.

A feasibility study was simulated in parallel at FEI and TU/e for implementation of a TM_{110} cavity into a 200 keV Tecnai Transmission Electron Microscope (TEM). A pillbox cavity was simulated and designed to run at 3 GHz for the 200 keV electrons. Initial beam conditions were given by the company, as well as sizes and dimensions. The schematic implementation can be seen in Fig. 6.1.

For 200 keV at 3 GHz, the length of the cavity should be $d=34.74$ mm, but is simulated as $d=34$ mm. This gives the cavity to slit distance as $l=33$ mm as the slit is fixed in the original Tecnai implementation design (see Fig. 6.1). To have a temporal resolution of $\tau=100$ fs Eq. (2.2) dictates a magnetic field amplitude of $B_0=12.9$ mT; a field of 12 mT gives 110 fs and was used in simulations.

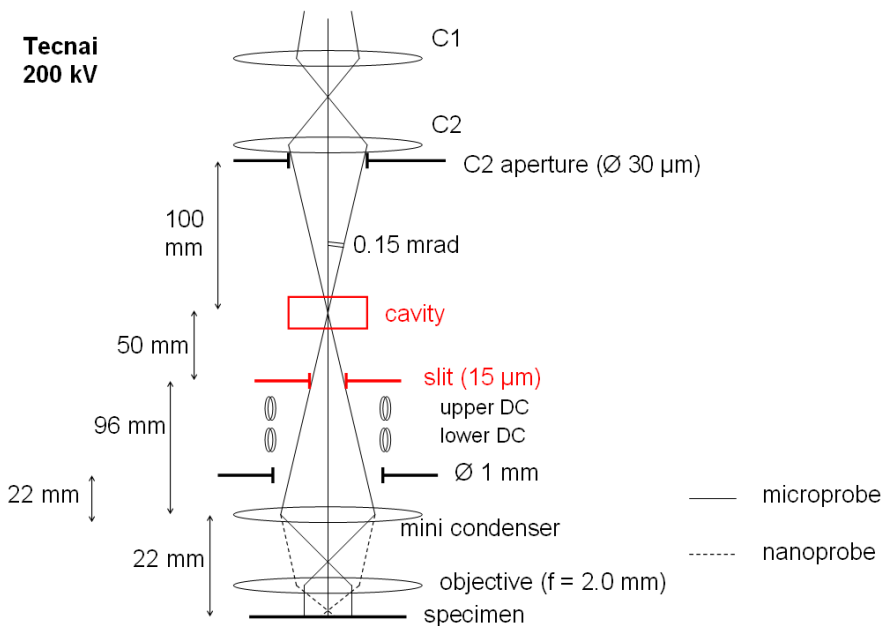


Figure 6.1: Schematic diagram showing the placement and lengths for implementation of a TM_{110} cavity into a 200 keV Tecnai TEM. The red represents the cavity and slit to be implemented. C1 and C2 are condensers, upper and lower DC are DC correction coils. The micro- and nanoprobe are two operation modes of the microscope.

It is important to note the location of the cavity. The cavity is placed between the C2 aperture and the slit such that focusing in the middle of the cavity (as revealed necessary in Sec. 5.2.3) when the cavity is switched off will still allow the full beam to pass through both the aperture and slit. The slit size is chosen as 15 µm because of the size of the C2 aperture and practical difficulties with slits and apertures below 15 µm. If the slit is placed on the optical axis, then the upper and lower DC coils are necessary to correct the transverse momentum gained in each bunch discussed in Ch. 5. As a technical note, it may be advantageous to place the slit off axis, so that only one DC coil is necessary to correct back onto the optical axis. For the simulations, the slit was assumed to be on axis. The goals of the simulations are to demonstrate chopping can be done within the microscope, and to test the beam quality after traversing the cavity.

6.1.1 Simulated Tecnai Implementation Results

In Sec. 5.1.2, the reduced brightness is given as $B_r = \frac{2q}{mc^2} \frac{I}{4\pi\epsilon_{N,x}\epsilon_{N,y}}$ where $\epsilon_{N,x/y}$ is the

normalized transverse emittance in the x/y -direction. For a current of 4 nA from a schottky emitter, the transverse emittance is found to be $\epsilon_{N,x/y}=3\times 10^{-12}$ m rad. The typical energy spread of a schottky emitter is ~ 1 eV. Because the streak is in one direction, the emittance growth is expected in only one direction (x) and expected to remain constant in the other (y). The numerical simulations proved this correct, as the growth in the y -direction was found to be less than 10^{-13} m rad and thus negligible.

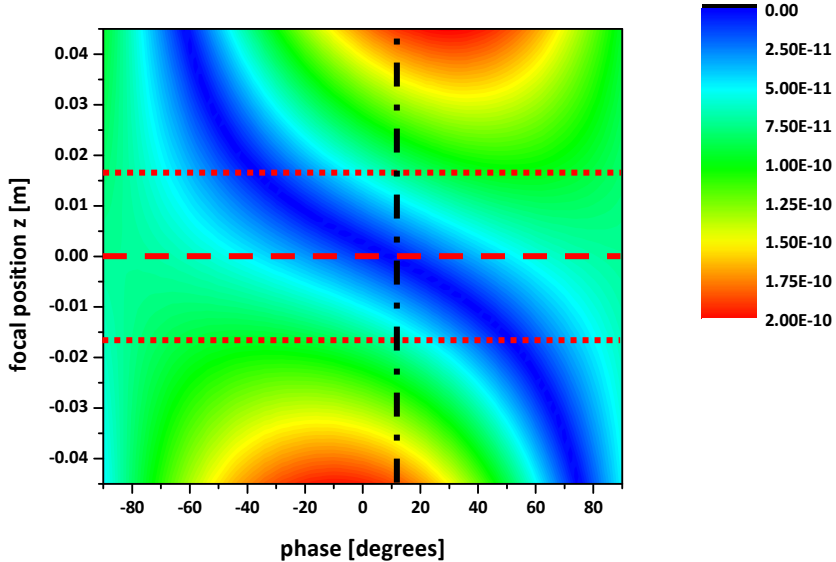


Figure 6.2: False color contour plot showing normalized transverse emittance (m rad) in the x direction as a function of entrance phase and focal position with respect to the cavity (positioned at $z=0$ m). The dashed red line denotes the center of the cavity, while the dotted red lines denote the beginning and end of the cavity. The black dashed-dotted line represents the 12 degree phase that will be chopped out in the situation considered.

Figure 6.2 demonstrates the phase-focal point dependence of the normalized emittance that was described and predicted in Ch. 5. For the short cavity-slit distance l , the phase which is chopped for an on-axis slit with size $15 \mu\text{m}$ is approximately 12 degrees. From Fig. 6.2 it can be seen that the transverse emittance can be minimized with proper focusing, thus maintaining a high peak brightness. Using Eq. 5.6 from the analytical model, the emittance is overestimated to be 7×10^{-11} m rad. Because of the large magnetic field amplitude, higher

order effects and correlations with other dimensions are expected to play a role, possibly explaining why the analytical model gives a larger growth than the simulations.

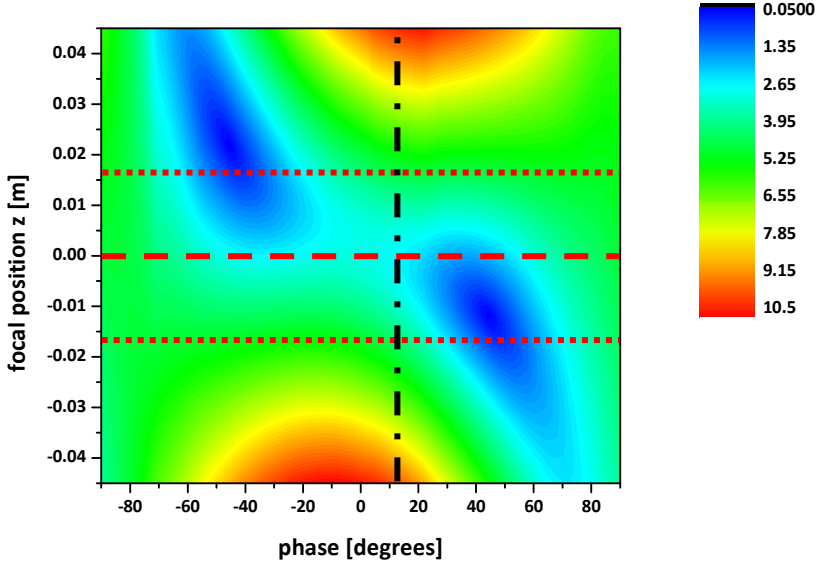


Figure 6.3: False color contour plot of the energy spread (σ_U from Ch. 5; i.e. standard deviation) as a function of focal position and phase with respect to the cavity (positioned at $z=0$ m). The FWHM is calculated by ~ 3.5 times the standard deviation, as is the case for a uniform distribution. The dashed red line denotes the center of the cavity, while the dotted red lines denote the beginning and end of the cavity. The black dashed-dotted line represents the 12 degree phase that will be chopped out in the situation considered.

Figure 6.3 shows the phase-focal point dependence of the energy spread as discussed in Ch. 5. The simulations predict an energy spread growth of nearly $\sigma_U=3$ eV which for a uniform distribution translates into 10.5 eV FWHM for the 12 degree phase which will be chopped out. Also, an important note, the energy spread no longer follows exactly the predicted behavior from Ch. 5. This is because the strong magnetic field causes a shift of more than 5 mm in the x -direction through the cavity. This causes the electron to “see” a large electric field, the main cause of energy spread growth; on top of this, the magnetic field deviates from the approximation of Eq. (5.1), no longer behaving as a uniform field in one direction.

For electron microscopy, an energy spread of 10.5 eV is far too high, and will cause large chromatic aberrations. To avoid this, the energy spread should be kept as low as possible. However, this is not the end-all to implementation. Solutions to reduce the energy spread growth will be presented in the next subsection.

6.1.2 Solutions to Reduce Energy Spread

The energy spread given to the beam in the implementation scheme shown in Fig. 6.1 is approximately 10.5 eV FWHM. Chapter 5 found the reason for this growth to be directly correlated to the electric field, which is sampled as the electrons go off axis. The off axis behavior is due to the magnetic field. So it logically follows that to reduce the energy spread, the power input to the cavity must be lower, and thus lower electric and magnetic fields. Three easily implemented solutions are presented.

The first solution, and the simplest, is to turn down the power to the cavity. The effect of this is that the magnetic field will be less. As a result the temporal bunch length τ will grow, as τ is inversely proportional to B_0 according to Eq. (2.22). For the dimensions given, if B_0 is reduced to 5 mT, then τ will grow to 250 fs. As a result, the energy spread for 250 fs bunches is only ~ 3.5 eV FWHM. This is already in the “good enough” regime, giving an energy spread comparable to a tungsten hairpin emitter. Turning down the power further will reduce the energy spread more, but also lengthen the temporal length of the bunch as a tradeoff.

The next solution is to alter the implementation scheme. This is a bit more difficult, but could turn out to be more fruitful in the end. According to Eq. (2.22), $\tau \propto (lB_0)^{-1}$, where l is the distance from the cavity to the slit. If this distance is increased to 7 cm, the field amplitude is roughly cut in half, giving a FWHM energy spread of ~ 3 eV. Lengthening l further to 10 cm would reduce the energy spread down to roughly 1.5 eV, while still maintaining the temporal length of 100 fs. There is also a tradeoff in this solution. The size of the slit was kept constant, but due to the beam parameters, not all of the beam would go through the slit if it is focused in the middle of the cavity while the cavity is off, essentially aperture limiting the beam. The beam would be aperture limited, reducing the current of each bunch. This may be problematic as the bunches are expected to have one or less than one electron per bunch, depending on the initial current.

The final solution is to not use 200 keV, but 100 or even 30 keV in the same scheme. The reason for using a lower acceleration voltage for the electrons is simple: they go slower. The slower the electrons, the smaller the cavity length, and as a result the distance from the cavity to the slit, l , increases making the requirement for B_0 to be lower. Using the same argument as before, a lower magnetic field gives a smaller energy spread. This may be a useful solution, but would be dependent upon the experiment and what electron energy is necessary.

These are just three of the possible solutions that could be used to implement the TM₁₁₀ cavity into a microscope. In all three situations there are tradeoffs between another parameter, but it is clear that the energy spread caused in the scheme given is not the full

stop towards implementation; it is also clear that the scheme as given does require a small detour to maintain a minimal emittance, energy spread, and temporal length.

6.2 Synchronization with a Laser: New Ideas

The importance of adding temporal resolution to an electron microscope is to study dynamic processes that occur on fs or ps timescales, such as molecular vibrations, solvation dynamics in liquids, and charge transfer in proteins as seen in Fig. 6.4 [2]. But in order to observe these processes, they have to be occurring at the time the electrons are spatially there probing the sample. This is where the importance of a laser comes into play.

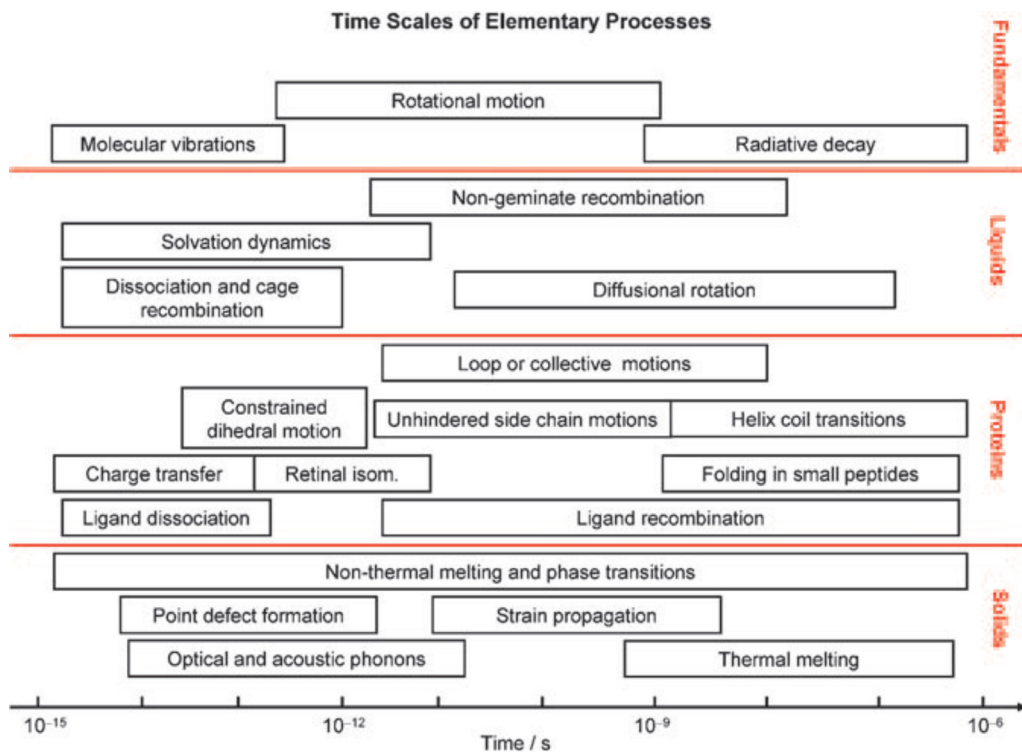


Figure 6.4: Table demonstrating various elementary processes that occur at short time scales. Image taken from Ref. [2].

In most ultra-short experiments, a pump-probe setup is used, with a fs laser pulse used to initiate the dynamic process (known as pumping the sample) and a second short pulse at some time delay to probe the process. The probe can be an electron or laser pulse, electrons in our case.

In order to repeatedly pump and probe a sample (as necessary when ~ 1 electron per bunch is present) then the arrival time between the pump pulse and probe pulse at the sample has to be stable to an accuracy of less than the pulse sizes, 100 fs in this case. For this reason, an in-house synchronization system was designed in 2001 by Kiewiet *et al.* [3]. The system synchronizes a 3 GHz electronic oscillator to a 75 MHz fs self-mode-locked Ti:sapphire laser oscillator with an RMS phase-jitter of less than 20 fs. With this the challenge of synchronizing a 3 GHz resonant cavity to a laser is achieved with an accuracy of better than 20 fs, more than sufficiently meeting the requirement of being less than 100 fs. This is done by taking the fifth harmonic of the 75 MHz signal and mixing it with one-eighth of the 3 GHz signal. This essentially allows the 3 GHz oscillator to lock to the 40th harmonic of the 75 MHz signal.

At this point, it is important to address the problem of having electrons at a repetition rate of 3 GHz (assuming half are blocked), and the 75 MHz repetition rate of the laser oscillator. The easiest solution is to use a fs laser that has a repetition rate of 3 GHz, as they have been developed with repetition rates up to 10 GHz [4]. However, these are not commercially available yet, and additionally not suitable for processes with longer relaxation times. A second possibility is to develop a fast blanker of only a few ns synchronized to the laser, allowing only a few electron bunches through for each laser pulse; to achieve one electron bunch per laser pulse, a blanker of < 300 ps would have to be developed, which is currently not feasible with standard electronics. The third option is the subject of the next subsection, using one cavity driven by two signals.

6.2.1 Dual Frequency TM_{110} Cavity

In Sec. 3.1.3, the elliptical design of the cavity was described, the main reason being to get the resonant frequency to 3 GHz to be used with the synchronizer previously described. In doing so, the cylindrical symmetry was broken, breaking the degeneracy of the two TM_{110} modes, oriented in x and y , respectively. This gives the two modes different frequencies, as seen in Fig. 3.4.

If the two modes are not sufficiently separated and one of them suppressed by impedance matching with the loop antenna, then the signal from the amplifier will drive both of the modes, with a $\pi/2$ phase shift with respect to each other. Also, due to the different resonant frequencies, the amplitudes of the two modes will be different. What occurs is the beam is swept from side to side in two directions harmonically with approximately the same frequency, but with a slight phase difference, giving the Lissajous figure on the detection screen, shown in Fig. 6.5.

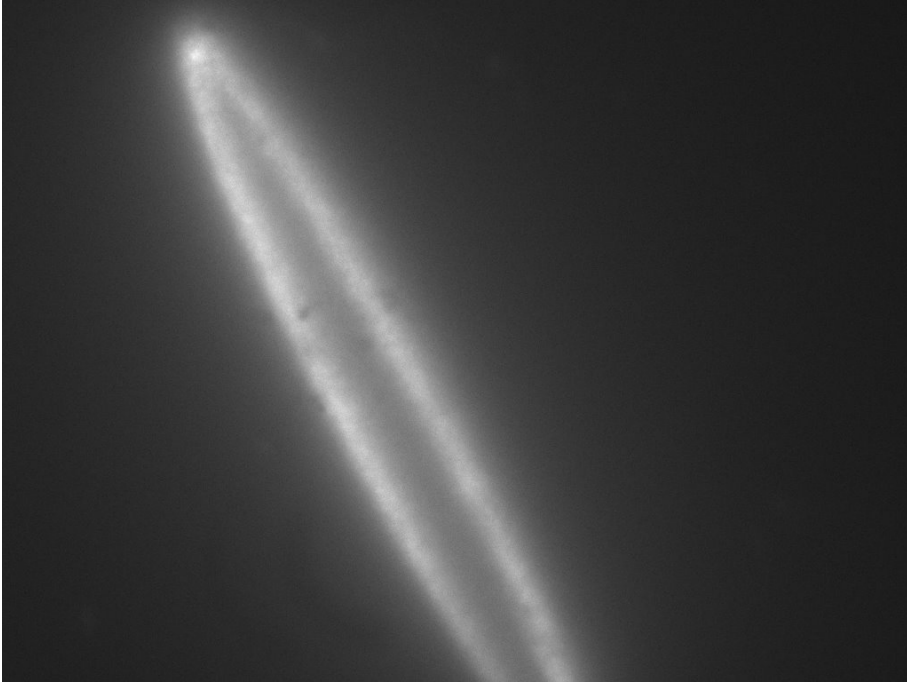


Figure 6.5: Two modes with a phase difference in one cavity, driven with one signal, observed on the detector in lab.

If a cavity is designed with two loop antennas, and two frequency tuners, in theory the two modes could be driven independent of each other. If the two modes have the same field amplitude, and are separated in resonant frequencies by $\Delta f = f_{0,a} - f_{0,b}$, then the pattern seen on a phosphor screen will have the pattern seen in Fig. 6.6. From the figure, it is clear that a pinhole will have to be used, instead of a slit. In the case of a pinhole, analogous to the single mode cavity, the beam will be streaked across the pinhole twice per beat period, $T_{beat} = 1/\Delta f$, instead of twice of the period of one mode.

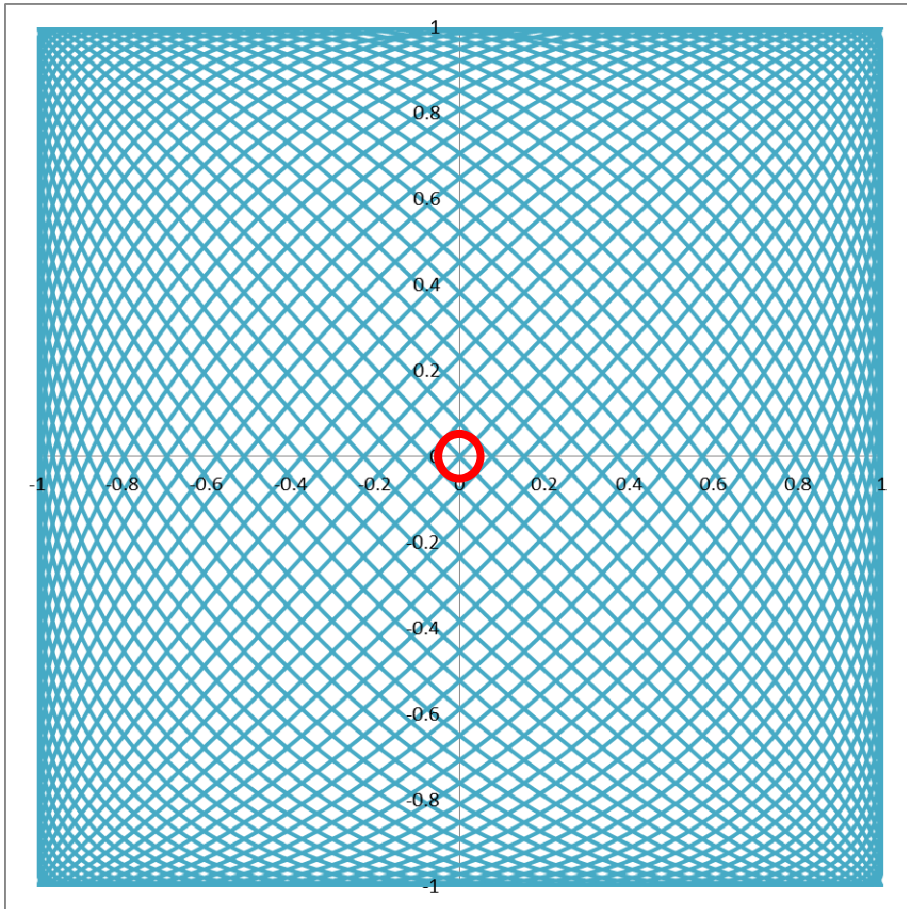


Figure 6.6: Simulated pattern seen on the screen when two modes are driven in one cavity with two separate signals. The red circle represents the location of the aperture for chopping. The amplitude is normalized, as the two maximum directions would depend on the two various amplitudes of the two modes.

In this way, by appropriately tuning the resonant frequencies of the two modes, one can, in theory, arbitrarily set the repetition rate of the electron bunches between $f_{0,a}=f_{0,b}=3$ GHz and Δf . If the first mode is set to 3 GHz, and the second mode to 3.075 GHz, then the repetition rate of the electrons will be 150 MHz if a crossing of trajectories is chosen, such as the circle seen in Fig. 6.6. Also, analogous to the single mode case, alternating bunches will have alternating signs in their transverse momenta, allowing one of them to be easily blocked, giving a repetition rate of 75 MHz, easily synchronized to a 75 MHz laser.

While this solution is elegant, it would require twice as much work and attention to detail in the designing and building of the cavity. The cavity would need two antenna inputs, two tuning stubs, as well as an elliptical design. On top of the cavity, twice as many RF

components (amplifiers, cables, synchronizers, etc.) are required. As for the synchronizers, some form of signal mixing would have to be done to bring the second mode to the 39th or 41st harmonic of the laser. This can be achieved by mixing a 75 MHz signal with a 3 GHz signal, followed by a filter to allow only the 39th or 41st harmonic signal through.

As a general comment of what may be a limit to this design, the two modes may need to be far enough apart such that their bandwidths do not overlap. This comes to a few MHz. This is fine if the laser pulses used for pumping are at a repetition rate of a few MHz or more, which is possible with a 75 MHz oscillator. However, if the amplified laser pulses are needed, they come at 1 kHz. This would require careful isolation of the modes as “seen” by the antennas. In practice, this would prove virtually impossible. It is much easier to design a blanker that operates at 1 kHz to synchronize with the probe pulse, and it would not have to be ultra-fast since the electron bunches are only coming every tens of ns rather than sub-ns.

6.3 Phase Control Between Two Cavities Running Simultaneously

Until now, the TM_{010} cavity has only been described in Ch. 2. As a quick refresher, the TM_{010} cavity is known as a compression cavity; it was designed to use the electric field along the z-axis to compress a few ps temporally long bunch down to 100 fs. With the combination of multiple cavities along a beam line, the beam can be manipulated transversely as well as longitudinally. In the following sections, some of the experiments that can be carried out with multiple cavities will be presented and simulated. However, as a proof of principle, it is vital to show that multiple cavities can be synchronized to the same signal, with a phase shifter used to vary the phase with respect to the two cavities.

In the beam line, a TM_{010} cavity was placed 50 cm downstream after the TM_{110} streak cavity. The streak cavity was turned on, with no slit in the way, giving a full streak on the screen. The TM_{010} cavity was then turned on, and the power increased. Both cavities were powered with the same 3 GHz signal, with a phase shifter added before the TM_{010} amplifier, giving the ability to shift the phase between the two cavities.

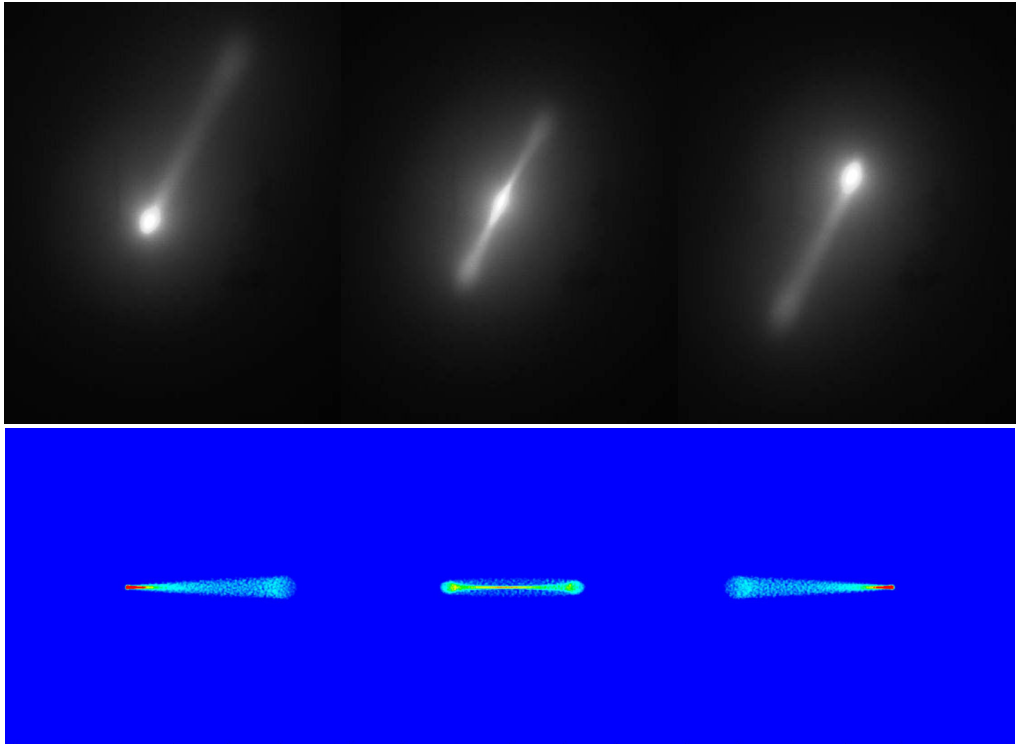


Figure 6.7: Phosphor screen measurement (top) and GPT simulations (bottom) of synchronization between two cavities, with phase differences between the cavities of 0, 90, and 180 shown from left to right. Rotation in the images are due to the rotation of the cavity as it is implemented in the beam line.

Most importantly, the two cavities are synchronized accurately to the same signal, and can have a phase delay between the two cavities easily added. However, Fig. 6.7 demonstrates multiple characteristics of the cavities. The normal streak, as shown back in Fig. 4.4, is distorted by the effects of the TM_{010} cavity, which is due to the focusing/defocusing of the TM_{010} cavity. This focusing/defocusing is seen in both simulations and in the experimental images. According to Pasmans *et al.*, this focusing/defocusing is a result of the electric fringe fields at the entrance and exit of the cavity [5]. It is also this phase dependent focusing/defocusing (with respect to the TM_{010} cavity) that van Oudheusden overcame with a solenoid [6], and that Oldfield recommended using as a form of spherical (see Sec. 6.5) and chromatic aberration correction [7].

With synchronization and phase control between multiple cavities demonstrated as well as synchronization with a laser, a multiple cavity experiment scheme will be described and simulated in the next section.

6.4 Poor Man's FEELS

Electron energy loss spectroscopy (EELS) is a technique used to study the change in energy of an electron beam due to interactions with a sample. Adding fs temporal resolution allows the Caltech dubbed "FEELS" acronym to apply. As a monochromatic beam passes through a sample, energy is lost to phonons, electron orbital transitions, plasmons, and ionization. As a result of the energy losses, the electron travels slower. In an EELS setup in a microscope, the electrons go through a standard spectrometer. Following the Lorentz force, electrons with a slower velocity will undergo a smaller force, and thus be deflected less than an electron that did not undergo any energy loss.

An alternate method to reveal the energy spectrum of a bunch after passing through a sample is proposed below in Fig. 6.8. Rather than using a powerful bending magnet to reveal the energy differences, a long drift space is used, seen in blue in Fig. 6.8. This long drift space ensures that the electrons with different velocities will have different arrival times to the second cavity, seen below. Different arrival times translate into different entrance phases, leading to different transverse velocities after traversing the second cavity.

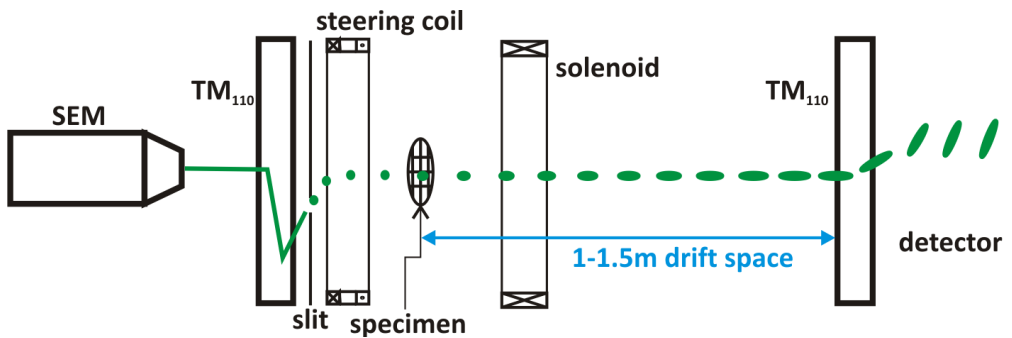


Figure 6.8: Schematic of the Poor Man's FEELS setup. The entire setup starting from the back end of the SEM to the detector was designed such that it fits on a 3 meter optical table.

The schematic demonstrates an entire setup scheme to measure the energy spectrum of electron bunches. The SEM provides a 30 keV DC beam, which goes through the first TM_{110} cavity, and then passes through a slit creating the fs bunches. The slit is placed off axis so that only one steering coil is necessary to return the beam back to the optical axis. A specimen is placed after that, for the electrons to interact with. Following is a solenoid used to focus the beam into the center of the second TM_{110} cavity. Between the specimen and the second cavity is between 1 and 1.5 m drift space, to allow the electrons with various velocities to separate. The longer the drift space, the higher the energy resolution that can be obtained. This drift space is for 30 keV electrons. For higher energies, the drift space must be extended. After the electrons have separated based upon their velocities, they reach the second TM_{110}

cavity, which streaks them to different positions on the detector, based on the different arrival times (and thus entrance phases with respect to the second cavity). In this scheme, the entire setup can be placed upon a 3 meter long optical table, from the very back of the SEM to the detector, making it an ideal scheme to be implemented in this project.

The scheme depicted in Fig. 6.8 was simulated in GPT for 100 fs bunches, with all foci placed inside both cavities. At the specimen, an energy distribution (seen on top in Fig. 6.9) was given to the beam, inspired by the FEELS study by Yurtsever *et al.* in which individual peaks were spaced 2.4 eV apart, corresponding to the laser energy $h\nu=2.4$ eV [8]. After drifting for 1 meter, the second cavity streaked the beam onto the screen.

From Fig. 6.9, it is clear that individual peaks spaced 0.75 eV apart can be resolved, with the appropriate intensities. The energy distribution given to the beam was a set of 11 peaks, evenly spaced, and given intensities that are exactly half of the next higher order peak. The histogram was given a binning of every 10 μm , roughly the size of a normal MCP channel.

When the separation between the peaks was decreased to 0.5 eV, 1 m drift space was found not to be enough, and could not resolve the peaks. However, increasing the drift space to 1.5 m allows for 0.5 eV to be resolved. From this, it is clear that a resolution of better than 1 eV can be achieved with two TM_{110} cavities, basic charged particle optics, and a 3 m optical table. For this reason, it has been dubbed the "Poor man's FEELS" since it does not require an expensive electron spectrometer.

The simulations were run with an emittance of 10^{-12} m rad, being similar to that from a Schottky emitter. Increasing the emittance reduces the resolution in this scheme. Simulations found for a resolution of 1 eV, a maximum emittance $\sim 5 \times 10^{-10}$ m rad is allowed, slightly under the measured emittance of the SEM in lab. The SEM in our lab is, however, designed to be equipped with a field emission gun (FEG) which has a lower emittance than the tungsten hairpin currently in use. An alternative is to use a third cavity, which will be discussed in Sec 6.4.1.

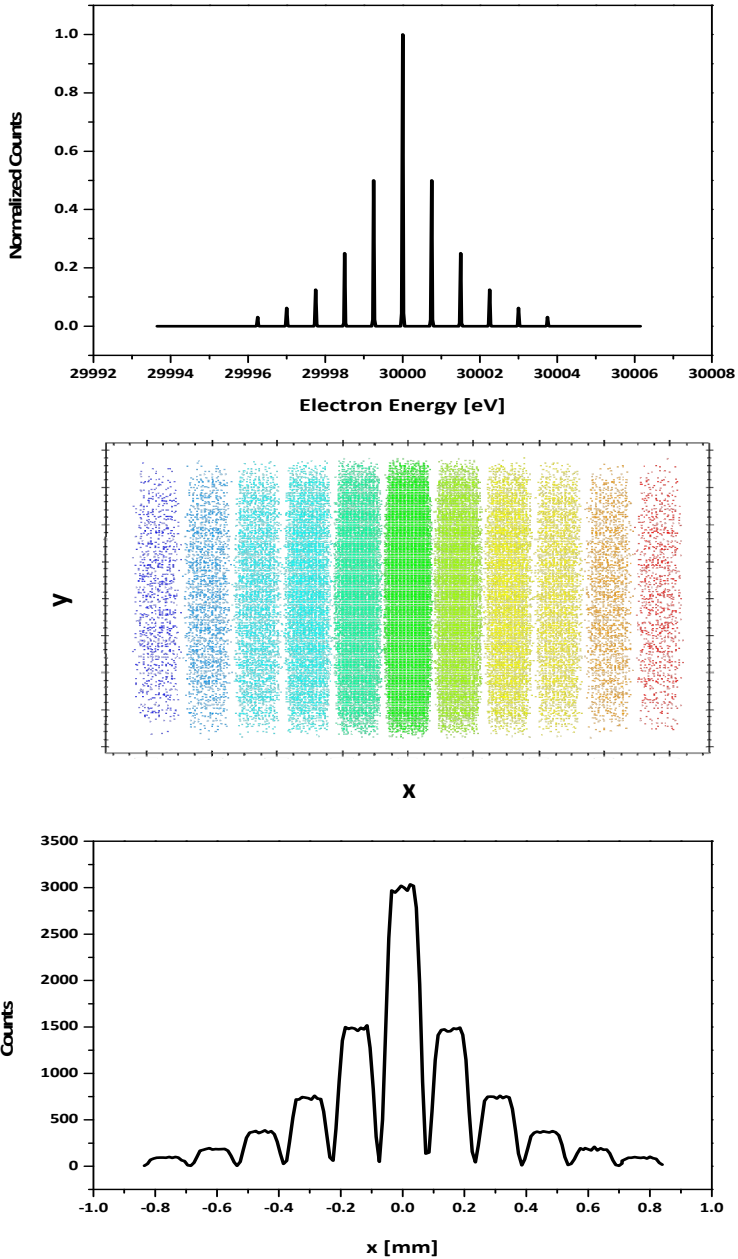


Figure 6.9: The top is the normalized energy distribution induced by the sample. Each peak is half the amplitude of the one before it, separated by 0.75 eV, with a FWHM of ~ 0.025 eV. The middle picture is what is seen on the detector, colored according to the energy given at the specimen. Each color represents a different peak. The bottom picture is a histogram of the middle picture.

6.4.1 Three Cavity Poor Man's FEELS Implementation Scheme for TU/e

As previously mentioned, the tungsten hairpin emitter system that we utilize in our lab does not have a high enough quality beam to carry out the FEELS experiments with sub-eV precision. An immediate solution that fits within the scope of this thesis is to utilize three cavities as time dependent phase space manipulators.

Because of the nature of the streak cavity in this scheme, the beam cannot be focused at the screen. This essentially is the limit of the resolution of the FEELS spectrum. The higher emittance in turn results in larger spots, blurring the energy resolution. One way to overcome this is to use a longer drift space to improve the resolution, as was demonstrated in simulations; a longer drift space gave better resolution. Longer drift space is not always practical. A trick to realize higher energy resolution in a compact setup is to “stretch” the bunch behind the sample.

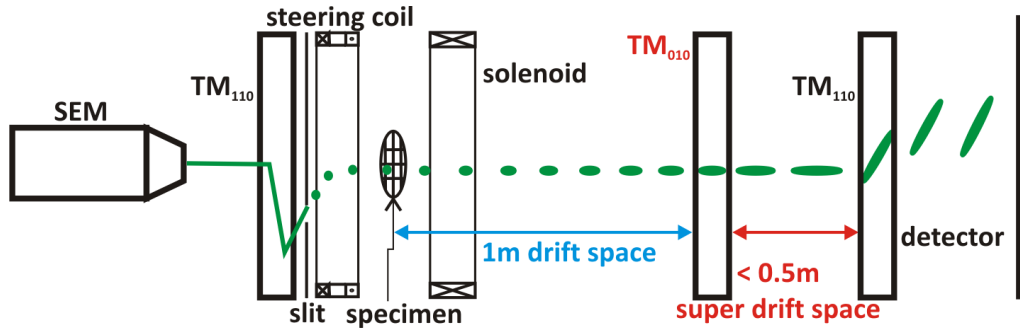


Figure 6.10: Three cavity scheme for implementation in our lab. The TM_{010} cavity is used to magnify the longitudinal energy spread of the bunch.

Figure 6.10 shows the scheme presented to achieve sub-eV resolution with the tungsten hairpin emitter system used in our lab. The emittance, measured to be $\sim 10^{-9}$ m rad, is the limiting factor in the setup without using the TM_{010} cavity. It reduces the resolution of the setup to a few eV. By placing the compression cavity in the beam line, and using it as an expander, i.e. a longitudinal magnifying lens, rather than a compressor, the resolution can be improved to sub-eV.

The first meter of drift space is to allow the various energies to separate out from each other, essentially expanding the 100 fs temporal length of the bunch. The TM_{010} cavity, seen in red in Fig. 6.10, must be set to a phase with respect to the bunch such that the center of the bunch will receive zero momentum change after traversing the cavity; and the cavity must accelerate electrons in front of the center of the bunch, and decelerate electrons in the back. This will cause the electron bunch to expand rapidly in the longitudinal direction. Because the

bunch at the point of the TM_{010} cavity is still much temporally smaller than half of a period of the cavity, the rapid longitudinal expansion will be approximately linear with respect to longitudinal position in the bunch.

This rapid expansion longitudinally results in larger differences in entrance phases of the final streak cavity with respect to the bunch, the same effect as if the beam had been allowed to drift naturally on its own, but uses only a fraction of the space.

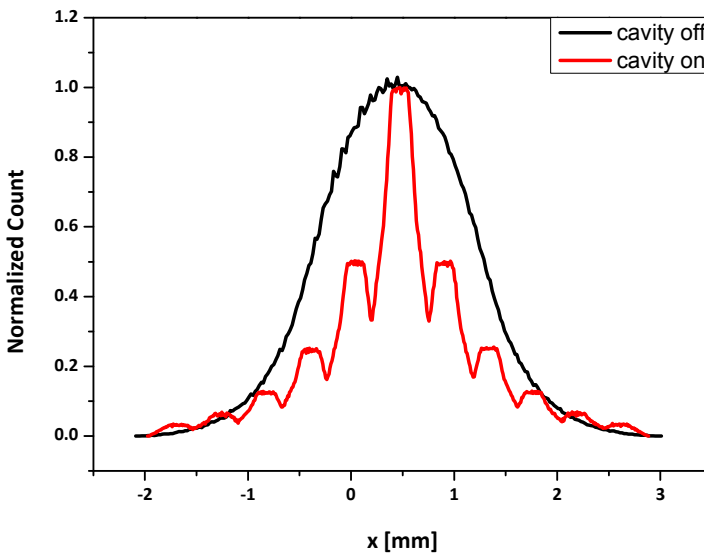


Figure 6.11: Normalized histogram as seen on the detector with the same given energy spectrum seen in Fig. 6.9 when the TM_{010} cavity is switched off (black) and when the cavity is switched on (red).

It is clear from Fig. 6.11 that the compression cavity allows for a higher resolution when used to expand the bunch longitudinally. Also, because the larger temporal length of the bunch when the TM_{010} cavity is used becomes larger at the final cavity, the required field amplitude in the final streak cavity is lower. Different amplitudes in the streak cavity were used in Fig. 6.11 to have roughly the same spread in x so as to compare the two cases.

6.5 Spherical Aberration Correction

Chapter 1 details previous work with cavities and pulsed sources in the 60's and 70's to bypass Scherzer theorem by relaxing the constraint of the lens having to be static. Due to technical limitations of the time in RF stability and computer simulating power, the work was stopped in favor of multi-pole focusing elements that break the cylindrical symmetry constraint of Scherzer [9]. It was not until recently that Schoenhense re-opened the discussion of using time-dependent fields in combination with pulsed electron beams. With as much work that has been previously published on using multiple cavities to correct for aberrations, it is the next logical step to investigate the feasibility of the aberration correction utilizing two cavities.

As a demonstration to illustrate spherical aberration caused by solenoids, the following setup was numerically simulated in GPT: a $200 \times 200 \mu\text{m}^2$ grid of electrons with a maximum divergence angle of $\alpha_0 = 14.2$ mrad and temporal length of 100 fs is allowed to expand a distance of $s_o = 0.75$ m to the solenoid with a focal distance of $f = 0.31$ m, followed by a distance of $s_d = 1.25$ m to the detector. The solenoid is modeled as a single turn solenoid, with the fields extending out from the center point. The solenoid is then followed by a TM_{010} cavity appropriately phased with the electron bunches to induce a negative spherical aberration coefficient. The spherical aberration coefficient is calculated to be $C_s = 1300$ m using the formula

$$C_s = \frac{S_o r_d}{s_d \alpha_0^3} + \frac{S_o}{\alpha_0^3} \tan(\alpha_0) \left(\frac{S_o}{s_d} - \frac{S_o}{f} + 1 \right), \quad 6.1$$

where C_s is the spherical aberration coefficient and r_d is the position on the detector [10].

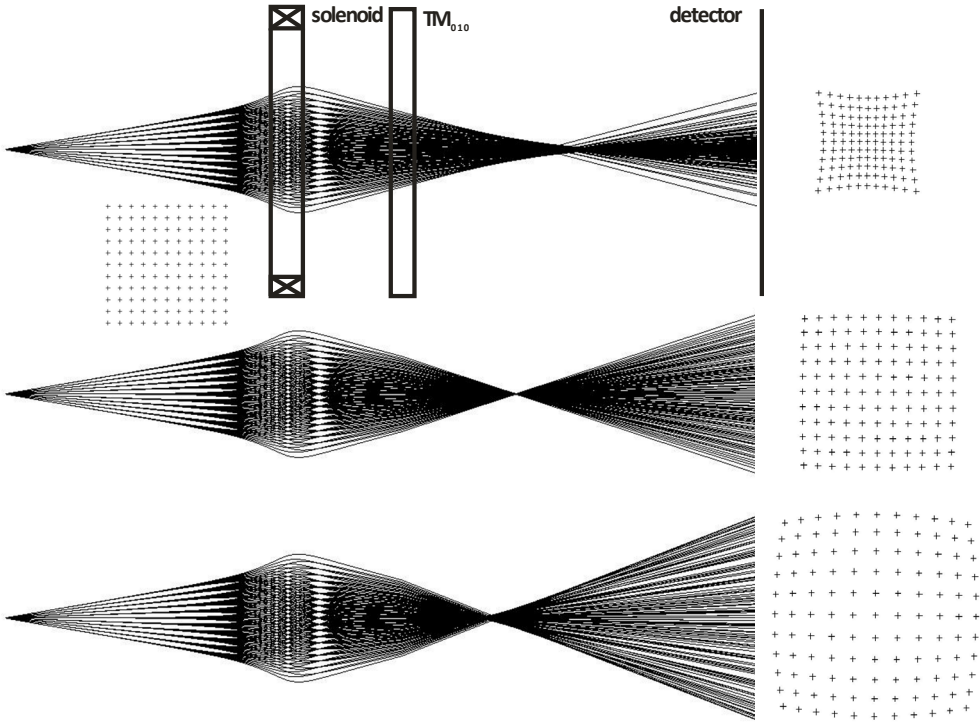


Figure 6.12: Top: xz ray tracing of electrons passing through a solenoid imaging system with a TM_{010} cavity used to demonstrate spherical aberration correction. Top to bottom: increasing electric field amplitude $E_0=0, 2.0, 4.0$ MV/m in the TM_{010} cavity. The initial starting array can be seen on the left between the top and middle plots. The xy array observed at the detector is seen on the right, rotated for comparison with the initial array.

The top half of Fig. 6.12 shows the general scheme used to demonstrate spherical aberration. The $200 \times 200 \mu\text{m}^2$ grid is seen in between the top and middle rows on the left. The grid expands, then focused by the solenoid, giving the pattern seen in the column on the right; if it was without aberration, the final grid pattern should be uniform, same as the initial pattern. The middle and bottom rows demonstrate what happens when the TM_{010} cavity is properly phased and switched on; nearly correcting the spherical aberration on the middle row, and showing with higher field amplitudes that the aberration can be overcorrected on the bottom row. For this particular setup, the correcting field strength is approximately $E_0=2.0$ MV/m. The simulation clearly demonstrates the ability of the TM_{010} cavity to act as a spherical aberration corrector. This is apparent in both the xz ray tracing as well as the final xy detector image. In the ray tracing, it can be seen that as the aberration is corrected, the focal point becomes sharper and more well defined; on the detector, the image goes from a pincushion shape to a barrel shape, moving through the correction point; but the spherical aberration correction comes at a price.

The particular phase of the TM_{010} cavity which gives this aberration correction is the same phase which, in Fig. 6.7, is seen as the focusing phase. As previously mentioned in Sec. 6.3, this phase is also the expansion phase of the cavity. This implies that the spherical aberration is corrected for, but at the cost of energy spread, which correlates into chromatic aberration. For an electric field amplitude of 4 MV/m, this corresponds to an energy spread growth of 3 orders of magnitude.

6.6 Conclusion

The group at Caltech led by Zewail has a system capable of performing pump-probe fs EELS measurements, dubbed “FEELS” [11]. Their system is an altered transmission electron microscope (TEM) which generates electron pulses by shining a fs laser on a cathode [12]. Carbone reports an energy spread of the bunches of ~ 1 eV delivered at a repetition rate of up to 1 MHz with 1 electron per bunch. In this setup, he reported pump-probe experiments on graphite with an energy resolution of ~ 1 eV. Yurtsever, working with an updated version of the same machine in Zewail’s group, reported pump-probe FEELS experiments with a resolution of ~ 100 meV, easily resolving structures spaced 2.4 eV apart [8].

Section 6.1 demonstrated the feasibility of using the TM_{110} cavity in an existing microscope, such as the one Zewail has had altered, but without the required use of a femtosecond laser for electron pulse generation. This can be done with an energy spread growth of ~ 1 eV, and a higher peak brightness ($\geq \sim 10^8$ A/(m² sr) [1] than a photocathode can achieve, ($\sim 10^6$ A/(m² sr) [13]). To achieve these numbers, alterations to the design for implementation would have to be carried through, with a myriad of possible solutions presented.

Section 6.2 discussed synchronization with a laser with minimal phase jitter, and presented an idea for reducing the repetition rate of the electrons to easily synchronize the electron bunches to a laser for pump-probe experiments. Section 6.3 showed synchronization between cavities to a single signal, with precise phase-control between the cavities.

Section 6.4 demonstrated a table top setup, known as the Poor man’s EELS, utilizing two streak cavities to resolve the FEELS spectra from a specimen with an energy resolution of sub-eV. The actual setup used in our lab does not provide a high enough quality beam to resolve sub-eV structures. But as Sec. 6.4.1 showed, a third cavity, the TM_{010} compression/expansion cavity, the energy resolution which was limited by the emittance can be overcome, and sub-eV structures can be resolved.

From this, it is clear that the term “Poor man’s FEELS” is an appropriate name for the scheme. Using all the devices shown in Fig. 6.10 and demonstrated in experiments and simulations, it is clear that similar experiments can be carried out with sub-eV energy resolution, comparable to that demonstrated by Zewail’s group, for a fraction of the overhead costs, and depending on the source for the electrons, perhaps better overall brightness. This was without any special charged particle optics. It might be possible that with an energy selection scheme (i.e. a slit), energy resolution may be improved into meV. But as a proof of principle, all the appropriate ingredients are there to make the Poor man’s FEELS a reality.

Finally, to bring cavity work in the scope of electron microscopy full circle back to the early work of Scherzer, Ura, and Oldfield, the principle of using a pulsed beam in correlation with a properly phased TM_{010} cavity to bypass Scherzer’s theorem and correct for the spherical aberration caused by cylindrically symmetric static solenoid lenses. In this scheme, the spherical aberration is corrected, but at the expense of energy spread/chromatic aberration.

References

- [1] FEI Company. "FEI Internal Document." n.d. *FEI Company*. <www.fei.com>.
- [2] Zewail, Ahmed H. "4D Ultrafast Electron Diffraction, Crystallography, and Microscopy." *Annu. Rev. Phys. Chem.* 57 (2006): 65-103.
- [3] F.B. Kiewiet, A.H. Kemper, O.J. Luiten, G.J.H. Brussard, M.J. van der Wiel. "Femtosecond synchronization of a 3 GHz RF oscillator to a mode-locked Ti:sapphire laser." *Nuclear Instruments and Methods in Physics Research A* 484 (2002): 619-624.
- [4] A. Bartels, D. Heinecke, and S.A. Diddams. "Passively mode-locked 10 GHz femtosecond Ti:sapphire laser." *Optics Letters* 33 (2008): 1905-1907.
- [5] P.L.E.M. Pasmans, G.B. van den Ham, S.F.P. Dal Conte, S.B. van der Geer, O.J. Luiten. "Microwave TM_{010} cavities as versatile 4D electron optical elements." *Ultramicroscopy* 11475 (2012).
- [6] van Oudheusden, T. *Electron Source For Sub-Relativistic Single-Shot Femtosecond Diffraction*. Eindhoven: TU Eindhoven, 2010. Thesis.
- [7] Oldfield, L. *Microwave cavities as electron lenses*. Cambridge: University of Cambridge, 1973. Thesis.
- [8] A. Yurtsever, R.M. van der Veen, A.H. Zewail. "Subparticle Ultrafast Spectrum Imaging in 4D Electron Microscopy." *Science* 335 (2012): 59-64.
- [9] G. Schoenense, and H. Spiecker. "Correction of chromatic and spherical aberration in electron microscopy utilizing the time structure of pulsed excitation sources." *J. Vac. Sci. Technol. B* 20 (2002): 2526-2534.
- [10] Reimer, Ludwig, Kohl, and Helmut. *Transmission Electron Microscopy*. Springer Series in Optical Sciences (2004).
- [11] F. Carbone, B. Barwick, O.H. Kwon, H.S. Park, J.S. Baskin, A.H. Zewail. "EELS femtosecond resolved in 4D ultrafast electron microscopy." *Chemical Physics Letters* 468 (2009): 107-111.
- [12] Zewail, Ahmed H. "Four-Dimensional Electron Microscopy." *Science* 328 (2010): 187-193.
- [13] O. Bostanjoglo, R. Elschner, Z. Mao, T. Nink, M. Weingaertner. "Nanosecond electron microscopes." *Ultramicroscopy* 81 (2000): 141-147.

7 Fundamental Photon-Electron Interaction

Thus far, the dynamics of electrons passing through radio frequency electromagnetic fields have been explored. With ultrashort electron bunches which can be synchronized to a laser, it seems reasonable that the next logical step would be to study the manipulation of electrons by means of a light field. This chapter presents an overview of electrons passing through the electromagnetic fields oscillating at optical frequencies of a laser rather than a resonant RF cavity. First a general description of the dynamics of a free electron in a standing light wave will be given. Following, the fundamental motives for investigating free electrons in a standing light wave will be discussed, followed by a summary of various applications that have been suggested. Finally, a feasibility study will be presented of utilizing one of the applications, longitudinal bunch length characterization, with the 30 keV altered SEM beam line.

7.1 Free Electron in a Standing Light Wave

Consider two counter propagating plane electromagnetic waves. If both waves are polarized in the same direction, the electric and magnetic fields will create a standing wave pattern. Assuming the waves are traveling in the $\pm x$ -direction, and are polarized in the z -direction, then [1]

$$\vec{E} = E_0 \cos(kx) \cos(\omega t) \hat{z}, \quad 7.1$$

$$\vec{B} = \frac{E_0}{c} \sin(kx) \sin(\omega t) \hat{y}. \quad 7.2$$

Equations (7.1) and (7.2) can be seen pictorially in Fig. 7.1. Using Fig. 7.1, the simple classical dynamics picture will be explained of a free electron in the standing wave. In Fig. 7.1, the top half is at some arbitrary time t' while the bottom half is depicted at the arbitrary time $t' + \pi/\omega$, or half a period later.

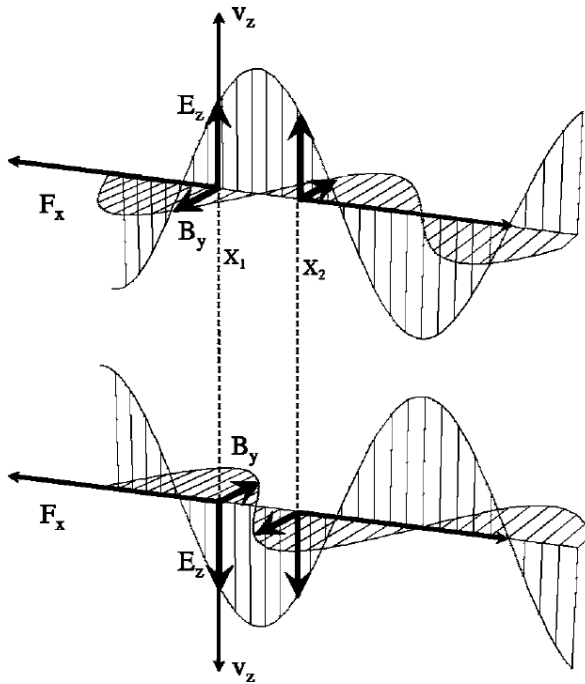


Figure 7.1: Standing electromagnetic waves, polarized in the z-direction. The bottom half is depicted at a time π/ω later than the time depicted in the top half. In the figure, the E_z field gives a velocity v_z which then, using the Lorentz force and B_y yields F_x . This picture is adapted from Ref. [1].

Consider a free electron placed at position x_1 at time $t=0$ with no initial velocity, seen in Fig. 7.1. Following the Lorentz force equation, the electron is accelerated by the electric field in the z-direction. This velocity, being perpendicular to the magnetic field, will cause the electron to be pushed in the x-direction. A subtle detail that arises is that the velocity given to the electron from the electric field oscillates with the same phase as the magnetic field. As a result, the Lorentz force gained by the magnetic field will not average out to zero over an oscillation, as both the velocity and magnetic field oscillate in time with each other.

From Eq. (7.1) and (7.2), it is clear that the equations of motion give the force as

$$F_x = \frac{q^2 E_0^2}{2mc\omega} \sin(2kx) \sin^2(\omega t). \text{ Averaging over an optical cycle yields}$$

$$\langle F_x \rangle = \frac{q^2 E_0^2}{4mc\omega} \sin(2kx) \approx \frac{q^2 E_0^2}{2mc^2} x, \quad 7.3$$

where the approximation is done for values around $x=0$. The electric field, according to Eq. (7.1), is maximum around $x=0$, so from Eq. (7.3), the electrons are pushed away from the electric field maximum. Since $\frac{\partial}{\partial x} \langle E_x^2 \rangle = -\frac{\omega^2}{c^2} E_0^2 x$ around $x=0$, Eq. (7.3) may be rewritten as

$$\langle F_x \rangle = -\frac{q^2}{2m\omega^2} \frac{\partial}{\partial x} \langle E_x^2 \rangle \equiv -\frac{q^2}{2\varepsilon_0 mc\omega^2} \frac{dI}{dx}, \quad 7.4$$

where I is the intensity of the light. This force is called the ponderomotive force. It can be shown that in general [1]

$$\vec{F}_{pomo} = -\frac{q^2}{2\varepsilon_0 mc\omega^2} \nabla I, \quad 7.5$$

with an intensity amplitude $I = \frac{E_0^2 \varepsilon_0 c}{2}$ relating to the electric field. This equation shows that the charged particle is pushed away from the field intensity maximum, towards lower intensity areas.

In 1933, Pyotr Kapitza and P.A.M. Dirac proposed to use a standing electromagnetic wave from light to diffract a well-collimated electron beam [2]. They took the work of Davisson and Germer, which demonstrated that electrons could be diffracted from a crystal lattice [3], and extrapolated that if the crystal lattice was replaced with a standing light wave, the light would serve as a grating which would diffract the electrons, known as the Kapitza-Dirac (KD) effect. In order for the electrons to be diffracted, they must no longer be just a free electron in a standing light wave, but now must have an initial velocity, which we will designate as v_z . Unfortunately at the time, the best light source would only produce enough intensity to scatter roughly 1 in 10^{14} electrons.

Rather than considering the standing light wave as a field, scattering of electrons by a standing light wave may be treated quantum mechanically. From Eq. (7.5) and Fig. 7.1, it follows that the electrons experience a ponderomotive potential $U_{pomo} = \frac{q^2 I}{2\varepsilon_0 mc\omega^2}$; in the case of a standing wave, the potential acts like a "grating" for electron waves with a grating period of $a = \frac{\lambda_{opt}}{2}$, where λ_{opt} is the optical wavelength of the light. Using Bragg's law, we

find electrons will be scattered by the standing light wave grating into discrete angles, given by

$$\sin \vartheta_n = n \frac{\lambda_e}{a} = 2n \frac{\lambda_e}{\lambda_{opt}}, \quad 7.6$$

where $n=0, 1, 2, \dots$ $\lambda_e = \frac{h}{p_z}$ is the electron's de Broglie wavelength associated with the

momentum of the electrons, based upon the initial velocity v_z . For a 30 keV beam, this gives scattering angles of a few tens of microradians. When the angular spread of the electrons is greater than the Bragg angle, then the quantum mechanical description no longer is necessary, and the classical description described previously is sufficient.

Finally, the scattering process may be considered in terms of collisions between electrons and photons. As the electron enters the light field, the electron collides with a photon travelling in the $+x$ -direction. Immediately following, a photon from the $-x$ -direction collides with the electron, causing stimulated emission. By conservation of momentum, the electron will recoil in the x -direction with a momentum of $2\hbar k = 2 \frac{h}{\lambda_{opt}}$, as the two photons leave in

the opposite direction of the electron recoil, reproducing the Bragg angles. For this reason, the ponderomotive effect is sometimes known as the stimulated Compton effect, although it has not been rigorously justified [1].

7.2 Fundamental Motivation

As previously described, the ponderomotive effect is an interesting topic for many reasons. It provides a playground for theoretical treatments, both classically and quantum mechanically. The fact that both the electrons and the photons can be viewed as fields or particles affords a variety of predictions and theories, as varied as the parameter space for the electrons and light can allow. Experimental verification (ideally) requires a strong light field and high angular resolution of the electron beam, i.e. amplified fs laser pulses and a small angular divergence (and thus low emittance) of the electrons. This is only possible if the laser pulses and electron beam overlap temporally and spatially, implying synchronization between low emittance electron bunches and a fs laser system. As discussed in Ch. 5 and Sec. 6.2., our setup appears ideal for studies of the interaction between free electrons and light.

The following two subsections discuss two possible fundamental experiments: investigation of the dependence of the force with respect to the polarization of the light wave; and diffraction of electrons from the light wave- the Kapitza-Dirac effect.

7.2.1 Classical Polarization Dependence

The classical description of the ponderomotive force in terms of a potential, $\vec{F}_{pomo} = -\vec{\nabla}U_{pomo}$, implies that the force is independent of the polarization of the light field, seen in Eq. (7.5). Looking back at Fig. 7.1, and using the same classical argument given to derive the ponderomotive force, one could easily come to the questions, “What happens when the electron has an initial velocity, v_z ? And does anything differ when the polarization is changed?”

Using the same classical argument as before, consider the electron in Fig. 7.1 to now have an initial velocity v_z . With a velocity in z , if the magnetic field is perpendicular to the velocity, $\vec{B} = B_y \hat{y}$, then both the electric and magnetic field work on the electron; if the magnetic field is parallel to the velocity, $\vec{B} = B_z \hat{z}$, then only the electric field works upon the electron. From this simple argument, there should be a polarization dependence.

However, Eq. 7.5 does not reflect this, as was discussed by Ref. [4]. Smorenburg *et al.* recently generalized this into the following form [5],

$$\vec{F}_{pomo} \approx -\frac{q^2}{2\gamma^{(0)}m\omega^2} \nabla \langle \bar{E}_{y,z}^2 - 2(\beta_{0z} \cdot \bar{E}_{y,z})^2 \rangle, \quad 7.7$$

where $\gamma^{(0)} \approx \sqrt{1 + \frac{\bar{P}^2}{m^2 c^2} + \frac{q^2 E_0^2}{2m^2 c^2 \omega^2}}$ is the averaged Lorentz factor and $\beta_{0,z} = v_z/c$ is the initial normalized velocity and the overbar denotes averaging at the guiding center position of the electron [5]. This generalized form was found to hold under four conditions. The first is that the laser is not too intense, $\leq 10^{17}$ W/cm², otherwise the electron motion in the field becomes relativistic. The second is that the laser focus is not too tight as to violate the paraxial approximation. The third is that the laser pulses are not too short, ≥ 5 fs, i.e. the slowly varying envelope approximation. The final assumption is that the electrons are well collimated, meaning that $\beta_{0,x/y} \ll \beta_{0,z}$. These are all reasonable realistic parameters, easily obtained under most laboratory conditions and covering a wide range of applications.

Using $I = \frac{E_0^2 \epsilon_0 c}{2}$, it is clear that Eq. (7.7) reduces to Eq. (7.5) with the Lorentz factor correction when the electric field is polarized in y . Also, if $\beta_{0,z} \rightarrow 0$, then Eq. (7.7) reduces to Eq. (7.3), for the free electron case mentioned in Sec. 7.1. It is also interesting to notice that when the electric field is polarized in z , the ponderomotive force is reduced below

$\beta_{0,z} = 0.707$, switches sign above $\beta_{0,z} = 0.707$, and equals zero for $\beta_{0,z} = 0.707$, which was confirmed with numerical simulations. $\beta_{0,z} = 0.707$ is the equivalent of an accelerating voltage of 212 keV, easily obtained by many electron accelerators and electron microscopes. Clearly, interesting predictions arise that could be verified within an RF-chopped EM setup.

Mentioned previously, the spread of the electrons from the standing light wave is dependent upon the velocity of the electrons and the polarization of the standing light wave. It would be interesting to experimentally confirm this, particularly since Eq. (7.7) was developed within our research group, CQT.

One way of testing the polarization dependence would be to change the polarization from E_y to E_z . The observed scattering should be of different lengths. According to Eq. (7.7), for a 100 keV beam, the differences in lengths of the scattered electrons should be about 50% larger for y polarization than for the z polarization. For a 30 keV system, the difference should be approximately 20%, feasible within the parameters of the altered SEM setup described in Ch. 5. Ideally would be a system which could span from 30 to 300 keV.

With a 30-300 keV microscope and E_z polarization, as the accelerating voltage is increased up from the 30 keV, the angle of the scattered electrons would continue to decrease until ~ 212 keV, at which point no effect should be seen. Around the 212 keV mark, one may even be able to observe a ponderomotive focusing effect, depending on the quality of the electron beam. Above the 212 keV mark, the angle of the scattered electrons should again increase.

A final suggestion for experiments demonstrating the polarization dependence would be to use circularly polarized laser light. In this scheme, the scattered length should oscillate between the y and z linearly polarized cases, oscillating at a frequency dependent upon the period of the polarization. If this period is fast enough, one could devise a scheme to chop out short pulses from the scattered electrons, analogous to the chopping scheme with the TM_{110} cavity.

As a quick check for the feasibility of detecting a ponderomotive interaction in our system, we start with a 100 fs laser pulse at 800 nm set to only 50 μ J per pulse. This will give a peak intensity of $I = 5 \times 10^{14}$ W/cm². Using the approximation $|\nabla I| \approx 4I/\lambda$, Eq. (7.5) yields a force of $F_{pomo} \approx 5 \times 10^{-11}$ N. If we assume that the momentum gained is approximately the force times the interaction period, we find a momentum from the interaction of $p_x \approx F_{pomo} \tau = 5 \times 10^{-24}$ kg m/s. The angular spread is then $\theta \approx \frac{p_x}{p_z} = 0.06$ rad, where

$p_z = mv_z = 9 \times 10^{-23}$ kg m/s. This must be larger than the inherent angular spread of the beam.

In Ch. 5, the normalized emittance was measured at ~ 1 nm rad. If we assume a beam with a radius of 50 μm , then to a close approximation the standard deviation is $\sigma_x \approx \frac{R}{2} = 25 \mu\text{m}$. The geometrical emittance is related to the normalized emittance by $\varepsilon_N = \gamma\beta\varepsilon_g$ and defined as $\varepsilon_g \equiv \sigma_x\sigma_\theta$. For a 30 keV beam, $\gamma \approx 1$ and $\beta \approx \frac{1}{3}$, which leaves us with an angular spread of $\sigma_\theta \approx 10^{-4}$ rad. This is well under the spread from the ponderomotive force, found to be 0.06 rad; the emittance of the SEM beam should not be a problem in detecting an electron-light interaction. A more detailed discussion will be presented in Sec. 7.3.3.

7.2.2 Electron Diffraction from a Standing Light Wave

It took more than 60 years of technological advances in lasers and electron sources to have the KD effect finally realized experimentally by Freimund [6]. The peaks were resolved at the expected $\pm n2\hbar k$, where $n=0, 1, 2, \dots$. This is the first time, and only to date, that electrons have been diffracted from a standing light wave.

Briefly explained in Sec. 7.1, the quantum mechanical view predicts quantized electron transverse momentum transferred from the laser pulses. But as also mentioned, this quantum electro-dynamic (QED) view is lacking and not rigorously justified. For this reason, Batelaan has described the KD effect as, "...a testing ground for non-perturbative treatments in QED," [1].

7.3 Applications of the Pomo and KD effects

Proposed applications of the ponderomotive effect have included novel x-ray-free electron laser schemes [7], attosecond electron pulse train generation by two different wavelength lasers [8], pre-acceleration schemes for laser-wakefield set-ups [9], and diffraction from two wavelength lasers without a standing wave scheme [1]. This section will be devoted to coherent beam splitting and bunch-length characterization.

7.3.1 Coherent Beam Splitter

The KD effect has been used extensively in atom optics, since the near resonance interaction with atoms increases the effect by roughly nine orders of magnitude [1]. For this reason, much more work has been put into light interacting with atoms, rather than electrons. Because of this large difference in interaction with light, atom optics has utilized

the KD effect as a coherent beam splitter. It has even been used to create atom interferometers [10,11].

In 2001, Freimund demonstrated experimentally the diffraction of electrons from a standing light wave, as Kapitza and Dirac had predicted in 1933 [6]. With this coherent splitting demonstrated but a rigorous QED description lacking, it is still an open ended question as to whether an electron interferometer can be constructed [1]. One advantage to this method over other electron interferometers is that there is no need for materials near the free electrons. According to Forrey, this would allow for interferometric measurements in the low-energy ranges typical for atomic physics, and possibly enable time-resolved, fs holography [12].

But it would be naïve to think this an easy feat to accomplish. There is a reason it took nearly 70 years to first observe electron diffraction from a standing light wave, and the same reason applies as to why it is only been observed once: it is experimentally challenging. If all beams are aligned spatially and temporally, detection still remains a challenge. These challenges are similar to ones that will be described in more detail in Sec. 7.4.

In order to resolve peaks in the diffraction pattern, the angular spread of the beam must be smaller than the angle subtended by the first order diffraction peak, given by Eq. (7.6). For a 30 keV beam, the de Broglie wavelength is $\lambda_e = 7.3$ pm, yielding the angle of the first diffraction peak to be $\mathcal{G} \approx 20$ μ rad, assuming an 800 nm laser. If we consider the laser to be a 100 fs pulsed laser, then the width of the standing wave pattern in the x -direction will be $c\tau_{laser} = 30$ μ m. This implies that to be scattered, an electron must be in this 30 μ m width; from this, we will approximate that at the point of interaction, the standard deviation of the electron beam in x to be $\sigma_x \approx \frac{c\tau_{laser}}{2} = 15$ μ m. As we mentioned before, the angular spread of the beam must be less than the spread of the first diffraction peak, approximated as half of the angular spread off the diffraction peak, $\sigma_\theta < \frac{\mathcal{G}_{pomo}}{2} = 10$ μ rad. In order to detect diffraction peaks with a 100 fs 800 nm laser and a 30 keV beam, the normalized transverse emittance must be $\varepsilon_N = \gamma\beta\sigma_x\sigma_\theta = 5 \times 10^{-11}$ m rad.

This is dramatically lower than our W-hairpin SEM system. Either a better source would be required, or the beam must be aperture limited, reducing the signal. A second option is to increase the pulse length of the laser. If the pulse length is increased to 1 ps, then the electrons do not have to be focused to as short of a focus, reducing the restriction on the emittance by an order of magnitude, putting it within the range of our system.

7.3.2 Bunch Length Measurements

In 2005, Siwick *et al.* proposed a technique to measure the length of ultra-short electron bunches [13]. The initial idea was to use a fs laser pulse overlapped with a fs electron bunch, and use the scattering from the ponderomotive force to determine the length of the electron bunch. By delaying the laser pulse's arrival time with respect to the electrons, one can determine the longitudinal length of an electron bunch. This scheme was experimentally achieved by Hebeisen in 2006 [14]; the general effect was improved by Hebeisen in 2008 by overlapping two pulses, giving the configuration described in Sec. 7.1 and seen in Fig. 7.1. The reason for using overlapping pulses is to create the standing wave pattern. In the standing wave pattern, the gradient of the electric field varies with $\lambda_0/4$, rather than with the shape of the pulse $c\tau_{laser}$, where τ_{laser} is the temporal length of the laser pulse. The standing wave configuration gives an enhancement to the effect by two orders of magnitude as compared to a single laser pulse [14].

The general idea behind ponderomotive electron bunch length measurements is straightforward, as seen below in Fig. 7.2.

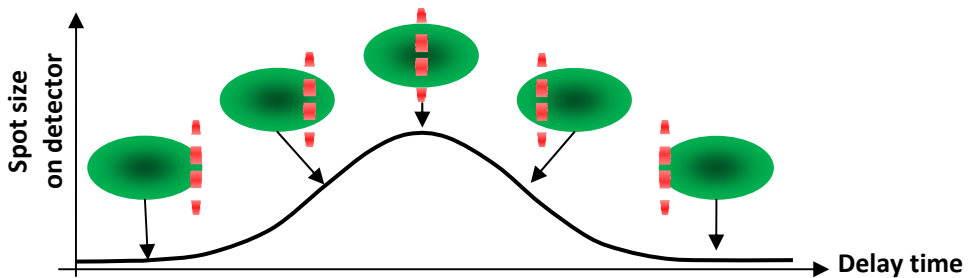


Figure 7.2: General Scheme of how a ponderomotive bunch length measurement works. By delaying the arrival time of the laser pulses with respect to the electron bunch, the longitudinal length of a bunch can be determined.

If the two laser pulses are overlapped spatially and temporally, they will create the standing light wave pattern. If the electron bunches are also overlapped spatially with the standing wave, the electrons will be scattered, producing a larger spot on the detector than if no lasers are present. By delaying the arrival time of the laser pulses, the amount of spread detected from the laser-electron interaction will be reduced, as it is proportional to the part of the electron bunch that is overlapped spatially and temporally with the lasers. In this way, a localized probing of the electron density along the z-axis within the bunch is achieved.

A numerical simulation in GPT [15] to test the extraction of pulse length from data was carried out. The gaussian laser beam was modeled to include the electric and magnetic fields, temporal length of the laser pulse, Rayleigh length, and the Gouy phases; the field equations used can be found in Appendix D. The parameters for the laser were specified as a spot size

of $w_0=25\ \mu\text{m}$ at the focus, a temporal length of $\tau_p=100\ \text{fs}$, a wavelength of $\lambda_0=800\ \text{nm}$, and an energy per pulse of $56\ \mu\text{J}$ corresponding to an intensity of $I_0=5.4\times 10^{13}\ \text{W}/\text{cm}^2$, giving an electric field amplitude of $E_0=2\times 10^{10}\ \text{V}/\text{m}$. The electron bunch was simulated as a collimated 3-D gaussian bunch of temporal length $\tau_e=100\ \text{fs}$, radius of $R_e=50\ \mu\text{m}$, and initial velocity $\beta_{0z}=0.5$ ($\sim 100\ \text{keV}$). Figure 7.3 shows the results for the case of z linearly polarized light.

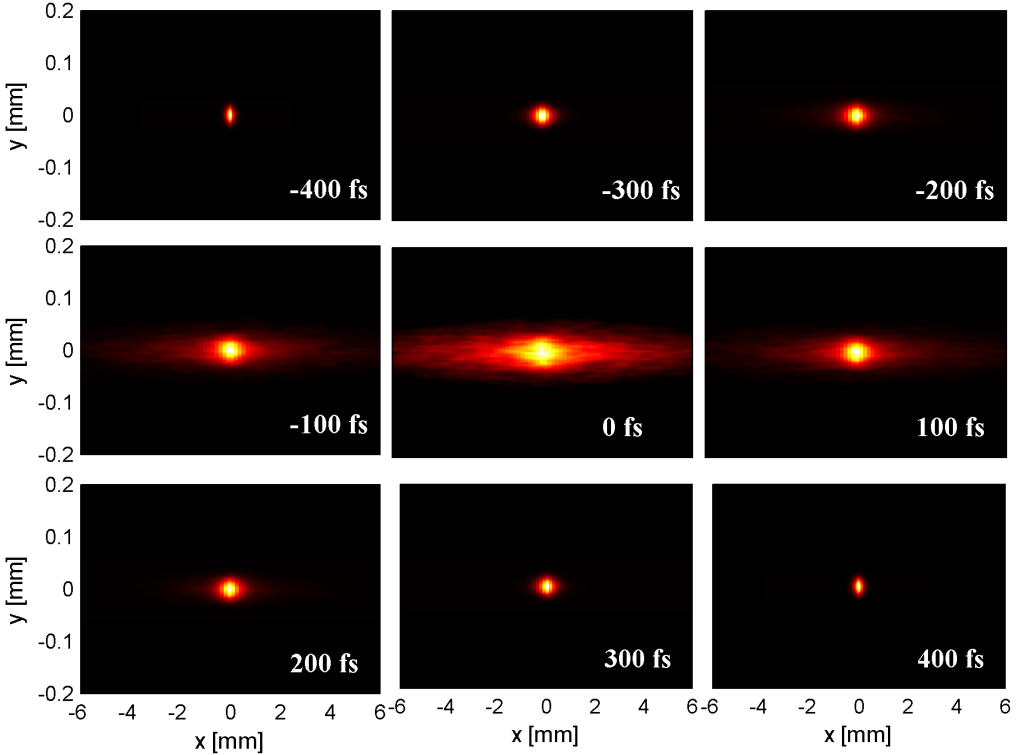


Figure 7.3: Simulation demonstrating what would be seen on the screen 0.2 m behind the ponderomotive interaction point. The arrival time of the laser pulses is delayed with respect to the electron bunch, with 0 fs equating to the lasers being in the middle of the electron bunch.

The simulation was run with linearly polarized light, with the electric field oriented in both y (seen in Fig. 7.3) and in z . Using the information from the numerical simulations, the temporal length was determined to be $\tau_e=101 \pm 1\ \text{fs}$ for the E_y polarization and $\tau_e=99 \pm 1\ \text{fs}$ for the E_z polarization, in excellent agreement with the 100 fs input. The same simulations were run with a uniform cylindrical distribution for the electron bunch, with the length of the cylinder corresponding to the temporal length of the bunch. This gave temporal lengths of $\tau_e=103\ \text{fs}$ and $\tau_e=95\ \text{fs}$ for the E_y and E_z polarizations, respectively [16]. It is clear at this point that the technique can be used very accurately for electron bunch length diagnostics for various electron distributions.

7.4 Feasibility of Ponderomotive Bunch Length Measurements in the Beam Line

To this point, the ponderomotive bunch length measurement has been studied and detailed to great length. The next step would be implementation into the 30 keV SEM beam line described in Ch. 4 and seen in Fig. 4.1. As designed, there are a number of complications that must be overcome to achieve detection of the ponderomotive scattering in this configuration.

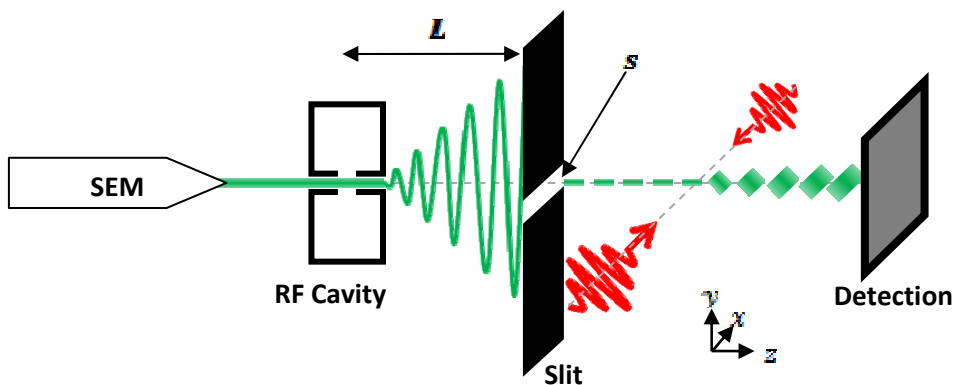


Figure 7.4: Bunch length measurement as would be implemented in the lab.

Figure 7.4 is a schematic representation of how a ponderomotive bunch length measurement would be carried out in this particular project. The SEM provides a DC current of electrons, which is streaked by the TM_{110} cavity, and ultrashort bunches are then chopped out by the slit, exactly as described in Sec. 2.5. After the ultrashort pulses have been created, the bunch length measurement should be carried out.

The first issue to tackle would be alignment. One way to do this is to use a tiny pinhole angled such that all three beams can be aligned through it. This will give spatial alignment, but not temporal alignment. Temporal alignment is a bit trickier. One way that has been suggested is to use a TEM grid rather than a pinhole, placed at an angle for all three beams to go through [14].

The high intensity of the laser at the focus in the TEM grid will create a small plasma that lasts longer than the duration of the laser or electron pulses. This plasma will create a difference in electron density on the detector if it is present at the same time as the electrons. In this way, the laser pulses can be roughly temporally overlapped with the electrons. To gain temporal overlap between the lasers, the same can be done as with one pulse, trying to maximize the shadow, but will require scanning a delay line with reference to

the two laser pulses. From this, it is clear that to gain the temporal overlap and precision needed, a minimum of two delay lines must be employed; one to temporally overlap the two laser pulses, and another to delay the laser pulses with respect to the electron beam.

Assuming temporal and spatial overlap has been achieved, the next issue to tackle is detection. To understand the true difficulty inherent in this configuration, we first consider the electrons. The cavity runs at 3 GHz, giving electron bunches once every half period, yielding a repetition rate of 6 GHz, with an average of ≤ 1 electron per pulse depending on input current. One can make use of the opposite transverse momenta of consecutive electron bunches, mentioned in Sec. 5.1.1, to reduce the repetition rate to 3 GHz.

At this point, it would be helpful to point out that Ti:Sapph lasers have been made with repetition rates up to 10 GHz [17], which would solve all problems of synchronization. However, it would probably not solve the signal to noise ratio, as the intensity is insufficient to scatter the electrons outside of the spread caused by the emittance.

This is not the case for the fs Ti:Sapph laser used in this group. The laser at the disposal of this project delivers 40 fs pulses with an average power of 2.7 W at a repetition rate of 1 kHz, yielding an energy per pulse of 2.7 mJ, well over the 56 μ J used in simulations. In more general terms, the problem is how to detect 1000 scattered electrons and block out or dump away 2,998,499,000 every second, giving a signal to noise ratio of 3×10^{-7} . There are three main solutions to this problem that are suggested, and should probably be used in combination with each other.

The first, and most obvious, is a zero order beam stop. This is simply a grounded piece of metal that can be moved in and out of the beam line to stop the electrons that are not scattered. The dimensions of the beam block should be limited by the spread expected from the scattering, so as not to inadvertently block scattered electrons as well as the unscattered. It is recommended that this solution be used in combination with one of the next two suggestions.

The next solution is to present some form of fast blanker, synchronized to the 1 kHz signal from the laser. This can be achieved with two parallel capacitor plates. A constant voltage is kept on one plate, essentially keeping the electrons deflected away from the original beam line. The other plate is synchronized with the 1 kHz signal, sending a short pulse of a few ns to the opposite plate, essentially turning off the deflector for a short moment. Assuming a window of two ns, only six electron bunches will be created, reducing the signal to noise ratio to ~ 0.17 . The difficult part of this solution is designing the electronics to send a short (\sim few ns) pulse at a repetition rate of 1 kHz; it can be accomplished, but requires a talented electrical engineer to design and build the components. Currently, in our

lab, such a blander was designed and commissioned, which delivers a high voltage pulse of ~5 ns at a repetition rate of 1 kHz. However, changes to the design of the device are still underway, with tests being carried out in the lab.

The last solution was presented in Sec. 6.2. By redesigning the cavity to operate in two modes separated by 1 kHz, the streak will only pass over the slit at a rate of 1 kHz, creating the fs pulses at a repetition rate synchronizable with the 1 kHz laser, giving a 1:1 signal to noise ratio. The difficulty in this solution is that an entire new cavity would need to be designed, with two antennas and two tuning stubs for the two competing modes. On top of that, two signals would have to be generated and amplified, requiring twice the amount of electronics. Also, 1 kHz may not be sufficient separation for the two modes to operate independently. To have full separation of the modes would require a Q factor of about 6 million, far too high to realistically achieve, as the best Q seen in our lab has only been around 10,000. Perhaps with careful designing of the antennas, one mode can be fully coupled into while the other is isolated from that particular antenna, and similar with the second antenna. Further investigation into this solution must be taken before going ahead with the option.

Finally, assuming that at least one of the aforementioned solutions is implemented and working as intended, detection of the electrons themselves must be undertaken. The project uses a single multi-channel plate (MCP) for detection. The expected signal, at best, is only about 2×10^{-16} amps. A single MCP typically does not have enough gain to detect this low signal, so a double or possibly even triple MCP to detect the signal is recommended. Other options have been suggested, as well; one such suggestion is a scan-able charge multiplier (a channeltron for example) with a slit or pinhole, so that a single electron at a particular x -position can be detected. All of the challenges to achieve success in the current beam line are summarized in Table 7.1.

Needed for Success In 30 keV beam line	Kapitza-Dirac Effect	Ponderomotive Bunch Length Measurement
<i>Spatial Alignment for electrons and 2 lasers beams</i>	✓	✓
<i>0th order beam block</i>	✓	✓
<i>Single electron detection</i>	✓	✓
<i>Laser-RF synchronization</i>	✓	✓
<i>fs Laser Pulses</i>	X	✓
<i>ns Laser Pulses</i>	✓	X
<i>Fast Blanker</i>	✓	✓
<i>Higher Brightness Beam</i>	✓	X

Table 7.1: Table listing the challenges to success in the current 30 keV SEM beam line described in Ch. 4. The Kapitza-Dirac effect does not require fs laser pulses, but could be accomplished with longer pulses; it would require a higher brightness source than the SEM currently provides. To accomplish a bunch length measurement, the current beam is sufficiently bright.

7.5 Conclusion

The interesting phenomenon of ponderomotive scattering of electrons was described classically and quantum mechanically. In the classical description and regime, a laser polarization dependence was observed in simulations and later described mathematically in Eq. (7.7). In the quantum mechanical regime and picture, the Kapitza-Dirac effect, i.e. the diffraction of free electrons from a standing light wave grating, can occur. Both of these regimes leave an open door for both theoretical descriptions as well as experimental verification.

Two main applications utilizing this light-electron interaction were presented and discussed: a coherent beam splitter and bunch length measurements. The first requires the diffraction of electrons, which while experimentally challenging having only been accomplished once, could yield fruitful results. It opens up the pathway for possible electron interferometry measurements at low energies. The second, bunch length measurements, requires less precision with respect to electron beam quality and intensity of the laser. With the bunch length measurement, the electron bunches must be accurately synchronized to the laser. By delaying the laser arrival time, with respect to an electron bunch, the amount of

electrons scattered is dependent upon which longitudinal section of the electron bunch overlapped with the lasers. From this, it can be deduced what the longitudinal length of the electron bunch is.

The feasibility of the last application, bunch length measurements, was discussed at length for implementation in our beam line, and is summarized in Table 7.1. It was concluded that in order to achieve success in measuring the bunch lengths, one must overcome a number of hurdles. The first is to reduce the repetition rate of the electron bunches to coincide with the repetition rate of the laser. A second is to block out the unscattered electrons. The final problem to overcome is detection. All three of these problems render detection in our beam line as nearly impossible as it currently is. However, due to the high quality of the beam, it does leave the system as a possible candidate to observe the KD effect with minimal changes to the beam line.

References

- [1] Batelaan, H. "Colloquium: Illuminating the Kapitza-Dirac effect with electron matter optics." *Reviews of Modern Physics* 79 (2007): 929-941.
- [2] P.L. Kapitza, and P.A.M. Dirac. "The reflection of electrons from standing light waves." *Proc. Camb. Phil. Soc.* 29 (1933): 297-300.
- [3] C. Davisson, and L.H. Germer. "The scattering of electrons by a single crystal of nickel." *Nature* 119 (1927): 558-560.
- [4] A.E. Kaplan, and A.L. Pokrovsky. "Fully relativistic theory of the ponderomotive force in an ultraintense standing wave." *Phys. Rev. Lett.* 95 (2005): 053601.
- [5] P.W. Smorenburg, J.H.M. Kanter, A. Lassise, G.J.H. Brussard, L.P.J. Kamp, and O.J. Luiten. "Polarization-dependent ponderomotive gradient force in a standing wave." *Physical Review A* 83 (2011): 63810.
- [6] D.L. Freimund, K. Aflatooni, H. Batelaan. "Observation of the Kapitza-Dirac effect." *Nature* 413 (2001): 142-143.
- [7] Balcou, Ph. "Proposal for a Raman X-ray free electron laser." *Eur. Phys. J. D* 59 (2010): 525-537.
- [8] P. Baum, and A.H. Zewail. "Attosecond electron pulses for 4D diffraction and microscopy." *PNAS* 104 (2007): 18409-18414.
- [9] J. Faure, C. Rechatin, A. Norlin, A. Lifschitz, Y. Glinec, and V. Malka. "Controlled injection and acceleration of electrons in plasma wakefields by colliding laser pulses." *Nature* 444 (2006): 737-739.
- [10] D.M. Giltner, R.W. McGowan, and S.A. Lee. "Atom interferometer based on Bragg scattering from standing light waves." *Phys. Rev. Lett.* 75 (1995): 827-830.
- [11] E. Rasel, M.K. Oberthaler, H. Batelaan, J. Schmeidmayer, and A. Zeilinger. "Atom wave interferometry with diffraction gratings of light." *Phys. Rev. Lett.* 75 (1995): 2633-2637.

- [12] R.C. Forrey, A. Dalgarno, and J. Schmiedmayer. "Determining the electron forward-scattering amplitude using electron interferometry." *Phys. Rev. A* 59 (1999): R942-R945.
- [13] B.J. Siwick, A.A. Green, C.T. Hebeisen, and R.J.D. Miller. "Characterization of ultrashort electron pulses by electron-laser pulse cross correlation." *Opt. Lett.* 30 (2005): 1057-1059.
- [14] Hebeisen, Christoph T. *Generation, Characterization and Applications of Femtosecond Electron Pulses*. Toronto: University of Toronto, 2009. Thesis.
- [15] Pulsar Physics. "General Particle Tracer (GPT) User Manual." n.d. *General Particle Tracer (GPT)*. www.pulsar.nl.
- [16] Kanters, J.H.M. *Electron Bunch Length Measurement using the Ponderomotive Force of a Laser Standing Wave*. Eindhoven: Technische Universiteit Eindhoven, 2011. Master's Thesis.
- [17] A. Bartels, D. Heinecke, and S.A. Diddams. "Passively mode-locked 10 GHz femtosecond Ti:sapphire laser." *Optics Letters* 33 (2008): 1905-1907.

Summary

In this thesis we have taken many of the RF ideas of Ura, Oldfield, and Hawkes from the 1960's, coupled with modern technology and simulating power to investigate the usage of miniaturized RF technology for femtosecond electron microscopy without the mandatory use of femtosecond lasers.

To achieve femtosecond time resolution, a TM_{110} cavity is used to streak a DC electron beam across a slit, creating ultrashort electron bunches at a regular repetition rate. To create a miniaturized cavity, the TM_{110} cavity was loaded with $ZrTiO_4$. This reduced the size of the cavity by nearly a factor of 6, and the power was reduced by nearly a full order of magnitude. Characterization of the cavity found that the dielectric loaded cavity operated as it was designed to do, matching both simulations and theory.

To test the RF technology developed in our group, a 30 keV SEM beam line was built on top of an optical table. This allows for the beam line to be extended ~ 2.5 meters beyond the end of the SEM, giving space and room for experiments that would not otherwise be available in a standard electron microscope. This allows for multiple cavity systems to be tested, as well as emittance measurements of a high quality beam, requiring long distances to resolve the small angles.

Implementation of the TM_{110} cavity into the beam line proved quite successful, with the beam behaving as expected. Chapter 5 builds an analytical model which predicts the beam's behavior through the cavity, and goes a step further to predict the growth in transverse normalized emittance and the energy spread of a beam as it traverses the cavity. The analytical model is then compared to particle tracking simulations, proving to be accurate for high quality beams. The measurements of the emittance demonstrate the behavior predicted by the analytical model, and match with the numerical simulations. An important point realized from the model is that focusing in the cavity makes all the difference, minimizing the emittance and energy spread growth. This is an important detail for using the TM_{110} cavity, since a high beam quality is always desired to obtain spatial resolution.

Chapter 6 detailed a few of the myriad of ideas of which can be done with the RF technology studied within the scope of this project. First, as the project is part of a larger industrial partnership program with the private company FEI, a full simulated study of implementing the TM_{110} cavity into an existing FEI electron microscope was carried out in cooperation with the company. In the parameter space presented by FEI, the energy spread growth from the cavity in generating 100 fs bunches appears too high, reaching ~ 10.5 eV FWHM. However, by relaxing a few of the constraints, and changing the parameters of the

setup, it was shown that the energy spread growth can be compensated for. Because of the compact size and low power consumption of the dielectric cavity, this makes the cavity an ideal candidate for femtosecond electron bunch generation in a microscope.

Following the implementation study, the idea of reducing the repetition rate of the bunches by using a dual mode cavity was presented. This was an idea that stemmed from a “Huh, that is strange...” moment in lab. The moment is seen in Fig. 6.5; it is when the two formerly degenerate modes were being operated simultaneously in one cavity. If the cavity was re-designed to use the two modes, running with two different frequencies, the repetition rate of the electron bunches could then be tailored to match repetition rates in the MHz range, rather than GHz.

The original designs of Ura and Oldfield included multiple cavities synchronized to manipulate the beam. However, Oldfield commented in his Ph.D. thesis that the phase control was of the utmost importance. In Sec. 6.3, we demonstrated a high precision of phase control between two cavities, a TM_{110} streak cavity and a TM_{010} compression cavity, and supported the results with numerical simulations. With phase control between multiple cavities demonstrated, both synchronized to the same RF signal, the door to time-dependent beam manipulation has flown wide open.

Section 6.4 walks right through the multiple cavity door, and presents a two cavity setup to compete with Zewail’s photocathode driven ultrafast electron microscope (UEM). Using two TM_{110} cavities, femtosecond electron energy loss spectroscopy (FEELS) was simulated using particle tracking software. It was shown that with the two cavities, appropriately phased, an energy resolution of <1 eV can be achieved. To take it a step further, the FEELS scheme was tested with the measured beam quality of the 30 keV beam line. It was found that when a third cavity was added, a TM_{010} cavity, a resolution of <1 eV could again be achieved. In theory, an old donated W-hairpin 30 keV SEM coupled with three RF cavities could perform the same experiments as Carbone or Yurtsever, in which FEELS studies were carried out with sub-eV resolution with Zewail’s specially designed UEM at Caltech. For this reason, it has been dubbed the “Poor man’s FEELS.”

Finally, to bring Ch. 6 to a close and full circle back to the early work of Ura, Oldfield, and Hawkes; the use of the TM_{010} cavity as a spherical aberration corrector was simulated. Using a solenoid and a highly divergent beam, the spherical aberration caused by the solenoid is very easily seen in Fig. 6.12. By increasing the field amplitude in the TM_{010} cavity, it is found that the spherical aberration is corrected for, and eventually over-corrected. This demonstrates that pulsed beams in combination with time-dependent lenses (RF cavities in this case) can correct for spherical aberration. However, this correction comes at the cost of

energy spread/chromatic aberration; the beam is stretched longitudinally when it is at the appropriate spherical aberration correction phase of the cavity.

The thesis concludes with remarks on the ponderomotive light-electron interaction. A classical description as well as a quantum mechanical hand waving argument is given for the effect. Within the classical framework, a polarization dependent equation for the ponderomotive potential was developed and presented. Within the quantum picture, the Kapitza-Dirac effect is discussed, being the diffraction of electrons from a standing light-wave grating. The applications of the two pictures are discussed, focusing on a bunch length measurement scheme and using the KD effect as a coherent beam splitter. Finally, the feasibility of the bunch length measurement in the 30 keV beam line with the TM_{110} streak cavity is discussed. It is found that to achieve success, a number of obstacles must be overcome.

This thesis covers the work of investigating the use of RF technology for femtosecond electron microscopy. It has been shown that with a TM_{110} cavity, ultrashort bunches can be created at a regular repetition rate. It was then demonstrated that with ultrashort bunches at a regular interval, more TM_{110} cavities can be used to create a Poor man's FEELS, or utilize a TM_{010} cavity to enhance the FEELS experiment or for spherical aberration correction. With the use of this developed RF technology, it has been shown that improvements to time resolution while maintaining the transverse properties of an electron beam can be achieved by means of RF cavities. In this way, we have concluded that RF technology can be utilized as tools for the advancement of the electron microscopy community.

Outlook

Like most scientific endeavors, this project has left many ideas open and ready to be tested, applicable to both industry and academia. Chapters 6 and 7 outlined many of them: implementation into an existing microscope column, dual mode cavity, poor man's FEELS, spherical aberration correction, and the Kapitza-Dirac effect.

Implementation into an existing microscope is the next logical step for future projects. It would consist of building a miniature TM_{110} cavity into the beam line of an existing microscope. Because of the complexity of most electron microscope columns and the potential marketing value of a time resolved EM, the project would most likely have to be carried out either in full by FEI or at the very least by a Ph.D. student at FEI's lab. From there, it would be interesting to accurately measure the peak brightness of the beam, and compare the measurements to the analytical model described in Ch. 5.

Because an EM with time resolution would, in most cases, have to be synchronized with a laser to perform pump-probe experiments, it would be useful to perhaps develop a dual mode cavity in tandem with the implementation into an existing column. This would be an ideal master student project, or a first task for a Ph.D. to become comfortable with RF technology and designing. Again, due to marketability of such a product, the project would be ideal for FEI to be a part of.

In the existing 30 keV beam line, described in Ch. 4, the rigorous testing of the spherical aberration correction can be carried out. This requires two cavities, one TM_{110} and one TM_{010} , synchronized to each other, as was demonstrated in Sec. 6.3. By using a mono-crystalline sample with known diffraction angles, the spherical aberration could be measured and corrected for, just as was done in Sec. 6.5.

Once multiple cavities have been synchronized to each other, the beam line could be used to perform the Poor Man's FEELS experiments. In particular, the three cavity system, described in Sec. 6.4.1, could be carried out. In theory, all the tools to achieve it are there. It just needs to be done. However, in order to achieve a successful FEELS measurement, a pump-probe setup would have to be designed, which means the struggles of implementing and synchronizing a laser to the electron pulses at the sample. Many of these difficulties are outlined in Table 7.1.

Chapter 7 discussed the interaction between electrons and a standing light wave. To achieve either the Kapitza-Dirac effect or ponderomotive bunch length measurements would require a herculean effort by a single Ph.D. The fruits of their labor would be well worth it if the challenges summarized in Table 7.1 could be overcome. Both the KD effect and bunch

length measurements can, in theory, be achieved with the beam line built. To whoever takes on the project of investigating electrons in a standing light wave, to you I say good luck.

From this, it is obvious that there are multiple paths for future work that have been opened by this research, both in industry and in academia. The use of cavities in a microscope could be highly interesting and profitable for industry; further development and building of multiple cavity arrangements can prove to be highly useful for a low cost for research institutions; free electrons in a standing light wave is highly difficult, but as a result, poorly understood leaving lots of room for research to be carried out.

A Appendices

A.1 Emittance: Collimated Case

Consider an electron traveling with initial velocity v_z entering the cavity with phase φ , defined as the phase when the electron is at the center of the cavity. The cavity has a uniform magnetic field oriented in y oscillating with radial frequency ω and amplitude B_0 when $t_b \leq t \leq t_e$, where t_b and t_e are the beginning and end times of the cavity for a traversing electron located at the center of a bunch of temporal length τ . From this, the force, momentum, and position can be tracked through the cavity. For simplicity, the cavity will be centered around $t=0$ so that $t_b = -t_e = -\tau/2$.

$$B_y = B_0 \sin(\varphi + \omega t), \quad \text{A.1}$$

$$F_x = q(v_z \times B_y) = -B_0 q v_z \sin(\varphi + \omega t), \quad \text{A.2}$$

$$p_x = \int_{t_b}^t F_x dt = \frac{B_0 q v_z}{\omega} (\cos(\varphi + \omega t) - \sin \varphi), \quad \text{A.3}$$

$$x_{beam} = r \cos \theta. \quad \text{A.4}$$

The normalized rms transverse emittance is defined as

$$\varepsilon_N = \frac{\sqrt{\langle x^2 \rangle \langle p_x^2 \rangle - \langle x p_x \rangle^2}}{mc}, \quad \text{A.5}$$

where $\langle \text{var} \rangle$ is defined as $\frac{\int_{t-\tau/2}^{t+\tau/2} \int_0^{2\pi R} \int_0^{2\pi R} (\text{var}) r dr d\theta dt}{\int_{t-\tau/2}^{t+\tau/2} \int_0^{2\pi R} \int_0^{2\pi R} r dr d\theta dt}$ and $\langle \text{var}^2 \rangle$ as $\langle (\text{var} - \langle \text{var} \rangle)^2 \rangle$. Knowing

that $\langle x p_x \rangle = 0$ for the collimated case, we find for the emittance growth at the entrance ($t = t_b$) of the cavity to be

$$\varepsilon_{N,b} = \frac{B_0 q R v_z}{2\sqrt{2}mc \tau \omega^2} \times \sqrt{-2 + \tau^2 \omega^2 + 2 \cos[2\varphi] + 4 \cos[\tau\omega] \sin^2 \varphi - \tau\omega \cos^2 \varphi \sin[\tau\omega] + \tau\omega \sin^2 \varphi \sin[\tau\omega]} \quad \text{A.6}$$

Taking the small angle approximation around $\tau=0$ yields (because $\omega\tau \ll \pi$; the bunch length is much smaller than half of a period of the cavity)

$$\varepsilon_{N,b} = \frac{B_0 q R v_z \tau}{4\sqrt{3}mc} \sqrt{\cos^2 \varphi} \quad \text{A.7}$$

Doing the same for $t=t_e$ and summing the emittance growth at the beginning and end of the cavity yields for the collimated case.

$$\varepsilon_{N,col} = \frac{B_0 q R v_z \tau}{2\sqrt{3}mc} |\cos \varphi| \quad \text{A.8}$$

A.2 Emittance: Focused Case

Consider the same situation as in appendix A, with the exception that the bunch is now focused to point t_x . As a result, x and p_x are now comprised of multiple terms summed together, and $\langle xp_x \rangle$ is no longer zero.

$$p_{x,cav} = \int_{t_b}^t F_x dt = \frac{B_0 q v_z}{\omega} (\cos[\varphi + \omega t] - \sin[\varphi]), \quad \text{A.9}$$

$$x_{cav} = \int_{t_b}^t \frac{p_{x,cav}}{m} dt = \frac{B_0 q v_z}{m \omega^2} \left(\cos[\varphi] - \left(\frac{\pi}{2} + \omega t\right) \sin[\varphi] + \sin[\varphi + \omega t] \right), \quad \text{A.10}$$

$$x_{beam} = r \cos[\theta] \left(\frac{t_x - t}{t_x - t_0} \right), \quad \text{A.11}$$

$$p_{x,beam} = m \frac{\partial x_{beam}}{\partial t}. \quad \text{A.12}$$

In Eq. (A.11) and (A.12), t_x is the focal point of the beam, and t_0 is the point before the cavity where the radius R is measured. The emittance shall, same as appendix A.1, be defined as

$$\mathcal{E}_N = \frac{\sqrt{\langle x^2 \rangle \langle p_x^2 \rangle - \langle xp_x \rangle^2}}{mc}, \quad \text{A.13}$$

where x and p_x are now the summations of Eq. (A.10) and (A.11), (A.9) and (A.12), respectively.

Similar to the collimated case, the limits of integration are still the same; and same as the collimated case, the emittance growth must be calculated at the beginning and end of the cavity (t_b and t_e , respectively), and summed together. Still analogous to the collimated case, a series expansion around $\tau=0$ (small angle approximation) must be taken, but then followed with an expansion around $R=0$ (again, small angle, assuming $R \ll |v_z t_0|$; i.e. small half angle of the incoming beam). This yields for the emittance in the focused case

$$\mathcal{E}_{N,b} = \frac{B_0 q R v_z \tau}{8\sqrt{3}mc\omega} \sqrt{\frac{(\pi + 2t_x \omega)^2 \cos^2 \varphi}{(t_x - t_0)^2}}, \quad \text{A.14}$$

$$\mathcal{E}_{N,e} = \frac{B_0 q R v_z \tau}{8\sqrt{3}mc\omega} \sqrt{\frac{((\pi - 2t_x \omega) \cos \varphi - 4 \sin \varphi)^2}{(t_x - t_0)^2}}, \quad \text{A.15}$$

$$\mathcal{E}_{N,foc} = \frac{B_0 q R v_z \tau}{8\sqrt{3}mc\omega} \sqrt{\frac{(\pi + 2t_x \omega)^2 \cos^2 \varphi}{(t_x - t_0)^2}} + \sqrt{\frac{((\pi - 2t_x \omega) \cos \varphi - 4 \sin \varphi)^2}{(t_x - t_0)^2}}. \quad \text{A.16}$$

The equation for the focused case emittance can be re-arranged to equal the collimated case (A.8) times a factor that is dependent upon the focal point.

$$\mathcal{E}_{N,foc} = \frac{B_0 q R v_z \tau}{2\sqrt{3}mc} |\cos \varphi| \left(\sqrt{\frac{(\pi + 2t_x \omega)^2}{(t_x - t_0)^2 16\omega^2}} + \sqrt{\frac{((\pi - 2t_x \omega) - 4 \tan \varphi)^2}{(t_x - t_0)^2 16\omega^2}} \right). \quad \text{A.17}$$

As a quick check, taking the limit as t_x goes to infinity should yield the collimated case. QED.

A.3 Energy Spread

The energy spread arises from the z-component of the Electric field. An approximation for the E_z component is found from the Maxwell-Faraday equation, $\nabla \times E = -\frac{\partial B}{\partial t}$, using Eq. (A.1) for the magnetic field.

$$E_z = B_0 \omega X \cos[\omega t + \varphi] \quad \text{A.18}$$

In Eq. (A.18), $X = x_{cav} + x_{beam}$ is the summation of the two x-components (A.10 and A.11). The energy spread is directly proportional to the momentum in the z-direction gained from the cavity taken along the path of x_{cav} .

$$p_z = p_{z0} + q \int_{t_b}^t E_z dt \quad \text{A.19}$$

$$\sigma_{pz} = \sqrt{\langle p_z^2 \rangle} \quad \text{A.20}$$

The spread in z-momentum is calculated with nearly the same limits of integration as Appendices A and B. Unlike the emittance, an integration along the time dimension is not necessary, instead only requiring that everything be evaluated at $t=t_e$ because unlike the emittance, the energy spread grows during the transit across the cavity, not at the entrance and exit. The integration of r and θ are still kept the same as the emittance. By multiplying the z-momentum spread by v_z yields for the rms energy spread for the collimated and focused case

$$\sigma_{U,col} = B_0 R v_z |\cos \varphi| \quad \text{A.21}$$

$$\sigma_{U,foc} = B_0 R v_z |\cos \varphi| \sqrt{\left(\frac{t_x}{t_x - t_0} + \frac{\tan \varphi}{\omega(t_x - t_0)} \right)^2} \quad \text{A.22}$$

A.4 Electromagnetic Fields of a fs Laser Pulse

Simulations in Ch. 7 used the electromagnetic fields of a fs laser pulse to numerically simulate the ponderomotive force. Below are the fields used, following paraxial Gaussian beam fields approximation polarized in the z-direction, traveling in the $\pm x$ -direction.

$$\vec{E} = E_+ \exp\left[-\frac{(x+ct)^2}{4(c\sigma)^2}\right] + E_- \exp\left[-\frac{(x-ct)^2}{4(c\sigma)^2}\right] \quad \text{A.23}$$

$$E_{\pm} = E_0 \frac{w_0}{w} \left(\vec{e}_z \cos\psi_{\pm} \pm \frac{zw_0}{x_R w} \vec{e}_x \sin\chi_{\pm} \right) \quad \text{A.24}$$

$$\vec{B} = B_+ \exp\left[-\frac{(x+ct)^2}{4(c\sigma)^2}\right] + B_- \exp\left[-\frac{(x-ct)^2}{4(c\sigma)^2}\right] \quad \text{A.25}$$

$$B_{\pm} = \frac{E_0}{c} \frac{w_0}{w} \left(\pm \vec{e}_y \cos\psi_{\pm} - \frac{yw_0}{x_R w} \vec{e}_x \sin\chi_{\pm} \right) \quad \text{A.26}$$

where $E_0 = \sqrt{2I_0 / (\epsilon_0 c)}$ is the peak electric field amplitude, $w = w_0 \sqrt{1 + x^2 / x_R^2}$ is the beam waist, $x_R = kw_0^2 / 2$ is the Rayleigh length, σ is the temporal standard deviation of the pulse, and the Gouy phases are given as

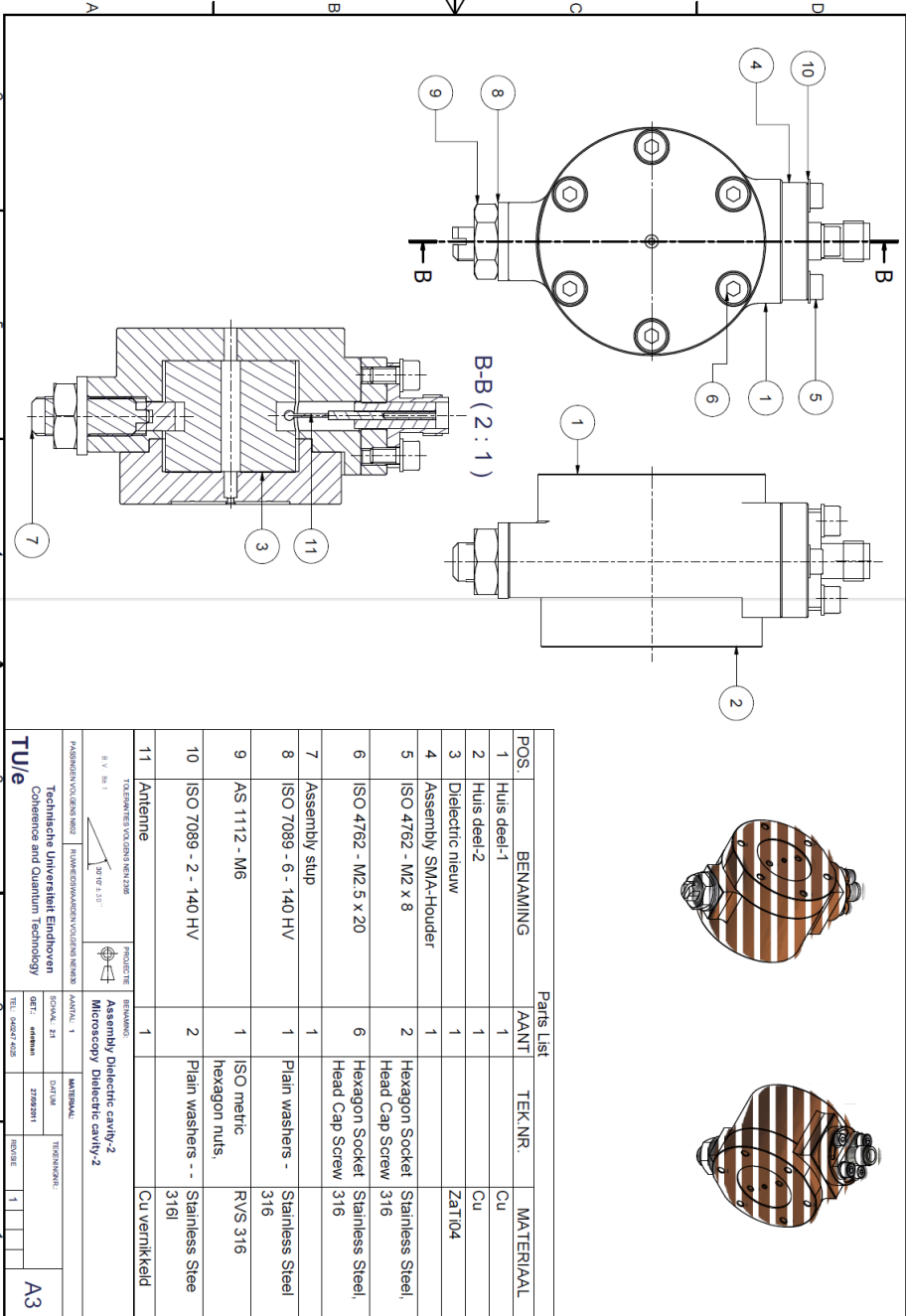
$$\psi_{\pm} = \omega t \pm \left(kx - \arctan \frac{x}{x_R} + \frac{x}{x_R} \frac{y^2 + z^2}{w^2} \right) \quad \text{A.27}$$

$$\chi_{\pm} = \omega t \pm \left(kx - 2 \arctan \frac{x}{x_R} + \frac{x}{x_R} \frac{y^2 + z^2}{w^2} \right) \quad \text{A.28}$$

To change the polarization from z to y, one should replace $z \rightarrow y$ and $y \rightarrow -z$ in the above expressions.

A.5 Technical Drawings for the TM₁₁₀ Dielectric Cavity

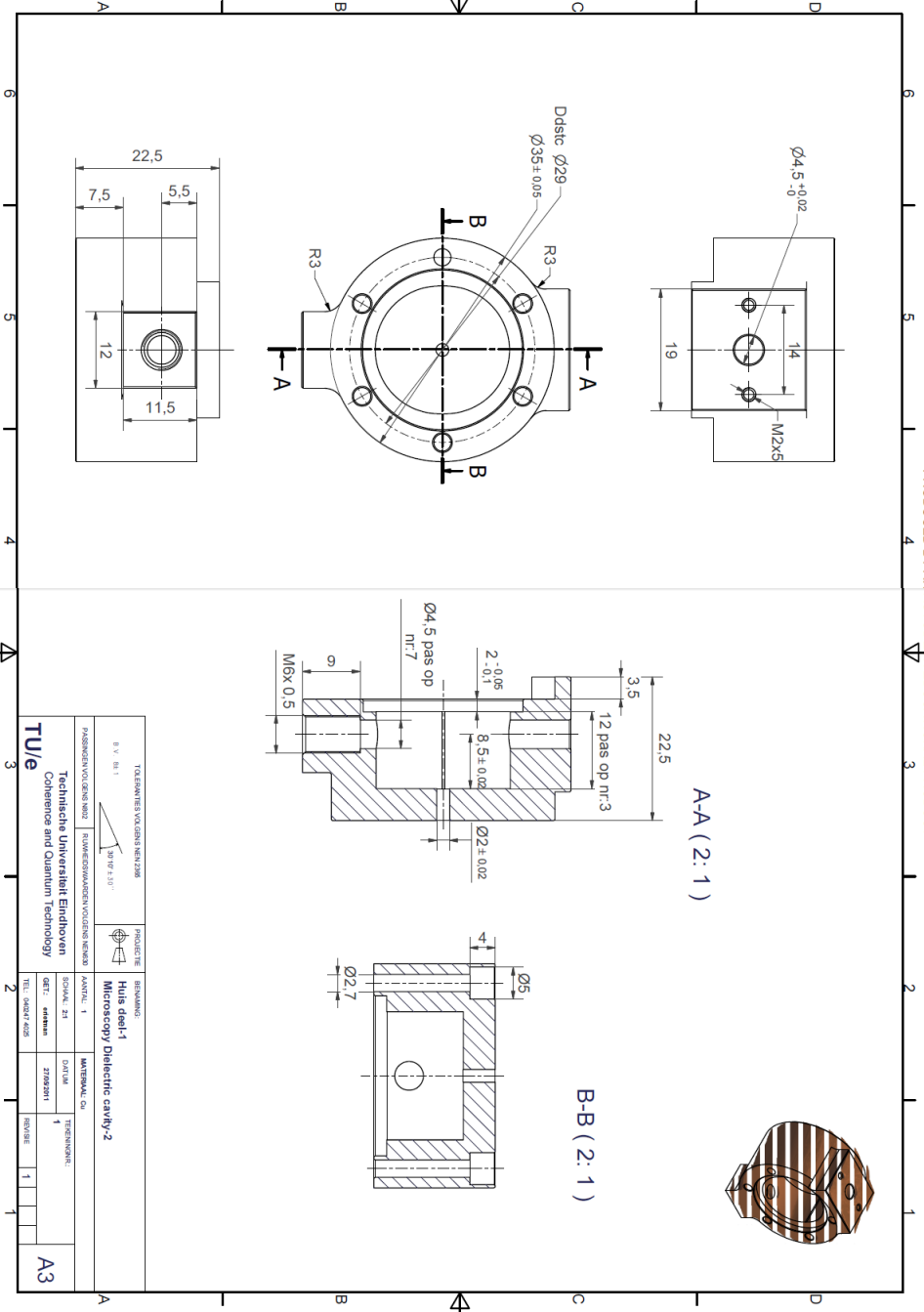
PRODUCED BY AN AUTODESK EDUCATIONAL PRODUCT



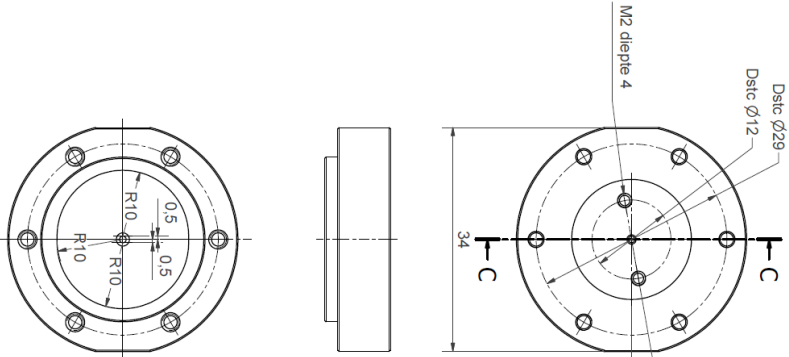
PASSEEREN VOOR DE NIEUW Technische Universiteit Eindhoven Coherence and Quantum Technology		PRODUCTIE Microscopy Dielectric cavity-2	
AANTAL: 1 SCALF: ZH OAFW: ZH00001	AANTAL: 1 SCALF: ZH OAFW: ZH00001	AANTAL: 1 SCALF: ZH OAFW: ZH00001	AANTAL: 1 SCALF: ZH OAFW: ZH00001

PRODUCED BY AN AUTODESK EDUCATIONAL PRODUCT

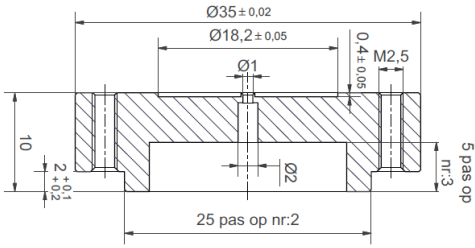
PRODUCED BY AN AUTODESK EDUCATIONAL PRODUCT



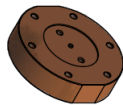
TU/e		Technische Universiteit Eindhoven Coherence and Quantum Technology	
PROJECTIE	REVISIONS	DATE	BY
Microscopy Dielectric cavity-2	Huis die1-1	2017-1-10	1
PROJECT LEADER	DESIGNER	CHECKER	APPROVER
1	1	1	1
A3		A3	



Opm:
R10 +0.02 +0.02 pas op nr:3



C-C (3:1)



TOEGEWIJZDE VOLGENDE NUMMER B.V. 44.1 30° OF 15°		PROJECTIE 		BEGRIPPEL Huls deel:2 Microscopy Dielectric cavity: 2	
PASSEREN VOLGENDE NUMMER Technische Universiteit Eindhoven Coherence and Quantum Technology	TOEGEWIJZDE VOLGENDE NUMMER TECHNISCHE UNIVERSITEIT EINDHOVEN COHERENCE AND QUANTUM TECHNOLOGY	JAARNAAL: 1 SCHAKEL: 3A DEEL: 444444 TITEL: MICRO: 4444	MATERIEEL: CU DATUM: 2 ZAKENNUMMER: 1 VERSIE: 1	A3	

Acknowledgements

Good lord it's been a long path to get here. And I would be painfully conceited and arrogant to not thank everyone who has helped me get to this point. And if anything, this PhD has been a humbling experience... So, let's begin.

Jom, you decided to hire some American kid living in Germany after only a phone call and a day with me for reasons that are still beyond me (I'm leaning towards "nobody else wanted the project"; that and I took my lip ring out). But for that opportunity, I'm forever grateful. On top of the opportunity, you always seemed to be able to point me in a direction when I'd run into the "Well... what do we do now...?" moment. Your guidance and help as my promotor and advisor was an essential key to success for the project. Dank je wel.

Peter M., Edgar, and Seth: you all three have, at some time or another, given input, advice, and criticism that was crucial to this project. It's been a pleasure bouncing ideas off of you gentlemen, and to your credit, you always had good comments in return.

To our technicians whom, without, I would not have had much of a setup to do experimental work with: Eddie, Jolanda, Iman, Harry, Ad, Wim, and Louis. (Louis, I'm still slightly upset with you for retiring midway through my project but I suppose I can find it in me to forgive you... After all, you did build most of my setup, and first cavity). All of you were the support crew that made experimental work possible. You're able to take my bad pencil drawings, and turn them into working setups. I'm constantly amazed with how helpful you all are and the work all of you accomplish for us. Thank you all again and again. Also, Iman, thanks for letting me come in and bother you in those late afternoon times when motivation to continue working was dwindling; always a pleasure sir.

To the GPT'ers- Bas and Marieke: I still don't care much for programming, I'm afraid you didn't convert me. But I do have to say thank you for always being able to help me in explaining and diagnosing my GPT problems. And doing so without making me feel too stupid. This thesis absolutely would not have been possible without GPT and your support. Thank you for all your help.

Betty. You're just awesome. You are always friendly, helpful, and able to guide me through the bureaucracy of the university. It made everything a thousand times easier for this buitenlander to navigate the corridors. Bedankt.

To the "old" promovendi, (not to imply you're old, just were finishing much earlier than me): Gabriel, Willem, Merijn, Thijs v. O.; you guys set the cornerstone on how to survive and

thrive in the group. You led by example, and I soaked it all in as much as I could. I am thankful for all of you helping me get started, and for making me feel welcome in the group.

To those promovendi I spent the most time with: Xavier, thank you for relinquishing the title “hardest working phd in the bunker” to me after you left. It’s an honor. Stefan, you’re like the energizer bunny except powered by a nuclear reactor; you never tire on energy or excitement or cheer, quite the dichotomy to me. I don’t know how you do it, but it made the last four years better. At the very least coffee breaks were entertaining... Nicola, mi favorito italiano. You’re the most relaxed, easy going, friendly person I have ever known, and I am happy to call a friend. Thijs Meijer, you’re still my favorite Dutchman under 6 foot (1.83 meters). Rick and Wouter, I hope that I haven’t bothered you too much in our office with my loud music or nervous tapping of feet/hands/pens/etc; it’s been a pleasure sharing the office with you guys, and being able to spin around in my chair and be able to chat about nearly anything. It made those late afternoon slumps manageable. Peter P., I’ve traveled to two different countries with you (USA and Canada) and both times I enjoyed being at those places with you. Despite quite different (polar opposite) work styles, it’s been enjoyable working on similar projects with you. Peter S. and Maikel, I still have to admit I don’t understand all that you theoreticians do, but I always appreciated you taking the time to try to explain it to me when I would ask. I realize it was probably like trying to explain wave-particle duality to a 10 year old, so thank you. Steiner, Servaas, Jaap, Ton, Marnix, Corine, Stefano, Joris, Erik, and all the rest of my colleagues, current and former, thank you for making this job worth coming to in the morning.

Bas, our once a week beer summits was very much a necessity for my survival in Eindhoven. I’m sure we solved most of the world’s problems, all for the price of a few crates worth of beer. And we still need to do a trip through the US together. Next time...

Michael Berger, sir! You’ve been the most amazing friend I could’ve asked for, even if you are German... Our evening video chats kept me going through the best times and worst. Danke schön.

Vera. Arawr! I know you feel that since this PhD has been such a huge part of my life as long as you’ve known me, you feel that you’ve earned part of a degree as well... Or at the very least, get your name on the cover here... Honestly though, you made the last two years worth while. You’ve made me comfortable and relaxed again, and have given me unwavering love and support in pursuing this degree. I’ll avoid the cliché, “I couldn’t have done it without you,” but I’ll gladly tell you that I’m forever thankful and happy to be able to share this with you. You’re my girl, and I wouldn’t change it for the world. I love you. GRAWR!

Now for the family. Mom-Dad (I've combined you both into a single entity now), thank you for all the love and support through all of this. You gave me the determination and work ethic as well as the courage to step out into the world on my own that has gotten me here today. Turning around and looking back, I'm a long ways away from my home in Tucson and doing just fine, and it's all thanks to you. So I hope now that you've read this far (I know you read the entire thing already...), that I've made you proud. Thanks Mom-Dad.

Grandma, I'm proud to send you a copy of this for the official Monowi Library. I know that you're just as proud of me as Mom and Dad, and I have to thank you for being the awesome grandmother that you are... Who else can brag that their grandmother is both a Mayor and she owns a bar? Thank you for all the wonderful support.

To all the rest of my friends and family whom I didn't mention, thank you for the love and support. This has been one hell of a rollercoaster ride, and I know I've shared both the ups and downs with all of you... Hopefully more ups than downs. But in the end, all of you made it possible for me to survive. For that, I'm forever grateful.

Thank you, all.

Curriculum Vitae

ADAM LASSISE

PERSONAL DETAILS

Name	Adam Christopher Lassise
Email	A.Lassise@gmail.com
Date of Birth	January 5 th , 1984
Nationality	American

EDUCATION

- 2008-2012 **Ph.D. researcher in Applied Physics (Technische Natuurkunde)**
Technische Universiteit Eindhoven (NL)
Topic: Miniaturized RF technology for femtosecond electron microscopy.
- 2006-2008 **MSc in Nanomolecular Science,**
Jacobs University Bremen (DE).
• Emphasis Experimental Physics
- 2002-2006 **BSc in Physics**
University of Redlands (USA).
• Major Physics
• Minor Mathematics
- 1998-2002 **High School Degree**
Mountain View High School (USA)
-

PEER REVIEWED PUBLICATIONS

- A. Lassise**, P.H.A. Mutsaers and O.J. Luiten *Compact, Low Power Radio Frequency Cavity for Femtosecond Electron Microscopy*, in *Review of Scientific Instruments*, 83, 2012.
- P.W. Smorenburg, J.H.M. Kanters, **A. Lassise**, G.J.H. Brussard, L.P.J. Kamp, and O.J. Luiten *Polarization-Dependent Ponderomotive Gradient Force in a Standing Wave*, in *Phys. Rev. A*, 83, 2011.
- R. Temirov, **A. Lassise**, F.B. Anders, and F.S. Tautz *Kondo Effect by Controlled Cleavage of a Single-Molecule Contact*, in *Nanotechnology*, 19, 2008.
- R. Temirov, S. Soubatch, **A. Lassise**, and F.S. Tautz *Bonding and Vibrational Dynamics of a Large π -Conjugated Molecule on a Metal Surface*, in *J. Phys: Condensed Matter*, 20, 2008.
- R. Temirov, S. Soubatch, O. Neucheva, **A. Lassise**, and F.S. Tautz *A Novel Method Achieving Ultra-High Geometrical Resolution in Scanning Tunnelling Microscopy*, in *New Journal of Physics*, 10, 2008.